University of Stavanger

Faculty of Science and Technology

MASTER'S THESIS

Study program/ Specialization: Petroleum Technology/ Reservoir Engineering	Spring semester, 2012 Open
Writer: Leif Inge Ramsdal	…… (Writer's signature)
Faculty supervisor: Svein Skjæveland External supervisor(s): Ingebret Fjelde	
Titel of thesis: Interactions between CO_2 and Cap Rock during CO_2 Storage	
Credits (ECTS): 30	
Key words: CO_2 Storage CO_2 Sequestration Trapping mechanisms Kinetic batch modelling Reactive transport modelling Diffusion	Pages: 85 + enclosure: 8 Stavanger, 14.6/2012 Date/year

Acknowledgement

First of all I want to thank my supervisor Dr. Ingebret Fjelde for providing me with an interesting master thesis, and for holding regular meetings where he has given me excellent follow-up. I would also like to thank him for reading through the thesis and giving his thoughts on it.

I would like to thank PhD. student Alexandre Vilela for his excellent help with the simulations. I would also like to thank him for all the interesting off-topic conversations we had during the semester.

I want to thank my faculty supervisor, Prof. Svein Skjæveland, for the meeting we had in early March where he provided me with ideas and knowledge about what is needed to write a good thesis.

Finally, I wish to thank my family, friends and especially Christin for patience and encouragement during the semester.

Leif Inge Ramsdal

Abstract

Geological sequestration and storage of carbon dioxide is a viable method for mitigating anthropogenic emissions of fossil fuels into the atmosphere. Geochemical reactions play an important role in CO_2 storage environments because they may change the properties of the overlying cap rock, and can either enhance or degrade the storage capacity and feasibility of a CO_2 storage project. Geochemical models can simulate these interactions and provide important knowledge of the feasibility of a CO_2 storage project at different settings.

In this thesis the geochemical simulation tool PHREEQC is used to simulate CO_2-rock-brine interactions at two distinct sites, Nordland Shale and Frio Shale. Both kinetic batch modelling and reactive transport modelling were conducted. Kinetic batch modelling results show that mineral dissolution and precipitation reactions is strongly related to the presence of carbon dioxide in the cap rock. Carbonate minerals precipitate as a consequence of the dissolution of CO_2. When CO_2 dissolves some of it will be permanently trapped in the precipitating carbonates in a process referred to as mineral trapping. Silicate dissolution or precipitation is also seen as a strong function of the behaviour of CO_2. Albite dissolution is the main mechanism for silicate precipitation at both storage sites.

Reactive transport modelling results indicate that the first 5-10 meters are affected by diffusive transport for the Nordland Shale formation, whereas the first 20-25 meters of the cap rock are affected by diffusive transport for the Frio Shale formation. This indicates that porosity and permeability of the lower cap rock are altered. Mineralogical changes within the area affected by diffusive transport are significantly larger for Nordland Shale compared to Frio Shale. Future studies should include advection transport to investigate the effects a flow rate would have on the cap rock mineralogy.

Table of Contents

Nomenclature

A	Temperature dependent constant, A = 0.5085 at 25°C
A_a	Pre-exponential factor
A_m	Reactive surface area for a given mineral
[A]	Concentration of reactant
α	Reaction order with respect to A
β	Reaction order with respect to B
C_A	Concentration of A
C_B	Concentration of B
CCS	Carbon Capture and Storage
CBM	Coal bed methane
CO_2	Carbon dioxide
CO_2-EOR	Carbon dioxide based Enhanced Oil Recovery
CO_2-EGR	Carbon dioxide based Enhanced Gas Recovery
D'_d	Effective diffusion coefficient (also referred to as D_d in the text)
E_a	Activation energy
EBCMR	Enhanced Coal Bed Methane Recovery
EOR	Enhanced Oil Recovery
GHG	Greenhouse gas
Gt	Gigaton
I	Ionic strength
[i]	Dimensionless activity
IAP	Ionic activity product (also referred to as Q_m in the text)
IGIP	Initial Gas in Place
J	Diffusional flux
K	Equilibrium constant
k	Rate constant
kg/m^3	Kilogram per cubic meter
γ_i	Dimensionless activity coefficient
m_i	Molality
mol/kgw	Moles per kilogram of water

mmol/kgw	Millimoles per kilogram of water
MPa	Megapascal
Mt	Megaton
$MW_{mineral}$	Molecular weight of a given mineral
n	Reaction order
N/A	Not available
n_{moles}	Number of moles of a given mineral
OS	Organic shale
P_{CO2}	Partial pressure of carbon dioxide
PV	Pressure and volume
R	Universal gas constant
$rate_m$	Rate of a given mineral
SI	Saturation index
T	Absolute temperature (K)
V	System Volume

1. Introduction

Carbon dioxide is a greenhouse gas. The greenhouse effect is well-documented and controversial, but evidently contributes to the increased global average temperature. This affects availability of food, water and natural habitats of both humans and animals. Mitigating these climate changes caused by the greenhouse gases is therefore an important issue, which is of global interest. Anthropogenic carbon dioxide emissions have increased dramatically in the last century. Estimates show that carbon dioxide contributes 64 % of the increased greenhouse effect (Li et al. 2006). This large contribution is due to production of fossil fuelled energy, which today constitutes approximately 75 % of the world's energy supply and are likely to remain a major factor in the next century (Bachu and Adams 2003).

Most research is focused on carbon dioxide due to the large quantity it represent of the total greenhouse gas emissions. A promising method in the work to reduce GHG emissions is to geologically store CO_2 in the subsurface. Geological storage is the process where CO_2 is captured and subsequently injected into a geological formation in a supercritical state where it is trapped by one or more trapping mechanisms. This prevents CO_2 from leaking through geological seals. Project monitoring and simulation studies are conducted before, during and after injection to prove that the carbon dioxide can be trapped within a geological time scale (thousands to millions of years) without leaking into overlying groundwater reserves, oceans or into the atmosphere. During this time frame a fraction of the CO_2 will ultimately dissolve in the formation water and promote geochemical reactions with the surrounding minerals. These geochemical reactions may alter the cap rock properties and may thus affect the cap rock integrity.

The objective of this thesis is to use a simulator programme called PHREEQC Interactive to simulate the geochemical effects occurring in the cap rock when CO_2 interacts with the cap rock minerals. Relevant data is obtained from literature and used as input to the programme code. Batch modelling and reactive transport modelling are conducted on the Nordland Shale

of the Sleipner West geological storage project and on the Frio Shale outside Houston. Emphasis is taken on long term reaction kinetics and reactive transport modelling by diffusive transport to see how much of the cap rock mineralogy that is likely to be affected by the CO_2 plume.

2. Theory

2.1 Geological Storage and Sequestration of CO_2

Geological sequestration is the process where CO_2 goes through gas separation, transport and compression processes before it is re-injected into geological storage formations where it is stored for at least thousands of years (Nguyen 2003). This technology is often referred to as CCS. Already in the 1970s it was suggested that CO_2 storage could be utilized to reduce emissions of carbon fuelled energy, but the idea was dismissed. The idea did not become popular before the early 1990s (IPCC 2005).

Sleipner West was the world's first industrial-scale storage project which commenced in 1996 (Chadwick et al. 2004). More storage projects in various locations around the world have been introduced since then and others are in the developing phase today. In the last 15 years CO_2 storage has gone from a controversial and limited area of interest to a promising and important mitigation option (IPCC 2005). The success of these pioneering projects is today regarded as paramount for the future of geological storage of CO_2 as a way of reducing greenhouse gas emissions.

2.2 CO_2 Injection Process

CO_2 is generally injected into reservoirs at depths greater than 800 meters in a supercritical state. These reservoirs are most likely to be sandstone dominated. They are also likely to be confined by a sealing cap rock. Schematics of the injection process in various settings are shown in Chapter 2.4.

CO_2 is in a supercritical state when temperature and pressure are above the critical temperature of 31.1 °C and critical pressure of 7.39 MPa (Kaszuba et al. 2003). This state is

important for CO_2 storage because the density is favourable compared to the gas or liquid state. When CO_2 is supercritical it acts both as a gas and a liquid and can occupy the same pores that a less dense gas would, but it won't split into two phases as long as it is kept above the critical temperature and pressure. Therefore, CO_2 is most often injected at formation depths where it keeps these properties (IPCC 2005).

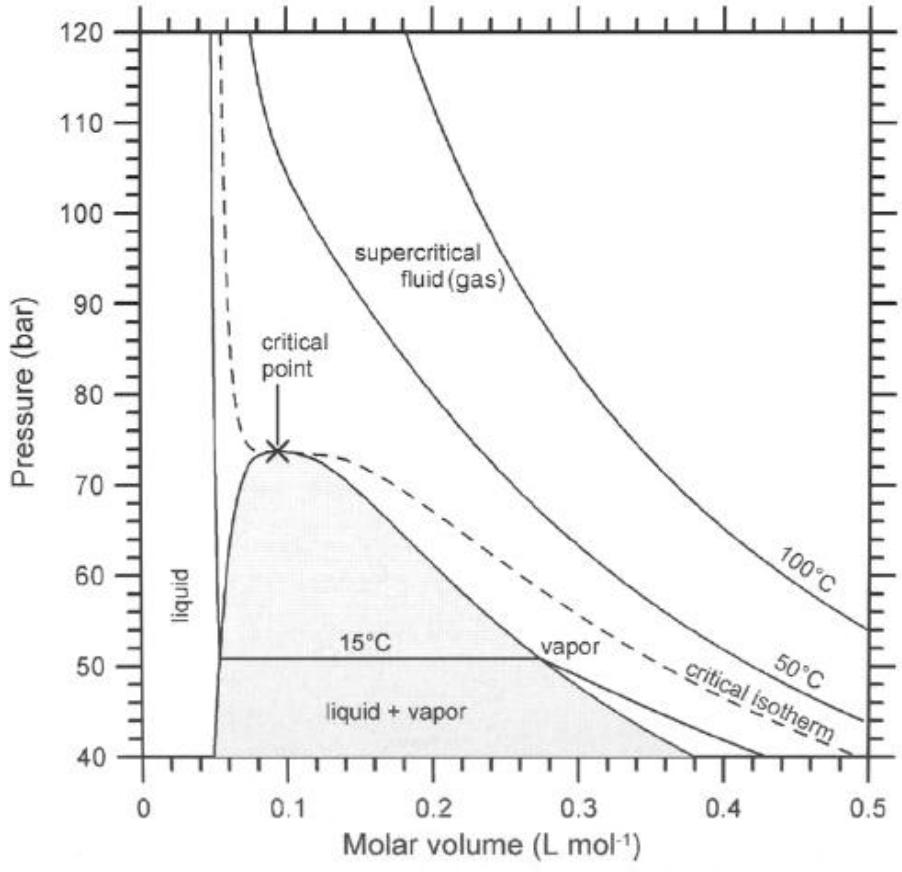

Figure 2.1: Simplified PV diagram for CO_2 (Marini et al. 2006).

Another advantage is that supercritical CO_2 is more stable than the gaseous CO_2 (Jasinge and Ranjith 2011). Supercritical CO_2 has a density of 400-700 kg/m^3 (Figure 2.2), which in most cases are less dense than the surrounding formation (unless it is a gas reservoir, where CO_2 is denser than the natural gas). Since the supercritical CO_2 is still less dense than the surrounding aquifer the CO_2 will rise buoyantly until it is trapped by an overlying seal (Shukla et al. 2010).

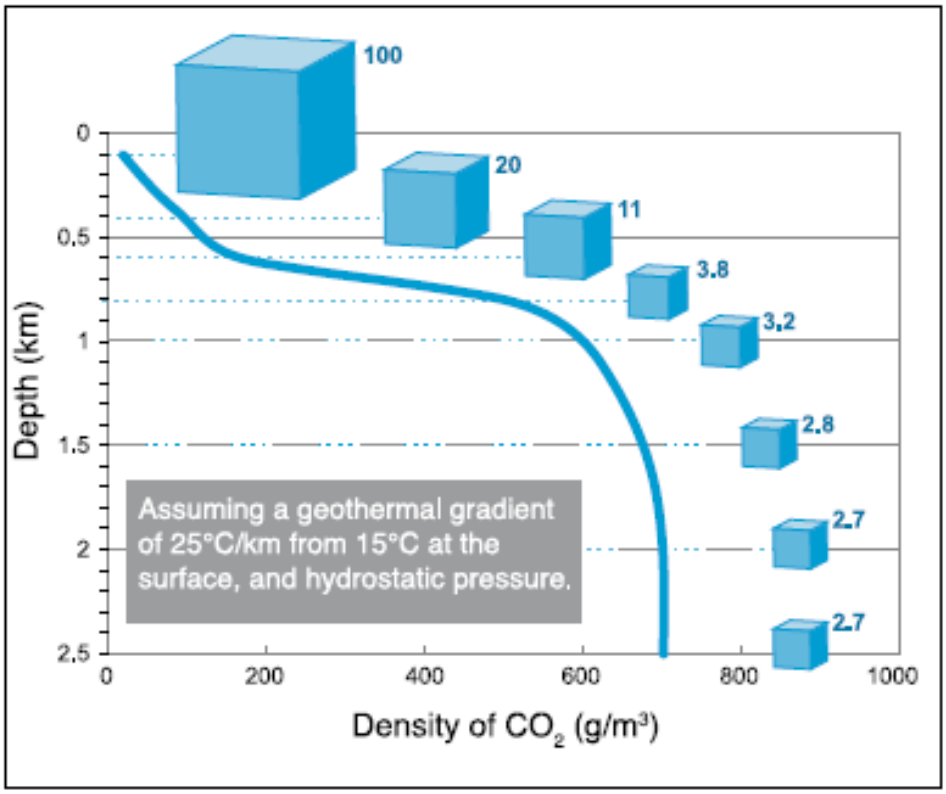

Figure 2.2: Density of injected CO_2 with assumed geothermal gradient of 25°C/km, surface temperature of 15°C and hydrostatic pressure (IPCC 2005).

An important monitoring parameter during CO_2 injection is the injection pressure (Li et al. 2006). Pressure build-up can potentially reduce the estimated storage capacity in saline aquifers. Production of hydrocarbons relieves pressure build-up but this is not the case for saline aquifers, which do not have hydrocarbons.

2.3 Storage Mechanisms

When buoyant CO_2 accumulates beneath the cap rock, a combination of physical and chemical trapping mechanisms work together to ensure that the CO_2 does not migrate from the reservoir for at least thousands of years (IPCC 2005). In the most desirable conditions the buoyant CO_2 plume is immovable under a thick and low-permeability cap rock, where a fraction of the injected volume is dissolved and later converted to carbonate minerals.

2.3.1 Physical Trapping Mechanisms

Physical trapping involves storage of CO_2 while keeping the physical properties it had during start of injection (IPCC 2005). Structural traps are formed by weathered rocks that acts as primary trapping mechanisms. These traps exist in most storage scenarios (IPCC 2005, Jasinge and Ranjith 2011). Structural traps are in most cases overlying barriers that prevent CO_2 from further upward migration. However, faults that exist close to a storage site can potentially provide leakage pathways for CO_2 flow (IPCC 2005).

Hydrodynamic trapping, or residual trapping, is another form of physical trapping that is often present in saline formations where fluid flows very slowly (IPCC 2005). The aquifer effectively blocks some of the CO_2 from further migration and consequently traps it within the sealing formation as residual CO_2 saturation. Hydrodynamic trapping is sometimes present without an overlying seal, and is in such cases the primary trapping mechanism (Gorecki et al. 2009). Hydrodynamic traps also have the potential of leaking if they are not properly sealed (Soong et al. 2004).

2.3.2 Geochemical Trapping Mechanisms

When the CO_2 plume is stagnated in the reservoir beneath the cap rock some of it will eventually begin to dissolve in the formation water. This process is called solubility trapping (IPCC 2005). When CO_2 dissolves in the formation water, the following reactions take place (Appelo and Postma 2005)

1) Gaseous CO_2 → aqueous CO_2:

$$CO_{2(g)} \rightarrow CO_{2(aq)} \quad \text{(C-1)}$$

2) Dissolved CO_2 → carbonic acid:

$$CO_{2(g)} + H_2O \rightarrow H_2CO_3 \quad \text{(C-2)}$$

3) The overall reaction:

$$CO_{2(g)} + H_2O \rightarrow H_2CO_3^* \quad \text{(C-3)}$$

where $H_2CO_3^*$ is the sum of $CO_{2(aq)}$ + H_2CO_3. For precipitation reactions the arrows would have gone the opposite way. The solubility of CO_2 in water has been shown to depend on temperature, pressure and salinity (Figure 2.3).

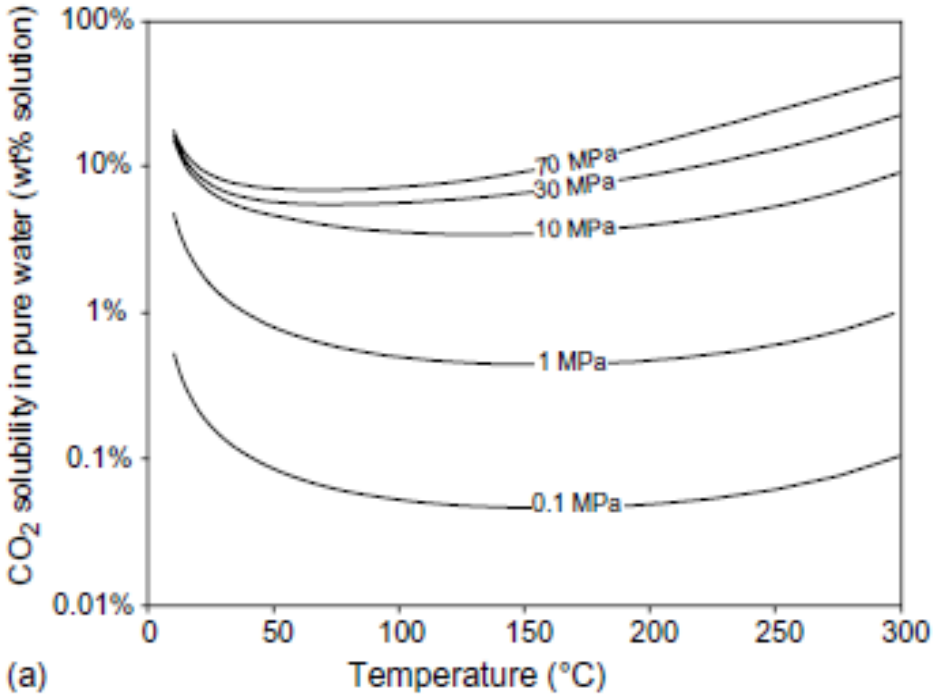

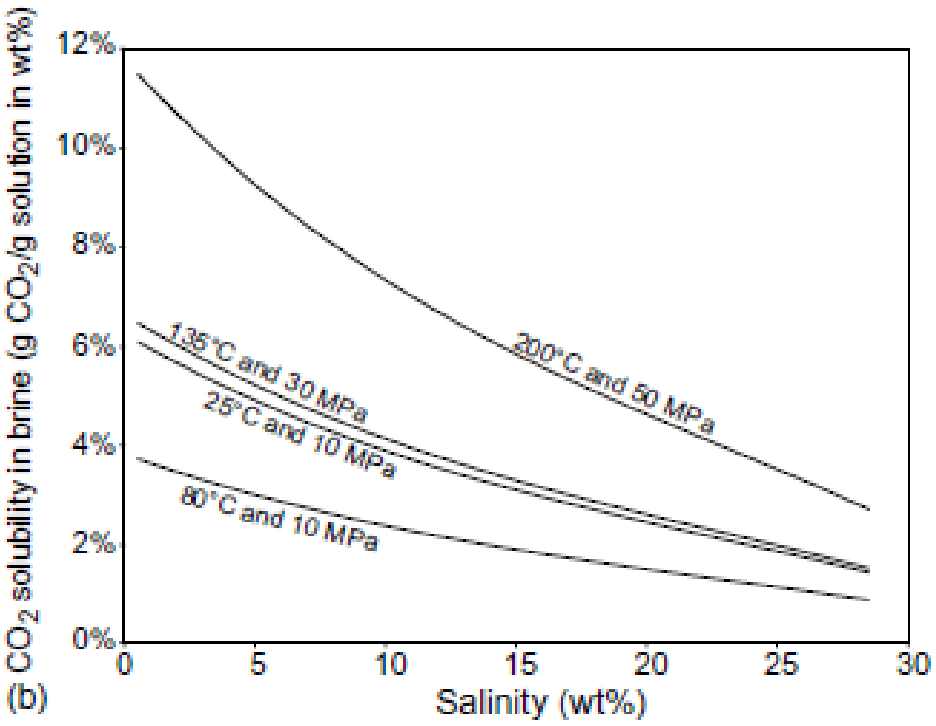

Figur 2.3: CO_2 solubility in water dependent on temperature and pressure (a), and salinity (b) (Bachu and Adams 2003).

As the rock dissolves ionic species will form and pH rises (IPCC 2005). A part of the dissolved CO_2 can be involved in precipitation of secondary carbonate minerals that may permanently store CO_2. This trapping mechanism is known as mineral trapping and is a very slow process that can take thousands of years, or even longer. Since mineral trapping involves permanent trapping of CO_2 it is regarded as the safest way of long-term storage.

2.4 Storage Options

Storage of CO_2 can be conducted in various settings, including depleted oil and gas fields which often involves EOR-processes, deep saline aquifers and coal seams (Figure 2.4). These settings vary in size, composition, and storage capacity, but are regarded as the most realistic and safe environments to be utilized for permanent CO_2 storage now and in the near future.

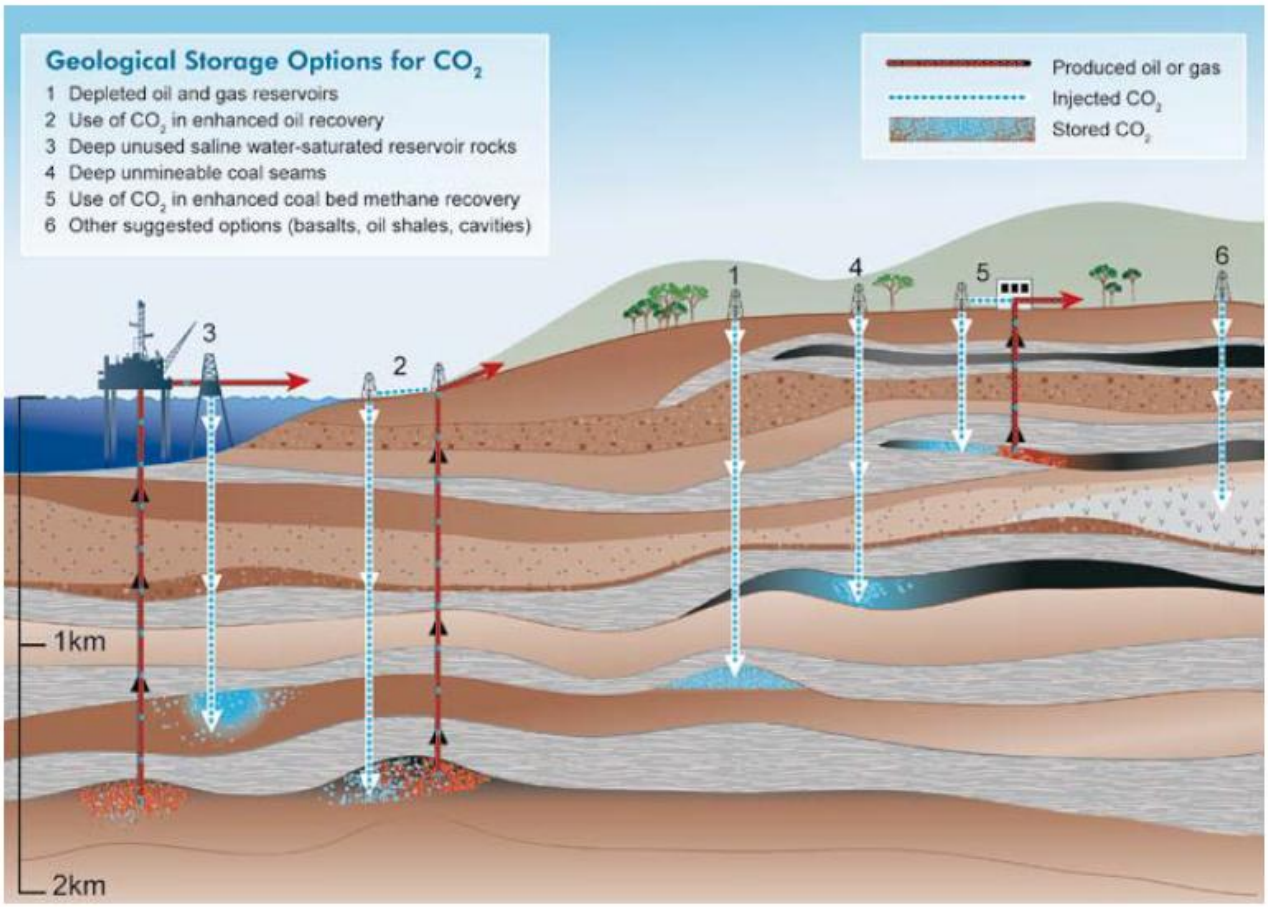

Figur 2.4: Options for CO_2 Storage (IPCC 2005).

2.4.1 Depleted Oil and Gas reservoirs Including CO_2-EOR and CO_2-EGR

Mature sedimentary basins are good storage sites. Some of the mature fields are depleted or nearing depletion. These sites have been explored, studied and produced, which indicates existence of a successful seal. In addition, these sites may already contain the infrastructure needed for CO_2 transport and injection (IPCC 2005). Global estimates of the storage capacity in oil reservoirs vary from 126-400 $GtCO_2$. For depleted gas reservoirs the storage capacity is estimated to 800 $GtCO_2$.

Depleted oil reservoirs are considered as promising and safe locations for storage of CO_2 (Jasinge and Ranjith 2011). When combined with CO_2-EOR injected CO_2 will also yield extra production of hydrocarbons and thus relieve pressure build-up, together with the obvious added economical benefit. Although CO_2-EOR only accounts for 0.3 % of the world's total oil production, the global storage potential of CO_2-EOR is estimated to lie within the

range of 61-123 $GtCO_2$ (Nguyen 2003, IPCC 2005). This translates to a global average incremental oil production of 13.2 % (IPCC 2005). A challenge remains to optimize CO_2-EOR for CO_2 storage (Sahin et al. 2012).

In CO_2-EOR the carbon dioxide is stored due to the injected CO_2 being trapped by capillary forces and other mechanisms within the pore spaces that are previously occupied by reservoir fluid. When assessing the storage capacity of a project it is often assumed that all pore space previously occupied by hydrocarbons can be utilized to store CO_2. Research suggests that this might not always be the case, as some residual water saturation may be present because of capillary forces and water influx, which will ultimately reduce the estimated storage capacity (Bachu et al. 2004).

CO_2-EOR can be performed either during miscible (or near miscible) temperature and pressure conditions where the CO_2 mixes and dissolves in the oil to enhance oil production, or at immiscible temperature and pressure conditions where CO_2 flows above the oil and increases the amount of oil recovery by gravity displacement (Sweatman et al. 2011). Some of the CO_2 is permanently trapped in the reservoir in a CO_2-EOR process, while the rest is reproduced until the field is abandoned (Sahin et al. 2012). All of the CO_2 is stored in the geological formation after completion unless some of it is needed for other purposes.

Depleted gas reservoirs are also regarded as very safe for CO_2 storage purposes. This is because the natural gas has been stagnated in these reservoirs for thousands of years, indicating presence of a sealing cap rock (Jasinge and Ranjith 2011). In CO_2-EGR projects CO_2 is primarily used for pressure support to prevent subsidence and water intrusion (Sweatman et al. 2011). CO_2 is stored in the pores previously containing natural gas.

2.4.1.1 Weyburn-Midale CO_2-EOR Project (Canada)

The Weyburn-Midale CO_2-EOR project is one of the world's largest commercial storage sites, located in Saskatchewan, Canada. It is a CO_2-EOR project where the purpose is to increase the amount of heavy oil recovery from a depleted carbonate reservoir where hydrocarbons

have been produced for 50 years (Cantucci et al. 2009). CO_2 is injected into the two reservoirs at 59°C and 1 500 meters depth.

CO_2 injection started in the year 2000 and ten years later approximately 16 Mt of CO_2 had been stored in the reservoir (Whittaker et al. 2011). CO_2 injection will possibly continue until 2035 and beyond. Oil production has increased by 60 %, yielding ca 155 million barrels of incremental oil recovery. Injection into the adjacent Midale Oil Field was started five years later in 2005. By 2010, 2 Mt of CO_2 had been stored at this location and it is estimated that injection will last 30-40 years with 60 million barrels of incremental oil production.

2.4.2 Deep Saline Aquifers

Deep saline aquifers holds the largest potential storage capacity, which is thought to be at least 1 000 $GtCO_2$, possibly as high as 10 000 $GtCO_2$ (IPCC 2005). Capacity estimations of saline aquifers are notoriously difficult because of the interplay between different trapping mechanisms operating at different time scales, and limited availability of seismic data. Current estimations are based on discovered fields, but could be 25 % higher if undiscovered fields are taken into account. This is also the case for the other storage options.

Aquifers that are too saline to be considered as drinkable groundwater are called deep saline aquifers (Gorecki et al. 2009). These aquifers are porous and permeable rock formations generally found at depths greater than 800 meters where CO_2 acts supercritical. CO_2 in this condition is immiscible with the formation water (IPCC 2005). Buoyancy drive in saline formations is strong because of the density differences between the supercritical CO_2 and the surrounding aquifer are large (30-50%). Storage mechanisms related to deep saline aquifers include structural trapping, hydrodynamic trapping and mineral trapping (Xie and Economides 2009).

A significant challenge related to storage of CO_2 in deep saline aquifers is pressure build-up that occurs since no fluids are produced. Such pressure build-ups and potential fracturing can cause severe CO_2 leakage. Because of these risks the pressure build-up is a limiting factor for

the storage capacity, meaning that the actual capacity can be less than the initial potential estimate.

2.4.2.1 Sleipner West (Norway)

Sleipner became operational in 1996, and as the first offshore commercial-scale injection site in the world the Sleipner project is a pioneer within CO_2 storage in deep saline aquifers. It is located on the Norwegian Continental Shelf, where carbon dioxide is injected into the extremely large Utsira Sand formation at a depth between 700-1000 meters (Figure 2.5) with a rate of approximately 1 Mt/year (Gaus et al. 2005). CO_2-rich natural gas is produced from a reservoir located at a depth of 3 500 meters, and the CO_2 content must be reduced to meet government regulations before the natural gas can be sold.

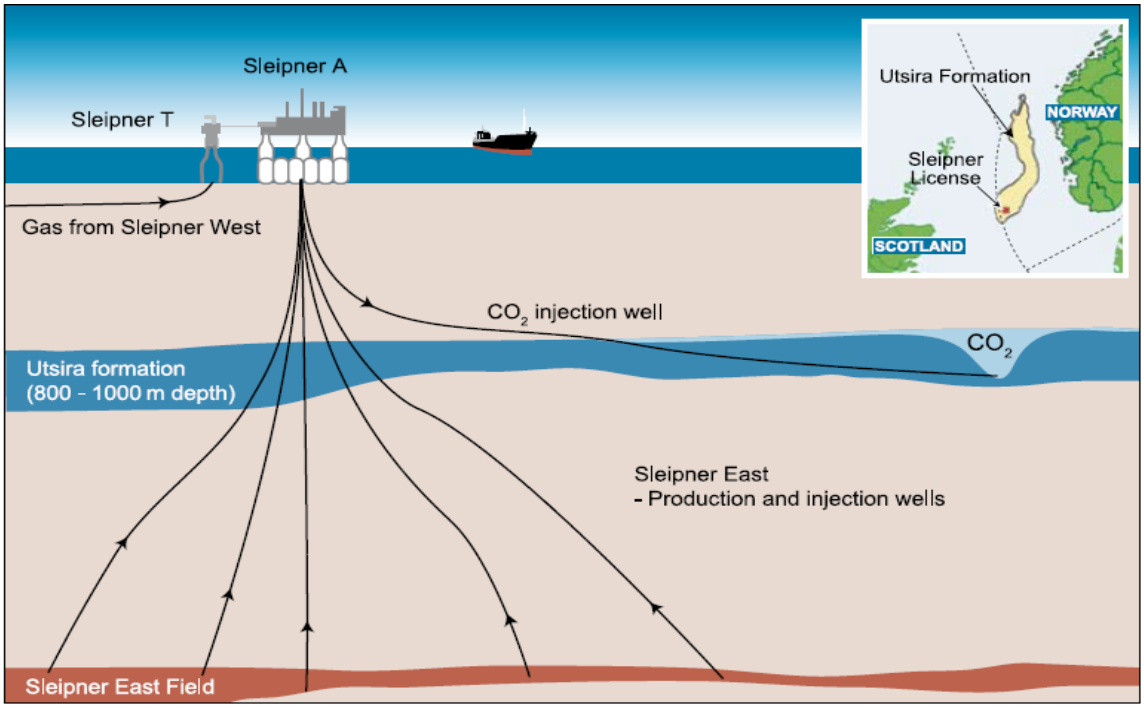

Figure 2.5: Schematic of the Sleipner project (IPCC 2005).

The Utsira Sand formation has inter-fingering layers of shale or clay that influences the movement of the CO_2 plume (Shukla et al. 2010). Above the aquifer the Nordland Shale cap rock prevents the CO_2 from migrating to the ocean floor. Nordland Shale is a 200-250 meters

thick cap rock with a porosity of 5-10 % (Gaus et al. 2005, Audigane et al. 2006). A total amount of almost 12 $MtCO_2$ was stored as of 2011 (Statoil).

2.4.2.2 The In Salah Gas Project (Algeria)

The In Salah Project is located in Algeria and was the world's first industrial-scale CO_2 storage project in a gas reservoir (IPCC 2005). The project became operational in 2004 and involves re-injecting produced CO_2 from the natural gas into the Krechba carboniferous sandstone, which is a 20 meter thick aquifer located at a depth of 1 900 meters (Figure 2.6). Natural gas containing up to 10 % of CO_2 is reduced to at least 0.3 % before it is sold (Wright 2007). CO_2 is injected in horizontal wells at a rate of 1.2 $MtCO_2$ per year (IPCC 2005). Approximately 17 $MtCO_2$ will be stored, which translates to a cost of 6 dollar/ton CO_2 avoided.

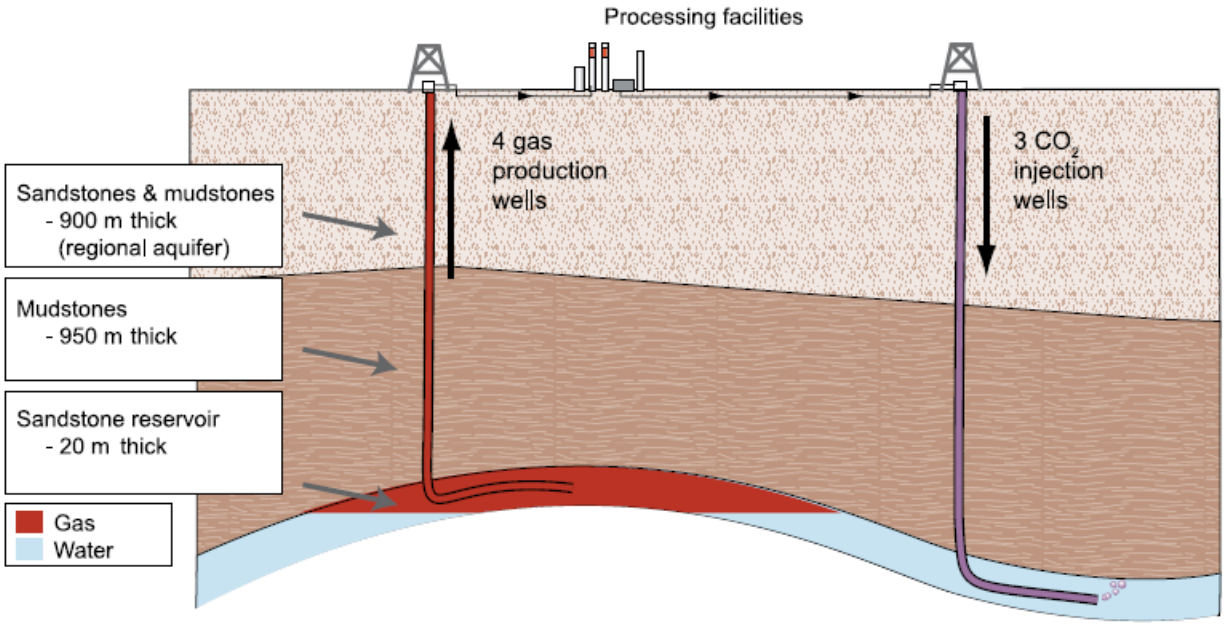

Figure 2.6: Schematic of the In Salah Gas Project storage site (IPCC 2005).

2.4.3 Coal Seams

Coal has fractures that alter the permeability of the coal seams. Gas molecules diffuse into micro-pores located between these fractures and strongly adsorb onto the coal, which is the main trapping mechanism in such storage environments (IPCC 2005). Storage capacity is determined by the coal thickness, CO_2 adsorption isotherms, recovery factor and completion factor (Xie and Economides 2009). When CO_2 interacts with coal beds there will be adsorption and desorption of gases that were previously adsorbed on the coal as well as shrinking and swelling of the coal. The global storage capacity is thought to lie between 60-200 $GtCO_2$ (IPCC 2005). However, assuming that CO_2 will only be stored in coal seams when recovering coal bed methane the theoretical storage capacity is reduced to 3-15 $GtCO_2$ (Xie and Economides 2009, IPCC 2005).

2.4.3.1 The Allison Unit CO_2-ECBMR Pilot (USA)

CO_2 injection lasted from April 1995 until the year 2001 with the purpose of enhancing coal bed methane recovery (IPCC 2005). The Allison unit is located in the San Juan Basin in USA and has a CBM resource estimated to be 242 million m^3/km^2. CO_2 was injected into a 13 meter thick reservoir at a depth of 950 meters. After six years of injection 270 000 ton CO_2 had been stored. Although methane recovery increased from 77 % of IGIP to 95 % of IGIP, incremental methane recovery was reduced and project cost escalated due to a significant permeability reduction .

2.4.4 Other Storage Options

Basalts, oil and gas rich shale, salt caverns and abandoned mines have also been investigated by means of CO_2 storage, but these will not be discussed any further.

2.5 Factors Affecting the Cap Rock Sealing Integrity

Many factors can affect the cap rock sealing integrity during CO_2 storage. These may be short-term or long-term factors and are identified as anthropogenic factors, geomechanical factors and geochemical factors.

2.5.1 Anthropogenic Factors

Anthropogenic factors include human interventions in the subsurface. These factors are abandoned wells and hydrocarbon production, which may contribute to leakage. Abandoned wells that penetrates the geological formation occupied by CO_2 is most interesting, because they may create pathways for CO_2 migration (Celia et al. 2004).

2.5.2 Stratigraphic Factors

The cap rock is integral when it comes to CO_2 storage. It is generally a low-permeable and low-porosity rock formation that overlies a weaker and more permeable formation, such as sandstone or chalk. The cap rock is typically shale or clay. In relation to CO_2 storage the cap rock is often very thick and dense (Gaus et al. 2005). In most cases the cap rock provides a vertical barrier against fluid flow. The cap rock strength is therefore important.

In geological storage situations it is the lower part of the cap rock that is most realistically affected by reactions taking place between the CO_2 and the surrounding formation water and mineralogy (Chapter 6). Thus, if the cap rock is uniform in the lower region over a large distance there is less chance of leakage. In such cases the most important stratigraphic factors include physical rock strength, faults, fractures, wells and CO_2-rock-brine interactions (IPCC 2005).

2.5.3 Geomechanical and Geochemical Factors

Injection of CO_2 into porous and permeable reservoirs may cause the reservoir and cap rock to deform because of pressure differences. Consequently, fractures and faults may re-activate. Knowledge of formation water composition, mineralogy, in-situ stresses, pore fluid pressures and pre-existing faults are necessary to model geomechanical and geochemical changes in the geological formation. These properties interplay and can either enhance or degrade the cap rock sealing integrity (Johnson et al. 2004). The geomechanical factors are prominent during the injection phase, whereas geochemical reactions take place independently of CO_2 injection and potentially keep reacting for thousands of years.

Geochemical reactions involve the dissolution of CO_2 and subsequent forming of carbonic acid (C-2), which leads to dissolution of bicarbonate ions $\left(HCO_3^-\right)$and finally carbonate ions $\left(CO_3^{2-}\right)$. CO_2 dissolution causes the formation water to become acid, and in time the low pH will slow down and reduce the amount of CO_2 that can dissolve. Formation rocks may then subsequently act as a pH buffer and store CO_2 as a dissolved phase, $CO_{2(aq)}$, which can then promote geochemical reactions with the surrounding minerals (IPCC 2005). Precipitation of carbonates can alter the cap rock properties and trap CO_2 as solid phases.

3. Background

3.1 General Introduction to Reaction Chemistry between Minerals and Water

Minerals present in an aquifer can be pure phases or a mix between solid solutions of different minerals (Appelo and Postma 2005). Solubility varies between minerals, with some reactions being quicker than other. Calcite, gypsum, fluorite and halite are among the most soluble minerals. Silicate minerals on the other hand are more complex and less soluble. At low temperatures, equilibrium of silicate minerals may never be reached. The law of mass action describes equilibrium in water, and states that (Appelo and Postma 2005):

$$aA + bB \leftrightarrow cC + dD \qquad \text{(Eq. 1)}$$

the equilibrium distribution of the species is given by:

$$K = \frac{[C]^c[D]^d}{[A]^a[B]^b} \qquad \text{(Eq. 2)}$$

where *K* is the equilibrium constant, and *A, B, C* and *D* are the activities (effective concentrations).

The law of mass action is only valid for the activity of ions. Activity is a dimensionless factor that shows how a given ion would behave in a solution where it was the only reacting ion. This size is given relative to a standard state. The standard state in an ideal aqueous solution has a solute concentration of 1 mol/kg H_2O. An activity coefficient corrects for this ideal behaviour:

$$[i] = \frac{\gamma_i \cdot m_i}{m_i^0} \equiv \gamma_i \cdot m_i \qquad \text{(Eq. 3)}$$

[i] is the dimensionless ion activity, γ_i is the dimensionless activity coefficient, m_i, is the molality (mol/kg H_2O) and m_i^0 is the standard state (1 mol/kg H_2O).

The empirical formula for activity coefficients is only valid for a given ionic strength, which is the concentration of ions in a solution. Formation waters suitable for CO_2 storage have ionic strengths above 0.5. In such situation the Davies equation is valid, which is also utilized by the simulation programme PHREEQC (Parkhurst and Appelo 1999):

$$\log \gamma_i = -A_i^2 \left(\frac{\sqrt{I}}{1+\sqrt{I}} - 0.3I \right) \qquad \text{(Eq. 4)}$$

A is a temperature dependent constant (at 25°C: A = 0.5085), z_i is the ion charge number and I is the ionic strength.

The Saturation index of a given mineral indicates whether the mineral tends to dissolve or precipitate:

$$SI = \log \frac{IAP}{K} \qquad \text{(Eq. 5)}$$

K is the activity of a given mineral at equilibrium, while *IAP* is the ionic activity product.
For calcite, $CaCO_3$ the activities are:

$$K_{Calcite} = [Ca^{2+}][CO_3^{2-}] \qquad \text{(Eq. 6)}$$

$$IAP_{Calcite} = [Ca^{2+}][CO_3^{2-}] \qquad \text{(Eq. 7)}$$

For *SI* = 0 the mineral is and solution is at equilibrium
For *SI* > 0 the mineral is supersaturated in the solution
For *SI* < 0 the mineral is undersaturated in the solution

3.2 Concept of Equilibrium and Kinetics

Equilibrium calculations are often used as initial steps in aquifer chemistry. Equilibrium is the concentration of a given chemical species obtained when it has finished reacting. Kinetic calculations utilize reaction rates to see how the concentration of the chemical species changes with time. Dissolution and precipitation of minerals can be explained by rate formulas.

3.3 Reaction Rates

Kinetic calculations uses the concept of utilizing rates and how they change with time. Consider a very simple environment consisting of two compounds A and B (Eq. 8). When compound *A* changes to compound *B* within a given time, the reaction rate is the change of *A* with time (Appelo and Postma 2005). The slope of the tangent determines the reaction rate (Eq. 9).

$$A \rightarrow B \qquad \text{(Eq. 8)}$$

The rate for the whole curve is:

$$\text{rate} = \left[\frac{-d_{C_A}}{dt} \right] \qquad \text{(Eq. 9)}$$

A general expression for an order reaction is:

$$\text{rate} = k[A]^m \qquad \text{(Eq. 10)}$$

where *k* is the rate constant, which is equal to the reaction rate when all reactants are at unit concentrations, *[A]* is the concentration of the reactant and *m* indicates the order of the reaction. In complex settings the reaction rates are likely to be proportional to fractional orders of the concentrations of reacting molecules (Marini 2006):

$$\frac{1}{V}\cdot\frac{1}{c}\cdot\frac{dn_C}{dt} = k\cdot C_A^{\alpha}\cdot C_B^{\beta} \qquad \text{(Eq. 11)}$$

V is the volume of the system, C_A and C_B are concentrations of A and B respectively, k is the independent rate constant, and α and β defines the order of the reactions with respect to A and B respectively and k is the independent rate constant.

3.3.1 Temperature Dependence of Rate Constants

Almost every geochemical reaction is influenced by temperature. The rates generally increase rapidly with increasing temperature, shown by the Arrhenius equation (Marini 2006):

$$k = A_a\cdot\exp\left(-\frac{E_a}{RT}\right), \qquad \text{or} \qquad \ln k = \ln A_a - \frac{E_a}{RT} \qquad \text{(Eqs. 12 and 13)}$$

where A_a is the so-called pre-exponential factor (same units as k), E_a is the activation energy (kJ/mol), R is the universal gas constant and T the absolute temperature.

3.4 CO_2-Rock-Brine Interactions

Acidification of the formation water due to dissolved CO_2 promotes various geochemical reactions. These reactions may completely alter the mineralogy of the lower part of the cap rock. Storage environments contain various minerals, including silicates and carbonates who play their parts in the integrity of the cap rock. The following subchapters give an introduction to dissolution and precipitation mechanism of these minerals.

3.4.1 Dissolution and Precipitation of Minerals

When dissolved CO_2 is in contact with surrounding rocks some minerals will consequently dissolve or precipitate. Dissolution and precipitation of solid minerals are functions of the many processes taking place simultaneously at different rates. The precipitation of a mineral is built up in stages. Nucleation is the first stage of the formation of a new mineral. In this stage ions accumulate in a cluster on an existing surface or on a new surface. Nucleation will not necessarily lead to the formation of a crystal, but a crystal cannot form unless nucleation takes place. The nucleation could either be homogeneous, identified by forming in solution, or heterogeneous when forming on an already existing surface (Marini 2006).

Crystal growth is the second process that eventually leads to the creation of a new solid. The rate of the slowest process governing the growth of a crystal is said to be the controlling growth mechanism (Marini 2006). Three controlling mechanisms exist, including surface-controlled, transport-controlled or intermediate-controlled crystal growth. Surface-controlled crystal growth indicates that advection and diffusive transport of particles to the growth site happens faster than addition of solute particles. For transport-controlled crystal growth it is the opposite and advection and diffusion are the slowest mechanisms contributing to the crystal growth. For intermediate-controlled crystal growth both transport and addition of solute particles to the growth surface controls the precipitation rate. Dissolution, on the other hand, differs from precipitation in the way that the minerals already exist when the dissolution process starts. As for precipitation the dissolution of minerals can be either surface-controlled, transport-controlled or controlled by both of them.

Diffusion transport is essential to the reactive transport modelling (Chapter 6) and can be identified by the transport of a given ion, i.e., Ca^{2+}, from an area of high concentration to an area of low concentration. This transport mechanism is important in the case of geological storage since it can involve transport of ions from the reservoir to the cap rock or vice versa, possibly implementing a change in the porosity and permeability of the lower cap rock. Diffusion can thus be an important factor for the long-term integrity of the cap rock. A simple formula, called Fick`s law for diffusion in sediments, is shown below (Domenico and Schwartz 1990):

$$J = -D_d' \, \mathrm{grad}(C) \qquad \text{(Eq. 14)}$$

where J is the diffusional flux (mol/m^{2}s), D'_d is the effective diffusion coefficient (m^2/s) and C the concentration (mol/m^3) of a given species.

Rate laws that describe the mineral dissolution and precipitation kinetics are vast in existence. Literature contains a host of different rate equations. They are sometimes controversial because they may appear inconsistent. However, for the simulation study the following rate equation is utilized (Lasaga 1984):

$$\text{rate}_m = A_m k(T)_m (a_{H+})^n \left[1 - \left(\frac{Q_m}{K_m}\right)\right] \qquad \text{(Eq. 15)}$$

where *rate* is the rate of dissolution/precipitation (positive if dissolution, negative if precipitation), *m* is the given mineral, *A* is the reactive surface area (m^2/kgw), *k(T)* is the temperature dependent rate constant, a_{H+} is the proton activity, *n* is the order of the reaction (here: $0 \leq n \leq 1$), *K* is the equilibrium constant for the mineral water reaction given for dissolution of 1 mol of mineral *m*, and *Q* is the ion activity product, IAP. An important assumption for this formula is that precipitation rate equals the dissolution rate.

The temperature dependent rate constant is given by the following (Lasaga 1984):

$$k(T) = k_{25} \exp\left[\frac{E_a}{R}\left(\frac{1}{T} - \frac{1}{298.15}\right)\right] \qquad \text{(Eq. 16)}$$

E_a is the activation energy (J/mol), k_{25} is the rate constant at 25°C (mol/m^{2}s), R is the universal gas constant (8.31 J/mol K) and T is the absolute temperature (K).

Reactive surface area is an important parameter that needs further explanation. In mineral dissolution and precipitation not al of the surface takes actively part in the dissolution or precipitation process at a given time. The area of a mineral that is actively taking part in these processes is termed reactive surface area (Marini 2006). One major challenge is to determine this quantity. Often, the reactive surface areas of some minerals are so highly uncertain that they are set equal to other minerals that have better known quantities (Xu et al. 2005).

3.5 Silicates

Silicates are commonly present in sandstone reservoirs and cap rocks suitable for geological storage (Gaus et al. 2005, Xu et al. 2005). Several sub-categories of silicate groups exists, however a detailed description of them is not given here. Rather, focus will be on silicate minerals from the Sleipner and Frio fields, which the simulation study is based on.

The dissolution process of silicates is dependent upon the type of silicates, but can generally be represented by divalent ion-proton exchange (Ca^{+2}, Mg^{+2}). When the Ca-O, and Mg-O bonds are broken, the mineral will break entirely (Marini 2006). Most silicates experience the lowest rates near neutral pH levels, whereas the more acid or more alkaline the solution gets the faster the reaction goes.

Dissolution of silicates is also a very important pH-buffer in the rock matrix, meaning that the pH will rise correspondingly when silicates dissolve. Precipitation of secondary silicates is in contrast to dissolution of primary silicates a relatively fast process (Helgeson et al. 1969). Some silicate weathering reactions are presented in Table 3.1., with the mineral kaolinite as reaction product:

Table 3.1: Silicate weathering, with kaolinite as reaction product (Appelo and Postma 2005).

Albite → Kaolinite
$2\ NaAl_3Si_3O_8 + 2\ H^+ + 9\ H_2O \rightarrow Al_2Si_2O_5(OH)_4 + 2\ Na^+ + 4\ H_4SiO_4$
Anorthite → Kaolinite
$CaAl_2Si_2O_8 + 2\ H^+ + H_2O \rightarrow Al_2Si_2O_5(OH)_4 + Ca^{2+}$
K-feldspar → Kaolinite
$2\ KAlSi_3O_8 + 2\ H^+ + 9\ H_2O \rightarrow AlSi_2O_5(OH)_4 + 2\ K^+ + 4\ H_4SiO_4$

3.6 Carbonates

Carbonate minerals have a special position in terms of CO_2 storage by potentially precipitating and permanently trap an amount of the dissolved CO_2. Carbonate minerals involved in this process in the simulation study include calcite, magnesite, siderite, dolomite, and dawsonite (Gaus et al. 2005, Xu et al. 2005). Most carbonates form from bacterial degradation. Calcite ($CaCO_3$) is perhaps the carbonate mineral that is most extensively studied. The precipitation reaction of calcite is (Berner and Lasaga 1983):

$$Ca^{2+} + 2HCO_3^- \rightarrow CaCO_3 + H_2O \qquad \text{(C-4)}$$

The dissolution reaction involves the same reactants and products, but the reaction goes in the opposite direction. Calcite experiments have shown that dissolution is dependent of pH at low temperatures, but at neutral and alkaline pH the dissolution rate is independent of pH (Rickard and Sjöberg 1983). In geological storage situations the injected CO_2 decreases the pH significantly. This leads to dissolution of calcite, which acts as a buffer to the carbonate system (Chapter 5). After some time, calcite is likely to precipitate and contribute to mineral trapping. Precipitation reactions for thesis relevant carbonates are listed in Table 3.2.

Table 3.2: Carbonate precipitation reactions.

Mineral Name	**Precipitation Reaction**
Dolomite	$Ca^{2+} + Mg^{2+} + 4HCO_3^- \rightarrow 2CO_2 + CaMg(CO_3)_2 + 2H_2O$
Magnesite	$Mg^{2+} + 2HCO_3^- \rightarrow CO_2 + MgCO_3 + H_2O$
Siderite	$Fe^{2+} + 2HCO_3^- \rightarrow CO_2 + FeCO_3 + H_2O$
Dawsonite	$Na^{2+} + Al^{3+} + 4HCO_3^- \rightarrow 3CO_2 + NaAlCO_3(OH)_2 + H_2O$
Ankerite	$Ca^{2+} + 0.3Mg^{2+} + 0.7Fe^{3+} + 4HCO_3^- \rightarrow 2CO_2 + CaMg_{0.3}Fe_{0.7}(CO_3)_2 + 2H_2O$

4. Simulation Method and Data

Geochemical simulations of two storage sites, Sleipner and Frio, are performed with the simulation programme PHREEQC Interactive V2.18.5570. The purpose is to analyze the geochemical reactions taking place in the cap rock during CO_2 storage. Both batch modelling and coupled batch modelling and reactive transport modelling are performed on the two storage sites. In the following a general introduction to the model and simulation descriptions relevant for the thesis will be discussed, including input data.

4.1 Introduction to PHREEQC Interactive V2.18.5570

PHREEQC is a geochemical simulation tool that can perform both batch modelling and 1D reactive transport among other simulations not relevant for this thesis. The model was originally designed for the purpose of groundwater analyses, where temperature and pressure are generally lower than the required settings of CO_2 storage. However, later versions of PHREEQC are capable of simulating at destined reservoir conditions (Parkhurst and Appelo 1999).

PHREEQC is built up by simple keywords in which relevant input is defined. For example, the keyword SOLUTION is here used to define the formation water chemistry, properties and solution size, RATES uses rate equations (Eqs. 15-16) to compute the mineral rates, KINETICS utilizes RATES for kinetic batch simulations, EQUILIBRIUM_PHASES uses equilibrium theory to calculate final composition of minerals, whereas TRANSPORT is utilized for the reactive transport modelling. $CO_{2(g)}$ is introduced in GAS_PHASE. PHREEQC is evidently a tool that is logic and relatively easy to learn, but it requires adequate knowledge of geochemistry.

PHREEQC can utilize a total of ten databases for the geochemical reactions. The programme logic is that it uses dissociation reactions (Table A.1 in Appendix A) as background for the

dissolution and precipitation calculations of minerals, and all databases are thus built up in this way. After some initial experiments it was decided that llnl.dat was the database that worked best with the obtained data. This database is prepared by Jim Johnson at the Lawrence Livermore National Laboratory and includes an extensive mineral coverage (Parkhurst and Appelo 1999).

4.1.2 Validation of PHREEQC

It was originally scheduled to perform simulations with another model (PHAST or STARS) to validate PHREEQC. This was not possible due to limited time. A brief walkthrough of literature references that utilizes PHREEEQC in their work are described instead.

PHREEQC has previously been used to study cap rock integrity of the Sleipner Project (Gaus et al. 2005). Equilibrium batch modelling, kinetic batch modelling and reactive transport modelling were performed on the Nordland Shale cap rock. The study concluded that equilibrium batch modelling is unrealistic by means of CO_2 storage and thus that the kinetic approach should be chosen. The paper also concluded that diffusion transport is most likely to be a factor within the first 10 meters of the cap rock.

PHREEQC was also used in another CO_2 storage project (Pauwels et al. 2007) to estimate the quantities of carbon concentration, aluminium concentration and pH in a brine reconstruction project where these quantities were initially unknown. The geochemical model SCALE 2000 was also used and results were compared between the two models. The content of CO_2 in solution varied significantly from PHREEQC to SCALE 2000, however the latter is based on a Pitzer model that does not include aluminium speciation.

A book called "Geochemistry, Groundwater and Pollution" covers potential geochemical reactions occurring in groundwater aquifers (Appelo and Postma 2005). The book utilizes PHREEQC to visualize many of the potential reactions occurring in groundwater aquifers, and includes extensive examples that contain both the code setup and simulated results.

4.2 Cap Rock Mineralogy and Formation Water Properties

4.2.1 Nordland Shale

The initial primary mineralogy of Nordland is dominated by quartz, mica/illite, kaolinite and plagioclase (Table 4.1). Secondary minerals, which are minerals that are not present before CO_2 injection, are expected to include the carbonate minerals dawsonite, dolomite and magnesite (Table 4.2).

Table 4.1: Initial primary mineral assemblage of Nordland Shale (Gaus et al. 2005, Audigane et al. 2006).

Nordland shale composition	**Mass Percent**	**Minerals introduced in PHREEQC**	**Chemical formula of introduced mineral**
Mica/Illite	24.7	Muscovite	$KAl_3Si_3O_{10}(OH)_2$
Quartz	21.5	Quartz	SiO_2
Kaolinite	18.0	Kaolinite	$Al_2Si_2O_5(OH)_4$
Plagioclase	12.3	Albite	$NaAlSi_3O_8$
		Anorthite	$CaAl_{2(}SiO_4)_2$
Smectite	8.8	Smectite-high-Fe-Mg	$Ca_{025}Na_{0.1}K_{0.2}Fe^{2+}{}_{0.5}Fe^{3+}{}_{0.2}Mg_{1.15}Al_{1.2}Si_{3.5}H_2O_{12}$
Chlorite	4.1	Clinochlore-7A	$Mg_5Al_2Si_3O_{10}(OH)_8$
Pyrite	2.8	Pyrite	FeS_2
K-feldspar	2.1	K-feldspar	KAl_3SiO_8
Siderite	1.6	Siderite	$FeCO_3$
Mixed layer clay	1.4	Not used	
Calcite	1.0	Calcite	$CaCO_3$
Total	98.3		

Table 4.2: Secondary mineral assemblage of Nordland Shale (Gaus et al. 2005).

Secondary mineral assemblage	**Minerals introduced in PHREEQC**	**Chemical Formula**
Dolomite	Dolomite	$CaMg(CO_3)_2$
Dawsonite	Dawsonite	$NaAlCO_3(OH)_2$
Magneste	Magnesite	$MgCO_3$

The described mineralogy is derived from laboratory measurements. When introducing the minerals to PHREEQC the exact mineralogy must be defined. Laboratory measurements might not always provide this level of detail, so the minerals introduced in PHREEQC may therefore be somewhat different from the minerals described by laboratory measurements. Plagioclase, for instance, is a group of solid silicates where the exact mineral type is described by the amount of albite and anorthite present. Smectite is introduced as smectite-high-Fe-Mg, chlorite is represented by clinochlore-7A and mica/illite is represented by muscovite. These representations are selected based on previous work (Gaus et al. 2005, Audigane et al. 2006). Secondary mineral assembly (Table 4.2), initial formation water composition (Table 4.3) and initial formation water properties (Table 4.4) are also taken from these papers.

Table 4.3: Initial formation water composition of Nordland Shale (Gaus et al. 2005).

Elements	**Concentration (M)**
Al	3.51×10^{-8}
Ba	1.25×10^{-5}
C	6.92×10^{-5}
Ca	0.177
Cl	0.479
Fe	2.48×10^{-7}
K	1.42×10^{-4}
Mg	1.11×10^{-2}
Na	0.106
S	4.81×10^{-4}
Si	2.52×10^{-4}

Table 4.4: Initial formation water properties of Nordland Shale (Gaus et al. 2005).

Temperature (°C)	37
Pressure (atm)	100
P_{CO2} (atm)	52
pH	7.67
Ionic strength (mol/l)	0.647
Porosity	0.05

4.2.2 Frio Shale

Frio Shale is primarily dominated by clay minerals, including illite and na-smectite, but is also represented by a large portion of quartz and calcite (Table 4.5). The secondary mineral assemblage at Frio was assumed to be equal to the secondary mineral assemblage at Sleipner, with the addition to siderite (Table 4.6).

Table 4.5: Initial primary mineral assemblage of Frio Shale (Xu et al. 2005).

Frio Shale Composition	**Volume % of medium**	**Minerals introduced in PHREEQC**	**Chemical formula**
Illite	25.33	Muscovite	$KAlSi_3O_{10}(OH)_2$
Na-Smectite	20.70	Na-Monmorillonite	$Na_{0.33}Mg_{0.33}Al_{1.67}Si_4O_{10}(OH)_2$
Quartz	17.30	Quartz	SiO_2
Calcite	9.81	Calcite	$CaCO_3$
Oligoclase	4.75	Albite Anorthite	$NaAlSi_3O_8$ $CaAlSi_3O_8$
K-feldspar	4.27	K-feldspar	$KAlSi_3O_8$
Kaolinite	3.95	Kaolinite	$Al_2Si_2O_5(OH)_4$
Chlorite	2.12	Clinochlore-7A	$Mg_5Al_2Si_3O_{10}(OH)_8$
Kerogen-OS	1.8	Not used	$C_{64}H_{102}O_{40}S_{10}$

Table 4.6: Secondary mineral assemblage Frio Shale (Xu et al. 2005).

Mineral	**Minerals introduced in PHREEQC**	**Chemical formula**
Dawsonite	Dawsonite	$NaAlCO_3(OH)_2$
Magnesite	Magnesite	$MgCO_3$
Dolomite	Dolomite	$CaMg(CO_3)_2$
Siderite	Siderite	$FeCO_3$
Pyrite	Not used	FeS_2
Ankerite	Not used	$CaMg_{0.3}Fe_{0.7}(CO_3)_2$
Alunite	Not used	$KAl_3(OH)_6(SO_4)_2$
Low-Albite	Not used	$NaAlSi_3O_8$

Illite is represented by muscovite, Na-smectite is represented by Na-montmorillonite since it is introduced as such in the database, oligoclase is represented by the end-member plagioclase minerals albite and anorthite and chlorite is introduced as clinochlore-7A. Kerogen-OS is left out because it is not contained in the databases. The formation water elements are similar to that of Sleipner, with calcium, chlorine and sodium in addition to carbon dominating (Table 4.7). Temperature and pressure are higher at Frio Shale compared to Nordland Shale, and pH is one unit lower (Table 4.8).

Table 4.7: Initial formation water composition of Frio Shale (Xu et al. 2005).

Elements	**Concentration (M)**
Al	5.41×10^{-8}
C	0.92
Ca	6.57×10^{-2}
Cl	1.0
Fe	4.92×10^{-4}
K	5.60×10^{-5}
Mg	6.47×10^{-7}
Na	0.83
S	9.72×10^{-7}
$SiO2_{(aq)}$	5.89×10^{-4}

Table 4.8: Formation water properties of Frio Shale (Xu et al. 2005).

Temperature (°C)	75
Pressure (atm)	198
P_{CO2} (atm)	128
pH	6.69
Ionic strength (molality)	N/A
Porosity	0.10

4.3 Batch Modelling

Batch models are models that exclude transport processes. In these approaches the purpose is to obtain equilibrium between the CO_2-rock-brine interactions and to see what is happening in-between without considering distance into medium. Batch modelling is divided into two main groups, including equilibrium batch modelling and kinetic batch modelling.

4.3.1 Equilibrium Batch Modelling

Equilibrium batch models use the theory of equilibrium to calculate final mole composition of chosen minerals. Equilibrium batch modelling is useful to get a first impression of how the mineralogy changes by looking at the initial concentrations and the equilibrium concentrations. Since geological storage of CO_2 is a very complex setting in which the geochemical reactions happens over a large time span and at different rates the equilibrium batch models are suggested to yield unrealistic results (Gaus et al. 2005). However it should be noted that calcite at relatively high temperatures can be assumed to react fast enough to be properly described by equilibrium batch models (Xu et al. 2005). Equilibrium batch modelling is in the following used to represent secondary minerals and minerals that may struggle to work with the specified rate formulas.

4.3.2 Kinetic Batch Modelling

Kinetic batch models look at the geochemical reactions taking place in the cap rock when CO_2 interacts with the formation water and mineralogy of it. Kinetic modelling utilizes rate equations (Eqs. 15 and 16) to perform kinetic calculations over a manually chosen time length, and divides the total simulation time into time steps where geochemical reactions are calculated at each time step. Input to the rate equations are calculated manually from relevant site specific input parameters.

In PHREEQC the specification of initial moles and the moles that are "allowed" to react per time step are set along with the given rate equations. The initial number of moles are calculated from a simple chemical formula (Eq. 17), whereas the moles allowed to react are for example the initial number of moles divided by the defined number of kinetic time steps, i.e., 10 moles/1000 steps. This quantity is not always necessary, but is useful to avoid convergence problems. It is equal to the initial number of moles if it is not manually specified.

$$n_{moles} = \frac{m_{mineral}}{MW_{mineral}} \qquad \text{(Eq. 17)}$$

where n_{moles} is the number of moles, $m_{mineral}$ is the mass of mineral and $MW_{mineral}$ is the molecular weight of a given mineral.

When equilibrium batch modelling and kinetic batch modelling are run together the concentrations of the former is calculated at each time step set by the latter. Because PHREEQC experiences problems with certain minerals in a complex mineralogical setting, it is useful to define some of these minerals at equilibrium phases instead, although this may cause some alteration of the results.

Reactive surfaces areas are given in cm^2/g in literature and are thus converted to m^2/kgw to fit the rate formulas (Eqs. 15-16). Literature may show conflicting values for *n*, therefore a uniform value of 0.5 is chosen for each mineral. *Log k* for Nordland Shale is given for 37°C (Gaus et al. 2005), whereas it is given for 25°C at Frio Shale (Xu et al. 2005) and must therefore be recalculated for 75°C (Eq. 16). Calcite is run within equilibrium phases at Frio Shale, which does not require rates. Input to the rate equations are given in Appendix B.

4.4 Reactive Transport Modelling

While kinetic batch modelling solely looks at the reactions taking place in the cap rock with time, reactive transport modelling takes time and distance into account. Reactive transport modelling uses 1D grid blocks where reactions in each cell are calculated at the midpoint of the cells (Figure 4.2).

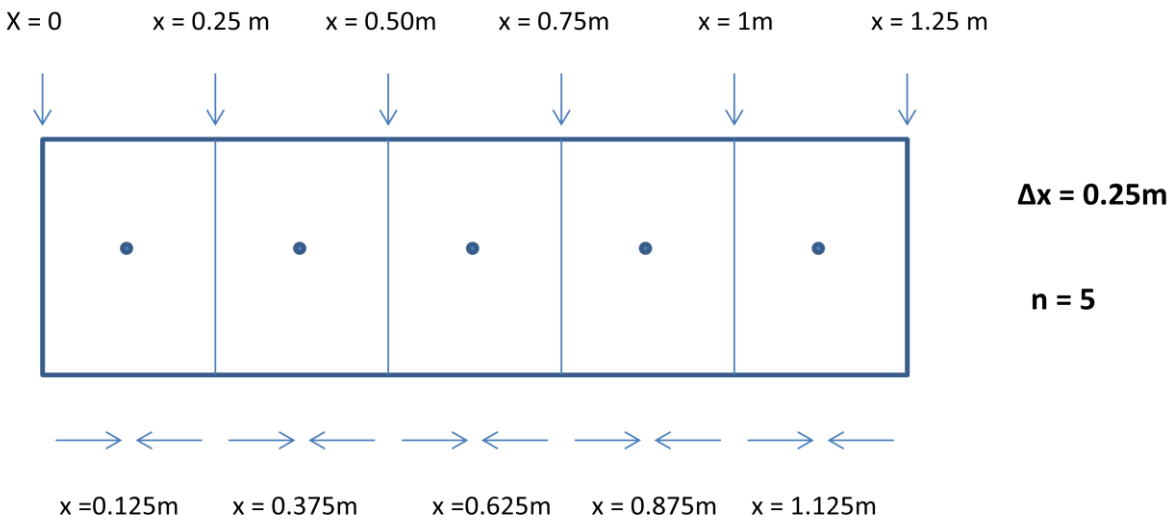

Figure 4.1: A simple grid block schematic of a 1D reactive transport modelling case for 5 cells with cell lengths of 0.25 meter.

Reactive transport modelling is separated into diffusive transport and advection transport. Diffusive transport is the transport of molecules from an area with high concentration to an area of lower concentration, whereas advection transport is transport of molecules due to a flow rate (Parkhurst and Appelo 1999). Advection transport is the fastest transport mechanism of the two. Transport is calculated by setting the number of grid cells, cell length, time step length, number of shifts and boundary conditions. An infilling solution 0 must be defined prior to the simulation. The advection or diffusive transport is then conducted by shifting solution 0 to cell 1, solution in cell 1 to cell 2 and so on (Parkhurst and Appelo 1999). Kinetic reactions are integrated in every cell at each shift, while being in equilibrium with the CO_2 gas phase at all times. The total time of the simulation is the number of shifts multiplied by time step length.

5. Kinetic Batch Modelling Results

5.1 Nordland Shale

Kinetic batch modelling at Nordland Shale were performed for 30 000 years to ensure that equilibrium was obtained for all minerals except muscovite. Since the "initial" concentration given by the output is the concentration in the first step and not year 0, a short-term simulation were also run to see the initial changes. The short-term simulation considered the initial ten years.

As kinetic batch modelling is useful to see if and when equilibrium is achieved for the minerals, some figures have down-scaled time axis to see the reactions occurring between initial contact with CO_2 and equilibrium. The concentrations are given in mol/kgw except for CO_2, which is given in mmol/kgw. The plot of CO_2 concentration versus time and secondary minerals versus time are given on logarithmic plots. Plots of the minerals that are practically non-reactive are given in Appendix C. Figures are not listed for the short-term results.

Albite was chosen to represent the plagioclase mineral, because of time restrictions imposed by anorthite.

5.1.1 Summary of Results

1) Long-Term

Quartz is the most reactive mineral of the precipitating primary minerals, and concentration increases from an initial concentration of 17.68 mol/kgw to a final concentration of 24.14 mol/kgw. This is due to the supply of dissolved $SiO_{2(aq)}$ from simultaneously dissolving silicates. Quartz precipitation is practically finished after just thousand years due to the lack

of supply of $SiO_{2(aq)}$ from albite later in the simulation. Albite dissolves almost completely in this phase of the simulation and supplies quartz and kaolinite with $SiO_{2(aq)}$ and Al^{3+}. K-feldspar dissolution is also significant. Calcite and dawsonite precipitation dominates mineral trapping of CO_2, with only minor contribution coming from dolomite. Magnesite is not visible during the entire simulation. pH increases first rapidly in the initial phase of elevated CO_2 concentrations before it slowly increases to a original pH of 7.67 after ca 10 000 years. Muscovite precipitates slowly due to the supply of K^+, Al^{3+} and $SiO_{2(aq)}$ from the dissolving K-feldspar and albite. The same trend is evident for kaolinite.

2) Short-Term

The same trends for quartz and albite are evident during the first ten years of the simulation. Precipitation of dawsonite is visible after 22 days, whereas dolomite precipitation initiates after 708 days. Calcite initially dissolves due to the immediate drop in pH caused by the CO_2 plume and works to stabilize the pH at 4.5 after approximately 1 000 days. The initial increase of pH is therefore very rapid. The other minerals are practically non-reactive in the initial period.

The overall results for the two simulations are listed in Table 5.1 and Table 5.2.

Table 5.1: pH variations for kinetic batch modelling at Nordland Shale.

	Long-Term		**Short-Term**		Long-Term
	Initial value	Final value	Initial value	Final value	Figure No.
pH	4.49	7.74	3.34	4.50	Figure 5.1

Table 5.2: Results for kinetic batch modelling at Nordland Shale.

	Long-Term		**Short-Term**		Figure No.	
Minerals / CO_2	Initial concentration (mol/kgw)	Final concentration (mol/kgw)	Initial concentration (mol/kgw)	Final concentration (mol/kgw)	Long term	Short term
$CO_{2(g)}$	1.97	0	2.04	1.96	Figure 5.2	N/A
Calcite	0.48	0.67	0.51	0.48	Figure 5.3	N/A
Dawsonite	0.03	1.83	0.00	0.00	Figure 5.4	N/A
Dolomite	0.00	0.02	0.00	0.00	Figure 5.4	N/A
Quartz	17.68	24.14	17.60	17.73	Figure 5.5	N/A
Muscovite	3.30	3.44*	3.31	3.31	Figure 5.6	N/A
Albite	2.28	0.09	2.31	2.27	Figure 5.7	N/A
K-feldspar	0.38	0.25	0.38	0.38	Figure 5.8	N/A
Kaolinite	3.47	3.54	3.47	3.47	Figure C.1	N/A
Pyrite	2.15	2.15	2.15	2.15	Figure C.2	N/A
Smectite	1.07	1.07	1.07	1.07	Figure C.3	N/A
Siderite	0.80	0.81	0.81	0.80	Figure C.4	N/A
Clinochlore-7A	0.34	0.34	0.34	0.34	Figure C.5	N/A
Magnesite**	0.00	0.00	0.00	0.00	N/A	N/A

* Equilibrium is not achieved
** Mineral is not present

5.1.2 Long-term Reactions with Albite Representing Plagioclase

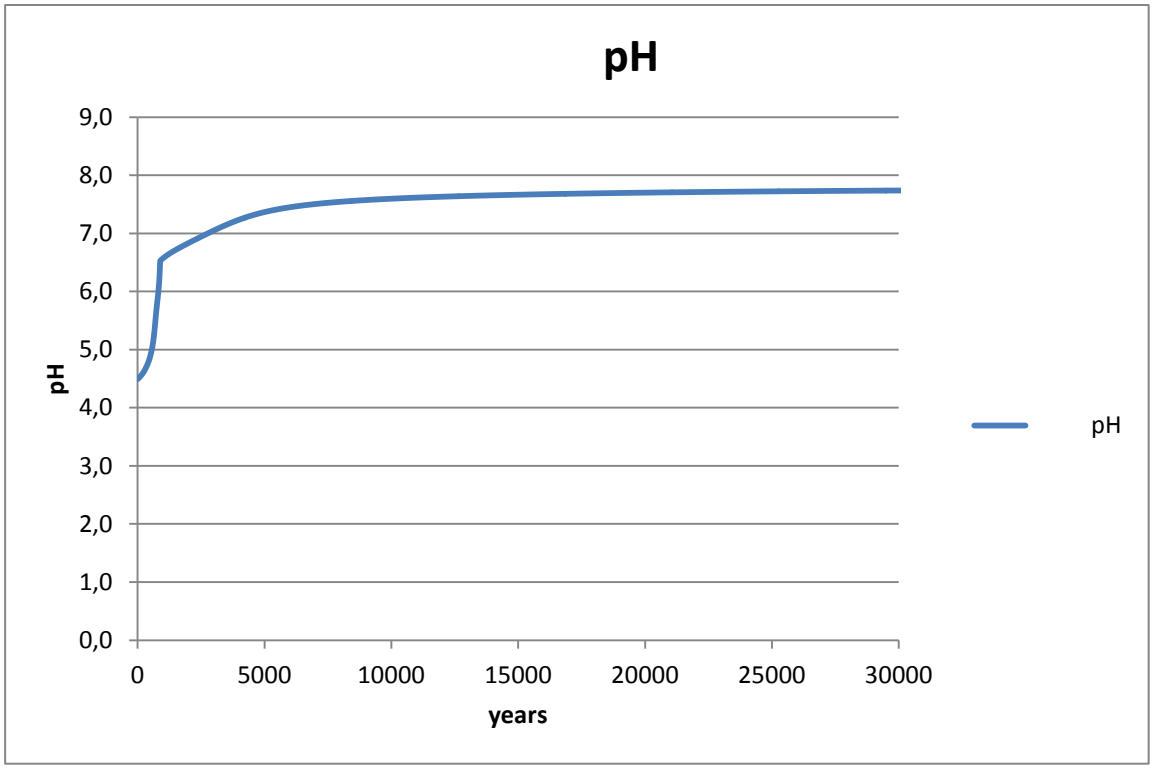

Fig. 5.1: pH variations.

In the long-term simulation the pH is expected to rise steadily as CO_2 dissolves in the formation water. As seen in Figure 5.1 the pH rises from about 4.5 to 6.5 during the first 1 000 years. pH increases slowly at a much slower rate during the next 8 000 years from 6.5 to approximately the initial pH of 7.67. From 15 000 years to 30 000 years the pH rises extremely slowly and is basically at equilibrium at the end with pH of 7.74. This is because there is very little reactivity in the cap rock after so many years.

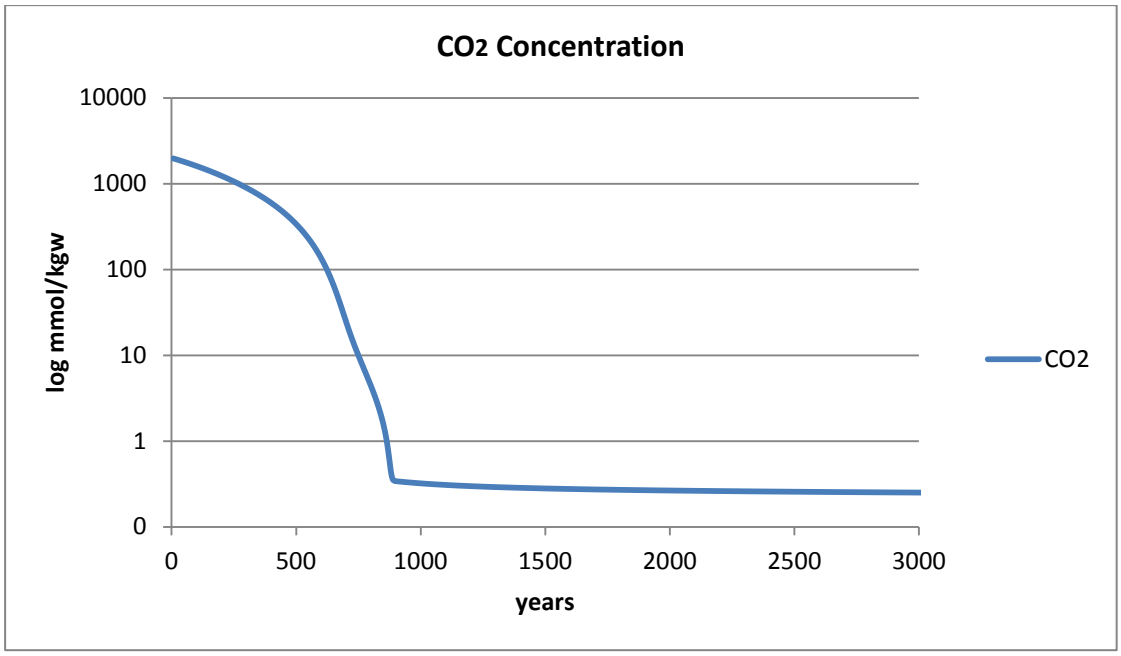

Figure 5.2: CO_2 concentration during the first 3 000 years.

Dissolution of CO_2 happens relatively fast. The concentration is almost at equilibrium after 900 years. Some dissolution is evident from 900 years to 2 000 years as seen in Figure 5.2, while at 3 000 years no measurable CO_2 dissolution occurs. Initial concentration of CO_2 is 1972 mmol/kgw and final concentration is 0.25 mmol/kgw, which is almost nothing.

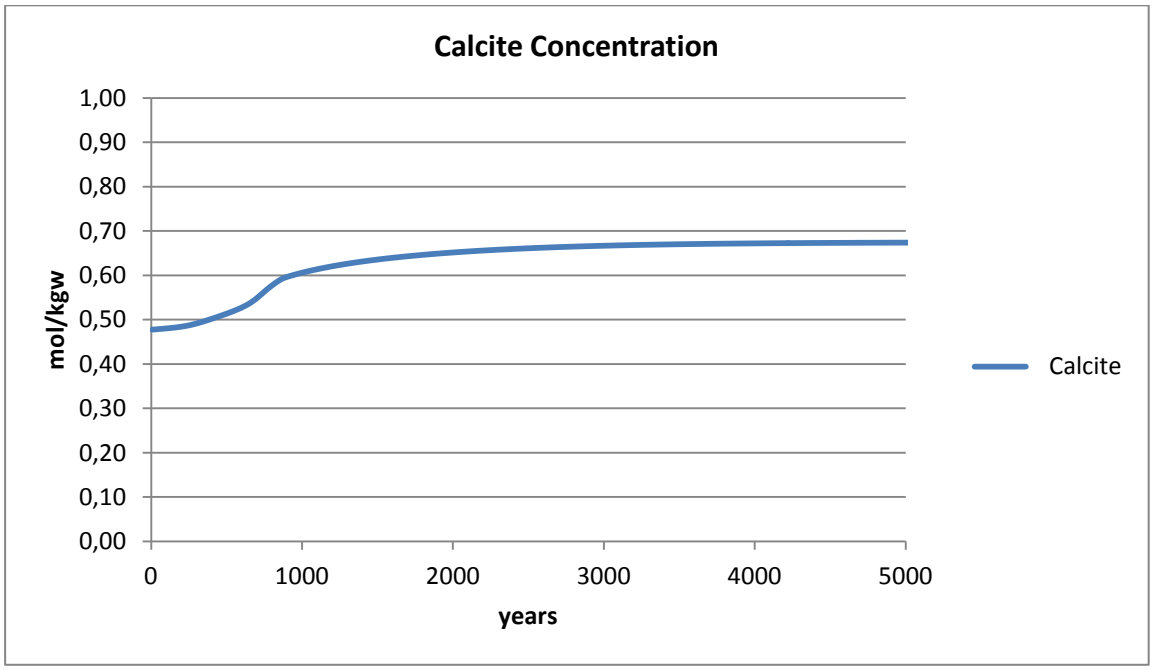

Figure 5.3: Calcite concentration in the first 5 000 years.

Figure 5.3 shows that calcite precipitates rapidly between 200 years and 1 000 years, especially at the end of this phase. Calcite therefore traps a fraction of the CO_2. Ca^{2+} is supplied by the formation water along with the Ca^{2+} that comes from the initial dissolution of calcite. Calcite still precipitates for the next 4 000 years before equilibrium is reached just shy of 5 000 years into the simulation. The final concentration of calcite is 0.67 mol/kgw.

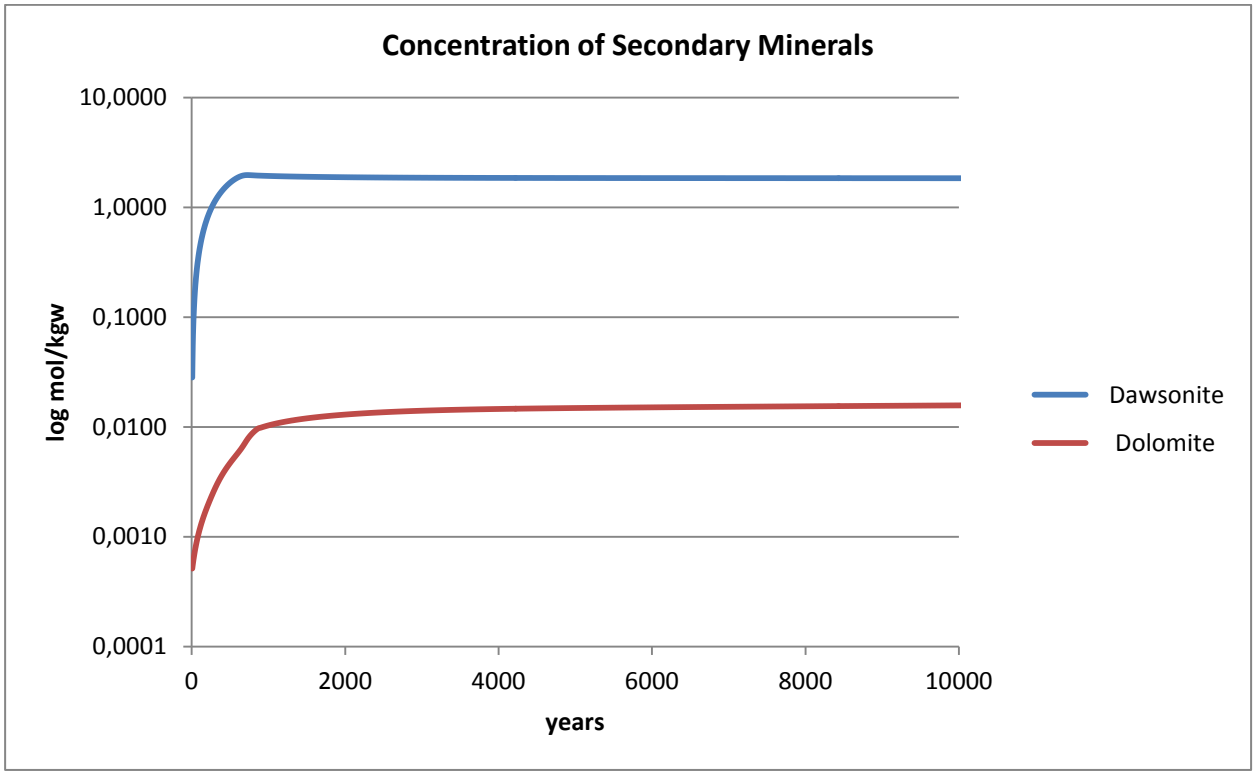

Figure 5.4: Concentration of secondary minerals during the first 10 000 years.

Dawsonite quickly precipitates to trap some of the dissolved CO_2. As seen in Figure 5.4, dawsonite is the main CO_2 trapping mineral (along with calcite) and has reached an equilibrium concentration of 1.83 mol/kgw after approximately 1 000 years. Although barely visible on this logarithmic plot, dawsonite then dissolves from a concentration of 1.96 mol/kgw to equilibrium concentration of 1.83 mol/kgw after 10 000 years, which prevents albite from complete dissolution. Dolomite reaches an equilibrium concentration of 0.016 mol/kgw. Magnesite, which was introduced as a potential secondary mineral, is not seen to precipitate during the simulation and is thus not present at all.

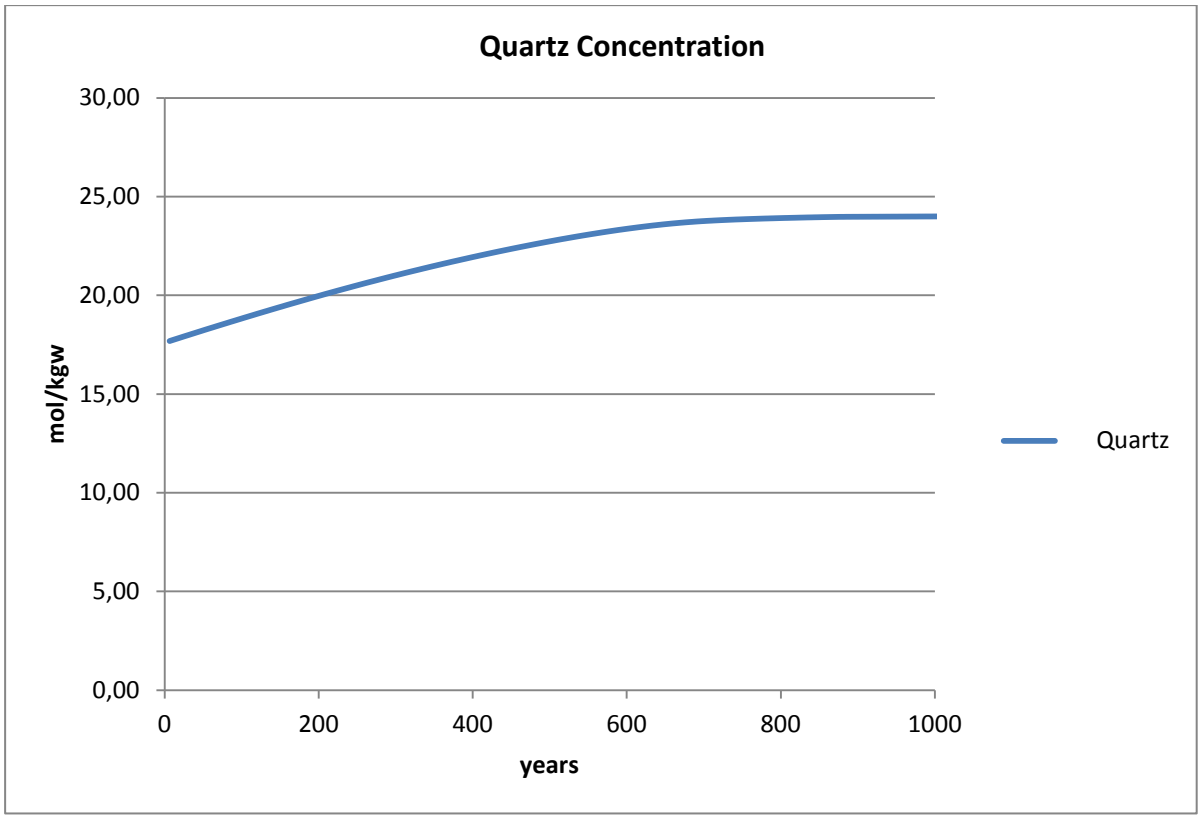

Figure 5.5: Quartz concentration during the first 1 000 years.

Quartz contains the largest molar concentration among the minerals, as indicated by Figure 5.5. Precipitation of quartz happens quickly while CO_2 is at elevated concentration. This is because dissolved $SiO_{2(aq)}$ molecules are product of simultaneous silicate dissolution (Table A.1), and silicate dissolution at Nordland Shale is strongly linked to the presence of CO_2 in the system.

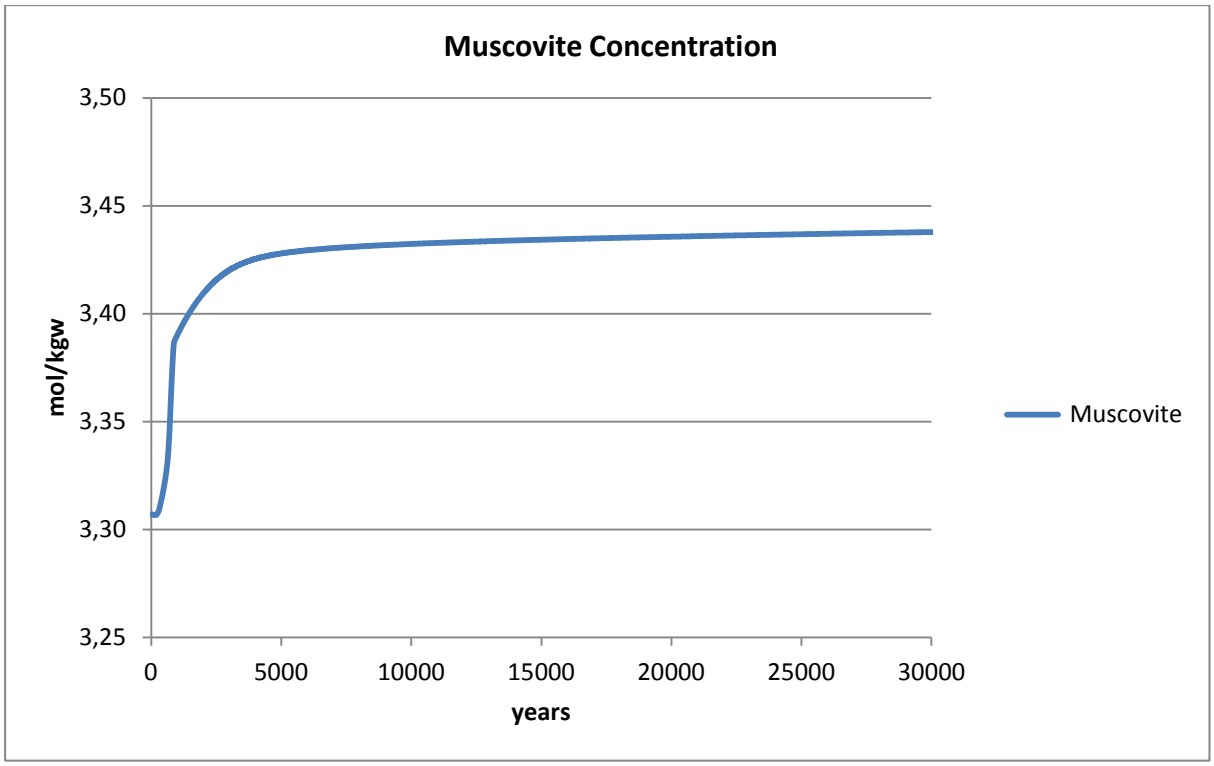

Figure 5.6: Muscovite concentration.

Muscovite precipitates for the entire 30 000 years, as indicated by Figure 5.6. Muscovite is the only mineral that has not achieved equilibrium after 30 000 years, and it is reasonable to believe that it will continue to precipitate slowly but steadily for many years beyond the scope of this simulation. Muscovite dissolves at an elevated rate during the initial 900 years where gaseous CO_2 is present at high concentrations. Muscovite is provided with K^+, Al^{3+} and $SiO_{2(aq)}$ from the dissolving albite (Figure 5.7) and K-feldspar (Figure 5.8). The precipitation continues with a less steep rate from approximately 1 000 years to 4 000 years, before it reaches a plateau for the remainder of the simulation and its final concentration after 30 000 years is 3.44 mol/kgw.

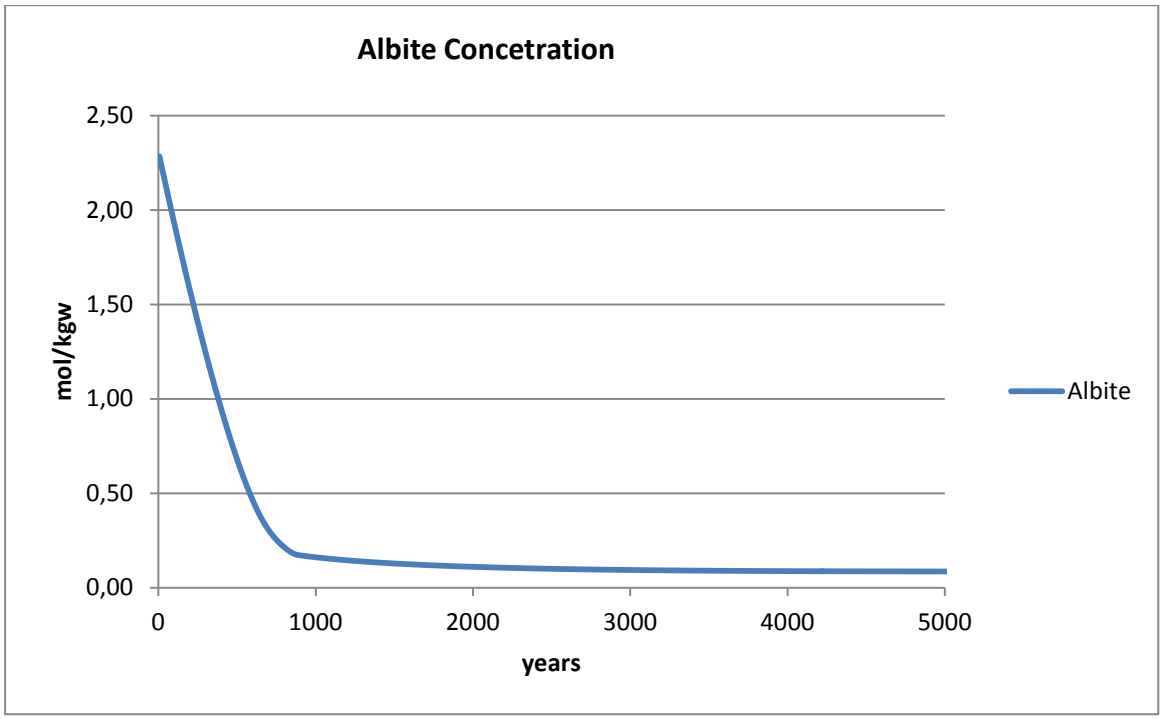

Figure 5.7: Albite concentration during the first 5 000 years.

Albite dissolution happens fast and is a strong function of the presence of CO_2, as seen in Figure 5.7. When all CO_2 is almost completely removed from the gaseous phase after 900 years, albite dissolves at a much slower rate before equilibrium is reached somewhere between 3 000 and 4 000 years at a concentration of 0.09 mol/kgw. The precipitation of calcite, quartz and kaolinite from albite dissolution can be shown by the following reaction (Gaus et al. 2005):

$$2NaAlSi_3O_8 + CO_2 + 2H_2O + Ca^{2+} \rightarrow 4SiO_2 + CaCO_3 + Al_2Si_2O_5(OH)_4 + 2Na^+ \qquad \text{(C-5)}$$

Below is a reaction that shows how dawsonite is formed by dissolution of albite (Gaus et al. 2005):

$$NaAlSi_3O_8 + CO_2 + H_2O \rightarrow 3SiO_2 + NaAlCO_3(OH)_2 \qquad \text{(C-6)}$$

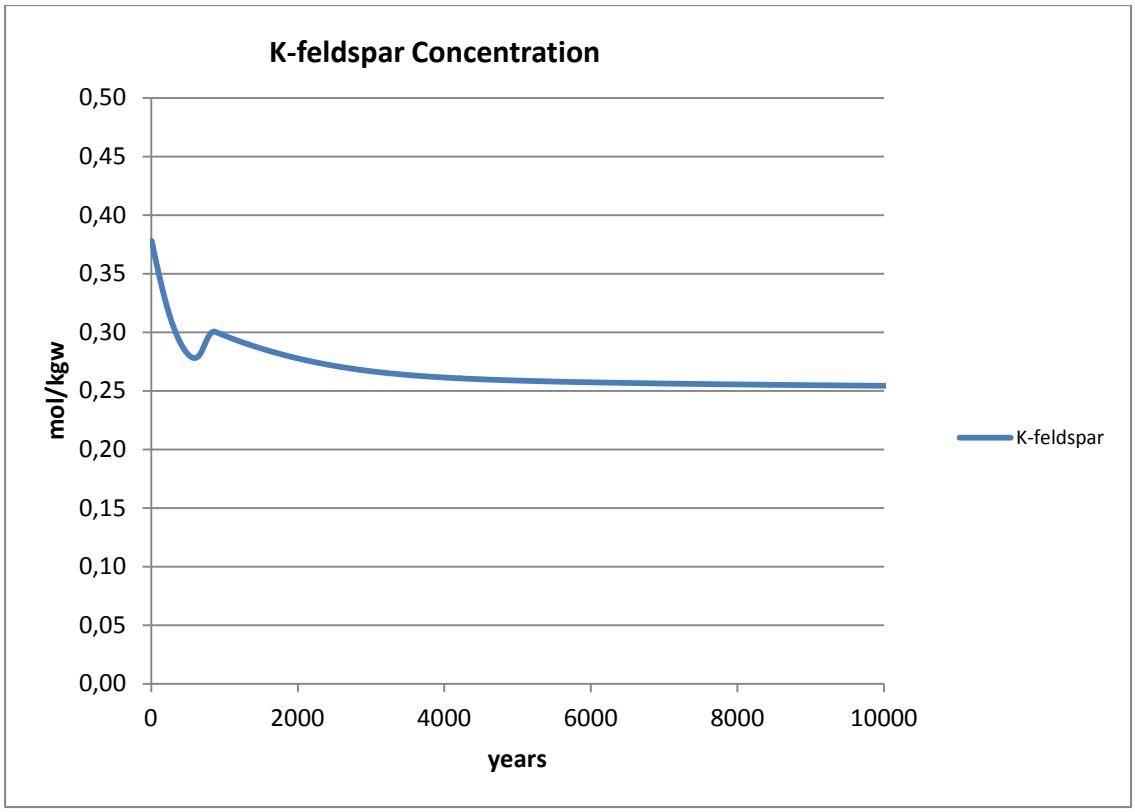

Figure 5.8: K-feldspar concentration during the first 10 000 years.

K-feldspar dissolves for the first 600 years, but in contrast to albite it precipitates for the remaining 300 years in the period where gaseous CO_2 is present at elevated concentration. This is clearly seen in Figure 5.8. K-feldspar subsequently dissolves until it reaches a final concentration of about 0.25 at equilibrium after 10 000 years. The 300 years of precipitation is mainly due to the supply of initially dissolved K^+ ions.

5.2 Frio Shale

A long-term simulation covering 6 350 years were conducted with albite as representative for plagioclase. The long-term simulation is not run for more than 6 350 years because of time restrictions imposed by the input data on PHREEEQC. Simulations with anorthite were not able to run for any longer than 500 years and were therefore not considered. No short-term simulation was conducted in this case.

5.2.1 Summary of Results

Quartz is in contrast to the behaviour seen in the Nordland Shale practically non-reactive in the Frio Shale formation. Kaolinite and K-feldspar are instead the dominating precipitates at Frio Shale. K-feldspar precipitation is also in stark contrast to Nordland Shale where it was dissolving. These minerals get the required Al^{3+}, K^{+} (for K-feldspar) and $SiO_{2(aq)}$ from dissolving Na-montmorillonite, muscovite and albite. Muscovite dissolution is also in contrast to the precipitation seen in the Nordland cap rock. The rapid dissolution of albite is however equal for both cap rocks. Dawsonite is the dominating trapping mineral of CO_2 as was also the case for Nordland Shale. The plots of the non-reactive minerals are shown in Appendix D.

The long-term simulation results from Frio Shale are summarized in Table 5.3 and Table 5.4.

Table 5.3: Initial and final pH for Frio Shale.

	Initial	Final	Figure no.
pH	5.44	5.33*	Figure 5.9

Table 5.4: Summary of the kinetic batch modelling results for Frio Shale.

Long-term changes			Location
Mineral / CO_2	Initial concentration (mol/kgw)	Final Concentration (mol/kgw)	Figure no.
CO_2	2.13	2.11*	Figure 5.10
Muscovite	18.01	15.36*	Figure 5.11
Na-Montor	13.28	12.66*	Figure 5.12
Kaolinite	4.00	6.70*	Figure 5.13
K-feldspar	4.07	6.71*	Figure 5.14
Dawsonite	0.02	1.93*	Figure 5.15
Albite	0.95	0**	Figure 5.16
Quartz	76.31	76.32	Figure D.1
Calcite	26.62	26.62	Figure D.2
Clinochlore-7A	0.94	0.91*	Figure D.3
Siderite	0	0	N/A
Magnesite	0	0	N/A

***** Equilibrium is not achieved

** Mineral has dissolved completely

5.2.2 Long-Term Reactions with Albite Representing Plagioclase

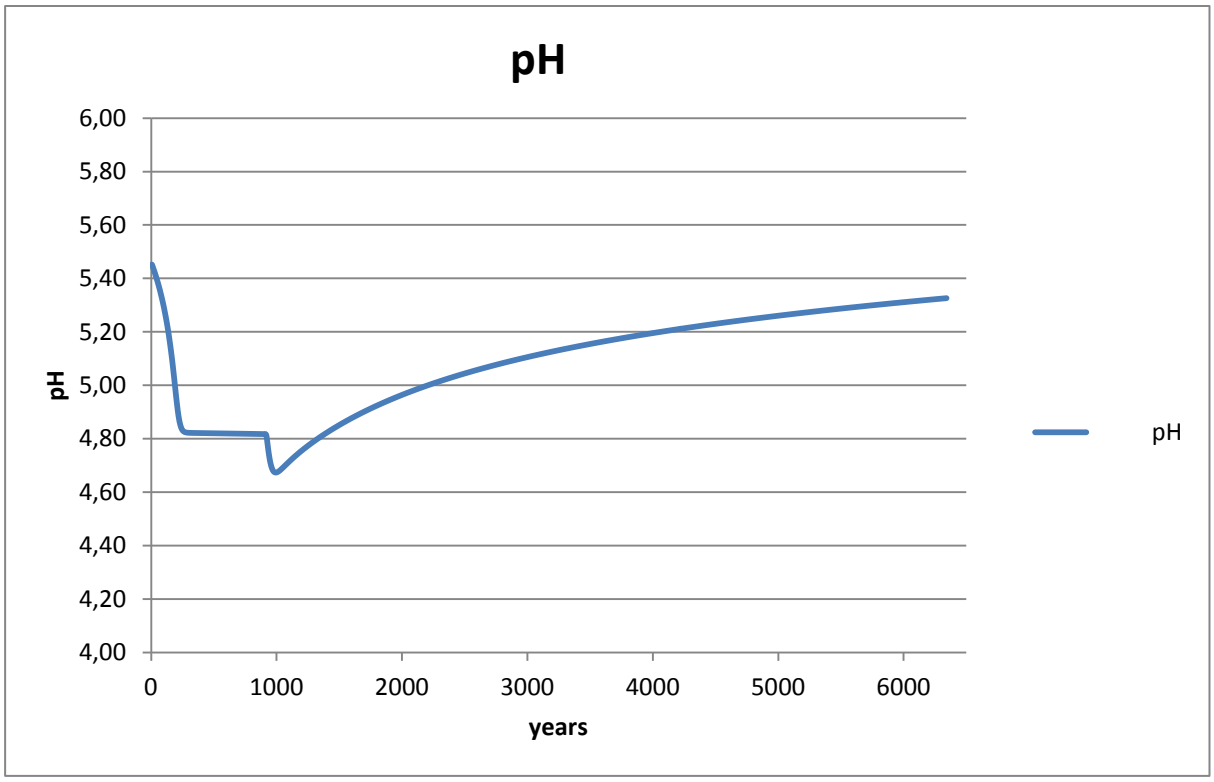

Figure 5.9: pH-variations.

pH is as expected a strong function of the presence of CO_2 and decreases sharply for the first 220 years from approximately 5.45 to 4.82 as shown in Figure 5.9. This is in stark contrast to the increasing behaviour of the Nordland Shale. As CO_2 subsequently dissolve the pH rises steadily to 5.35 after 6 350 years. pH will probably continue to rise for a significant amount of years beyond the simulation scope. The constant pH experienced from ca 220 years to 1 000 years is probably caused by buffering effects.

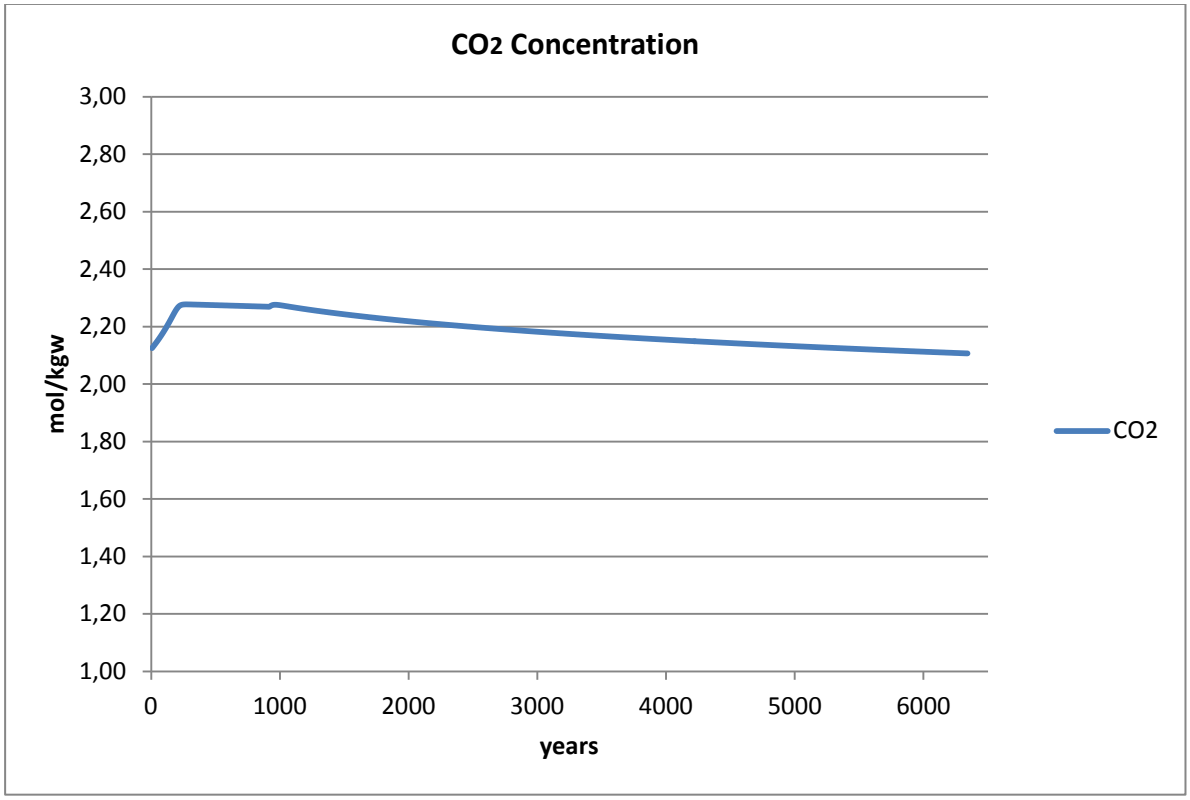

Figure 5.10: CO_2 concentration.

As seen in Figure 5.10 the CO_2 concentration goes from 2.13 mol/kgw to 2.30 mol/kgw during the first 220 years. This is in stark contrast to the concentration slope for Nordland Shale. For the remainder of the simulation the CO_2 concentration decreases slowly but steadily and is not at equilibrium after 6 350 years.

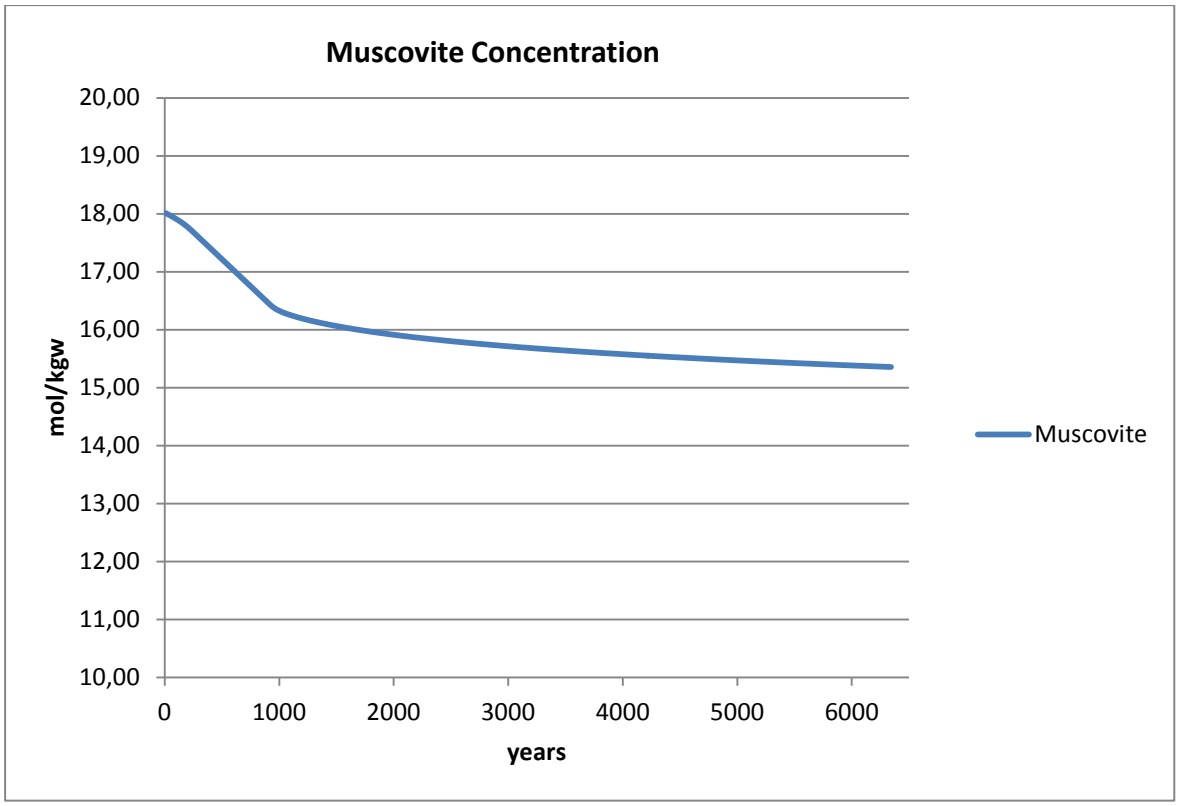

Figure 5.11: Muscovite concentration.

The concentration of muscovite decreases relatively quickly from 18 mol/kgw to about 16.4 mol/kgw during the first 1 000 years, as seen in Figure 5.11. In this period, muscovite dissolves and provides precipitating K-feldspar (Figure 5.14) with K^+ ions along with $SiO_{2(aq)}$ to the precipitating silicate minerals. After 1 000 years the rate of dissolution slows down. Equilibrium is never achieved during the 6 350 years.

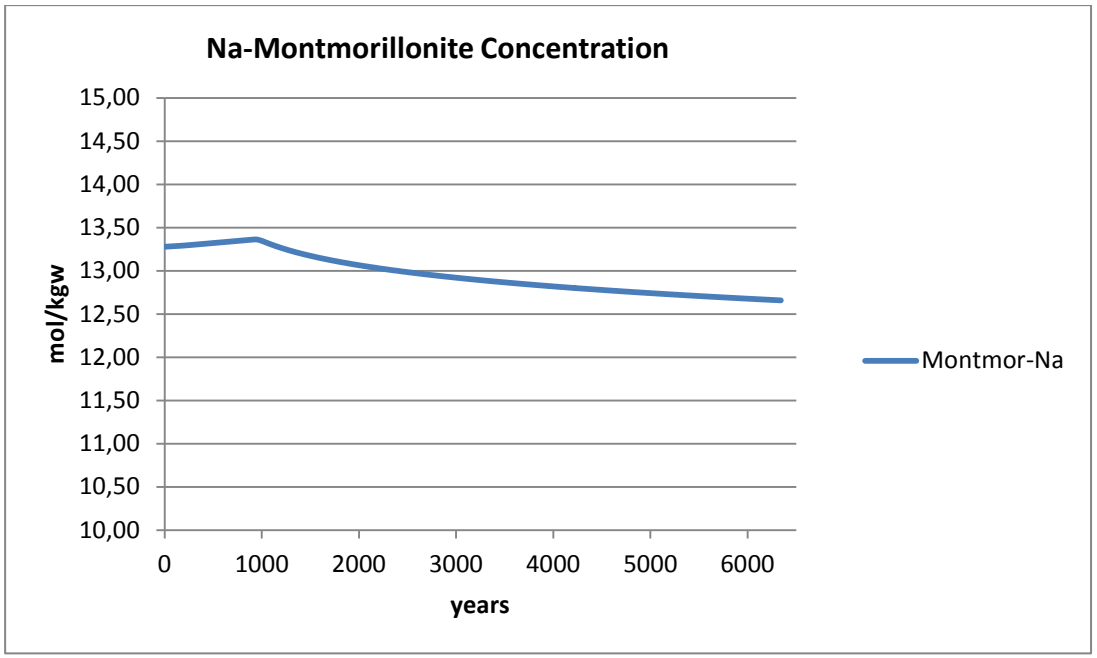

Figure 5.12: Na-montmorillonite concentration.

Figure 5.12 shows that Na-montmorillonite precipitates slowly from 13.3 mol/kgw to 13.4 mol/kgw during initial phase of increased CO_2 concentration, but dissolves for the remainder of the simulation and is still far from equilibrium at the end of the simulations. Its final concentration is 12.7 mol/kgw.

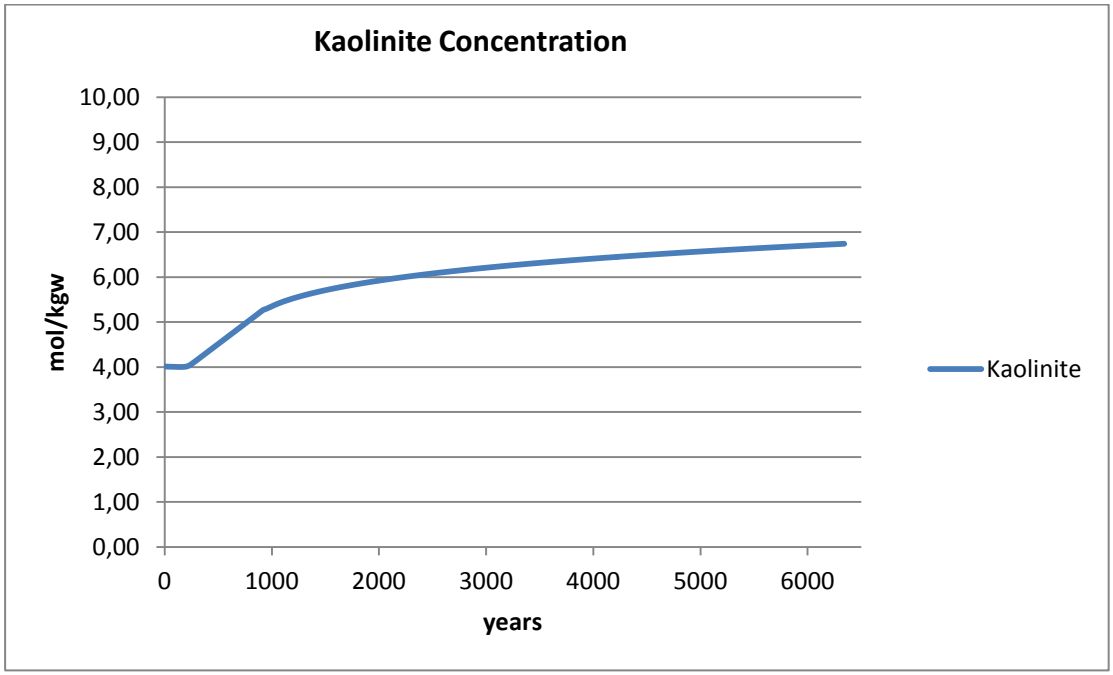

Figure 5.13: Kaolinite concentration.

Figure 5.13 shows that kaolinite concentration is constant during initial concentration increase of CO_2, but increases in concentration when CO_2 starts to dissolve in the brine. This is mostly due to albite dissolution since albite contributes with Al^{3+} and $SiO_{2(aq)}$ to this process (C-5). For the remainder of the simulation the dissolution of Na-montmorillonite and muscovite provides kaolinite with Al^{3+} and $SiO_{2(aq)}$. Kaolinite has a final concentration of 6.7 mol/kgw after 6 350 years, but is still far from equilibrium.

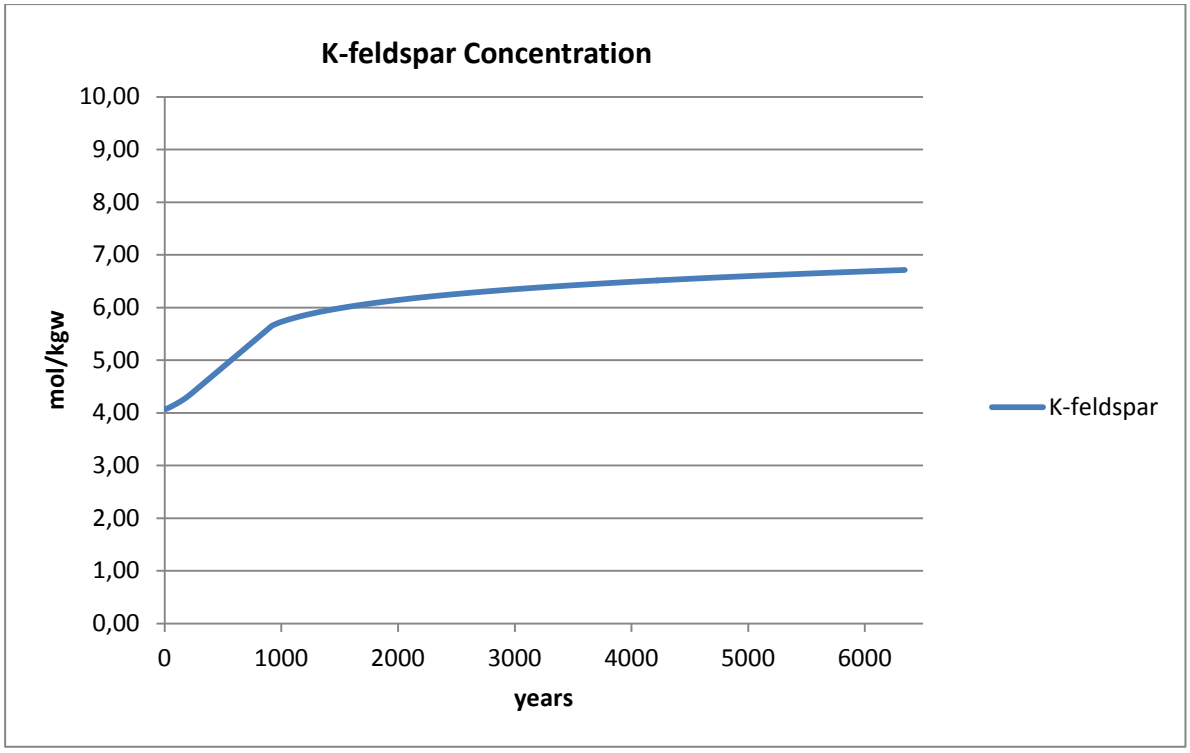

Figure 5.14: K-feldspar concentration.

The slope of K-feldspar concentration is similar to that of kaolinite, as indicated by Figure 5.14. K-feldspar precipitation requires supply of K^+, Al^{3+} and $SiO_{2(aq)}$ (Table A.1). Muscovite is the only dissolving mineral containing K^+ that contributes to the precipitation of K-feldspar. The other ions are supplied from muscovite, albite and Na-montmorillonite. K-feldspar has a final concentration of approximately 6.7 mol/kgw, but is still far from equilibrium.

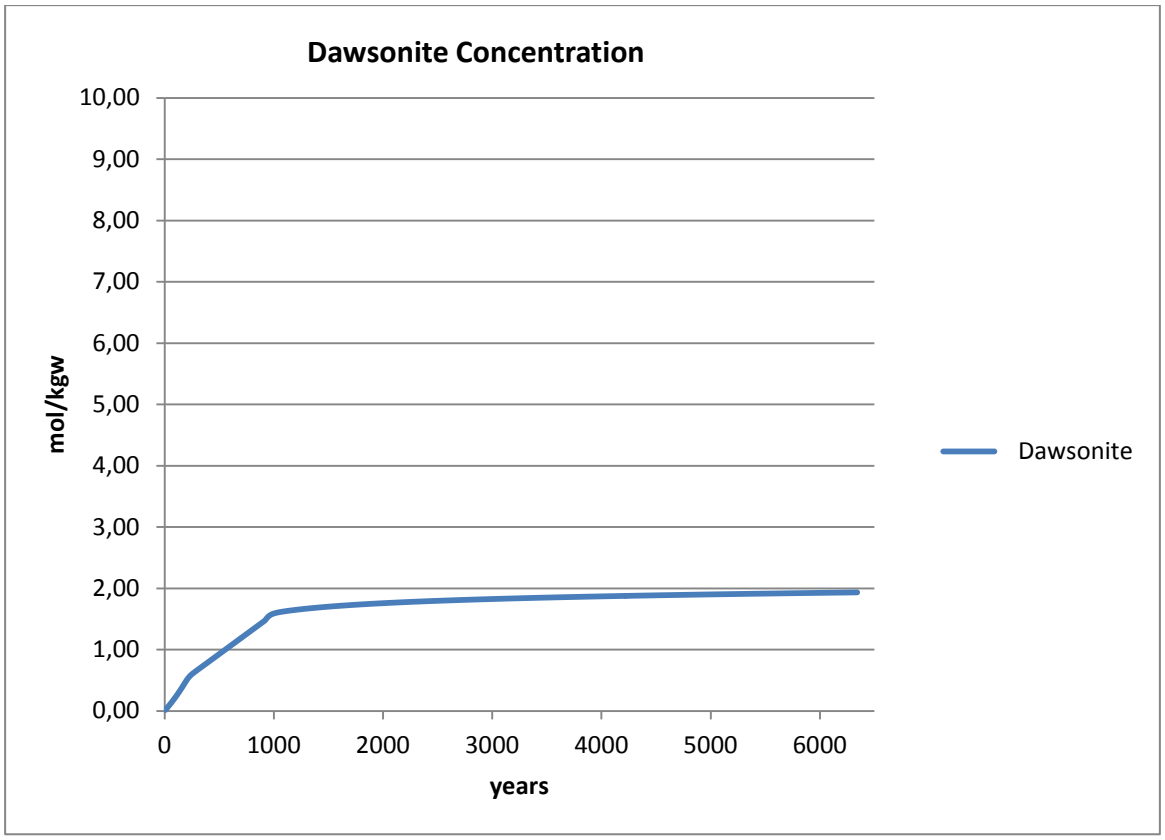

Figure 5.15: Dawsonite concentration (secondary mineral).

Dawsonite forms early, as indicated by Figure 5.15. It precipitates steadily for about 1 000 years at a relatively constant rate, where Na^+ is constantly supplied from dissolving albite (Figure 5.16). Dawsonite then precipitates at a much slower rate for the remainder of the simulation when all albite is removed from the cap rock. After 1 000 years the contribution of Na^+ is minor and comes from the dissolving Na-montmorillonite and formation water. Dawsonite is most likely near equilibrium after 6 350 years and its final concentration is 1.93 mol/kgw.

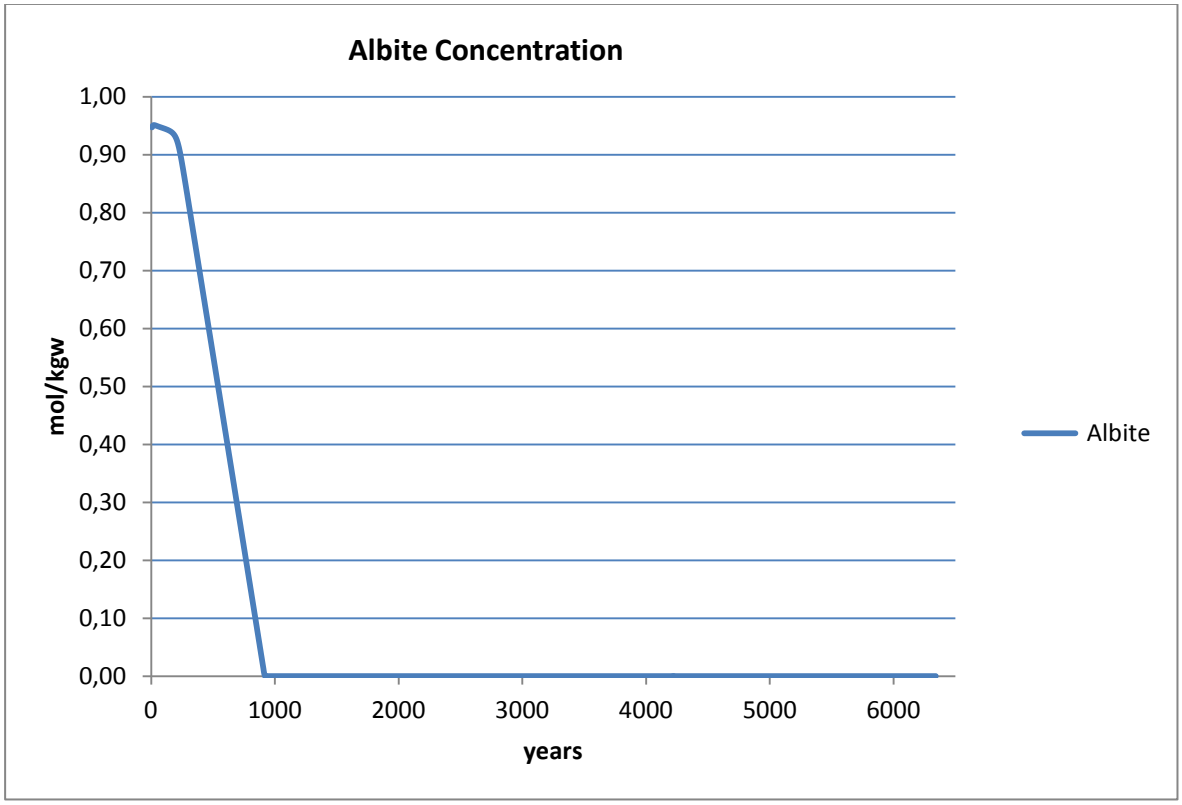

Figure 5.16: Albite concentration.

Albite dissolves very slowly for approximately 100 years, before the rate of dissolution increases rapidly. This is evident from Figure 5.16. Albite is not present in the formation after approximately 900 years. This trend is consistent with what is seen in the Nordland cap rock.

6. Reactive Transport Modelling Results

6.1 Sensitivity on Grid Setup

Specification of the number and sized of grid cells is extremely important. If the grid is too coarse (few grid cells) it may cause numerical dispersion. Numerical dispersion is a feature in finite difference schemes that affects the outlook of the results. A grid of ten cells (n = 10) and individual cell sizes of one meter (Δx = 1.0 m) will not yield equal results compared to a grid of 100 cells and individual cell size of 10 centimetres. This is because the coarser grid may "not see" all the concentration trends as the finer grid with much more data. Three different runs were considered to check for numerical dispersion in the diffusive transport setup:

1) n = 100, Δx = 0.50 cm
2) n = 200, Δx = 0.25 cm
3) n = 500, Δx = 0.10 cm

It was decided that a grid of 100 cells and 50 centimetre cell sizes would be too coarse. Since the cell concentration is measured in the middle of the cell, this meant that 0.25 meters of the cell would ultimately not be "seen". A grid of 500 cells and 0.1 meter cell lengths would be the optimal choice; however the amount of data and real time duration of the simulations meant that this was also discarded. A grid of 200 cells with 0.25 meter cell lengths was therefore chosen, with numerical dispersion at a minimum and amount of data is maintainable (Table 6.1).

Table 6.1: Grid setup for Nordland Shale and Frio Shale for reactive transport modelling

Site	Run	Σcells	Δx (m)	D_d (m^2/s)	Porosity	Lower boundary	Upper boundary	Duration (years)
Nordland	1	200	0.25	4.5×10^{-11}	0.05	Flux	Closed	200
Nordland	2	200	0.25	4.5×10^{-10}	0.05	Flux	Closed	200
Frio	1	200	0.25	1.0×10^{-9}	0.10	Flux	Closed	200
Frio	2	200	0.25	1.0×10^{-8}	0.10	Flux	Closed	200

Sensitivity was also taken on the boundary conditions. It was decided that a flux boundary at the inlet best fitted the problem setup along with a closed upper boundary, which means that no elements are allowed to pass through the outlet boundary.

6.2 Nordland Shale Diffusive Transport

Diffusive transport is conducted for 200 years. Similar to kinetic batch modelling, plagioclase is represented by albite for consistency. In addition the simulations are performed with two different diffusion coefficients, with the slowest one being the one found in literature (Gaus et al. 2005) and the fastest one being ten times larger to check the effects that a faster diffusion rate would potentially have on the transporting section of the cap rock.

The diffusive transport is set up such that the initial concentration in cell 1 is equal to the concentration after 200 years of kinetics with CO_2 present in the cap rock. Differences arise because the first cell measures concentration after 0.125 meters and not at the exact interface. The term initial concentration will in the following be used with the assumption that this concentration equals the concentration at the inlet of the first cell. The concentrations in the cells not affected by diffusive transport are equal to the concentration after 200 years of kinetic simulations given no presence of CO_2 at all during the simulation. In lack of a better word, this is in the following referred to as equilibrium concentration although it only describes "equilibrium" after 200 years without CO_2 affecting the system.

Nordland Shale is run with two effective diffusion coefficients of $D_d = 4.5 \times 10^{-11}$ m^2/s (run 1) and $D_d = 4.5 \times 10^{-10}$ m^2/s (run 2). Diffusive transport simulation is set up with 200 cells. Cell lengths are 0.25 meters, giving a cap rock of 50 meters in total. The porosity of Nordland Shale is 0.05 (Gaus et al. 2005). It is important to notice that the moles allowed to react for each mineral are reduced (downscaled) to allow the simulations to run without experiencing convergence problems. Concentrations are therefore given in mmol/kgw.

6.2.1 Summary of Results

Diffusive transport affects the first four to five meters of the cap rock in the original run for most of the minerals. Large concentration changes are observed in this section of the cap rock. Quartz concentration is relatively stable compared with the other minerals, with a 19 % change in composition. The rest of the minerals present in the cap rock changes more than 50 % of their original composition, except for pyrite. With a ten times faster effective diffusion coefficient there is observable change in the mineralogy within the first ten to twelve meters of the cap rock. The concentration trends are almost equal to the original diffusion coefficient, but the concentration changes are smaller since diffusion happens over a larger distance

Summary of the results are listed in Table 6.1 and Table 6.2

Table 6.2: pH variations during diffusive transport for Nordland Shale.

	Run 1		**Run 2**		
	Initial	Final	Initial	Final	Figure No.
pH	4.04	7.51	4.43	7.51	Figure 6.1

Table 6.3: Diffusive transport results for Nordland Shale.

Run 1			**Run 2**		
Mineral/ CO_2	Initial concentration (mmol/kgw)	Final concentration (mmol/kgw)	Initial concentration (mmol/kgw)	Final concentration (mmol/kgw)	Figure no.
$CO_{2(g)}$	455.8	0.0	142.7	0.0	Figure 6.2
Quartz	15.1	12.2	14.4	12.2	Figure 6.3
Kaolinite	4.3	2.1	3.7	2.1	Figure 6.4
Muscovite	0.6	2.2	1.0	2.2	Figure 6.5
Pyrite	1.0	1.2	1.1	1.2	Figure 6.6
Smectite (...)	0.3	0.9	0.4	0.9	Figure 6.7
Dolomite	0.0	0.4	0.0	0.4	Figure 6.8
Clinochlore-7A	0.0	0.2	0.0	0.2	Figure 6.9

Other minerals were not present after 200 years of diffusive transport in the cap rock.

6.2.2 Diffusive Transport with Albite Representing Plagioclase

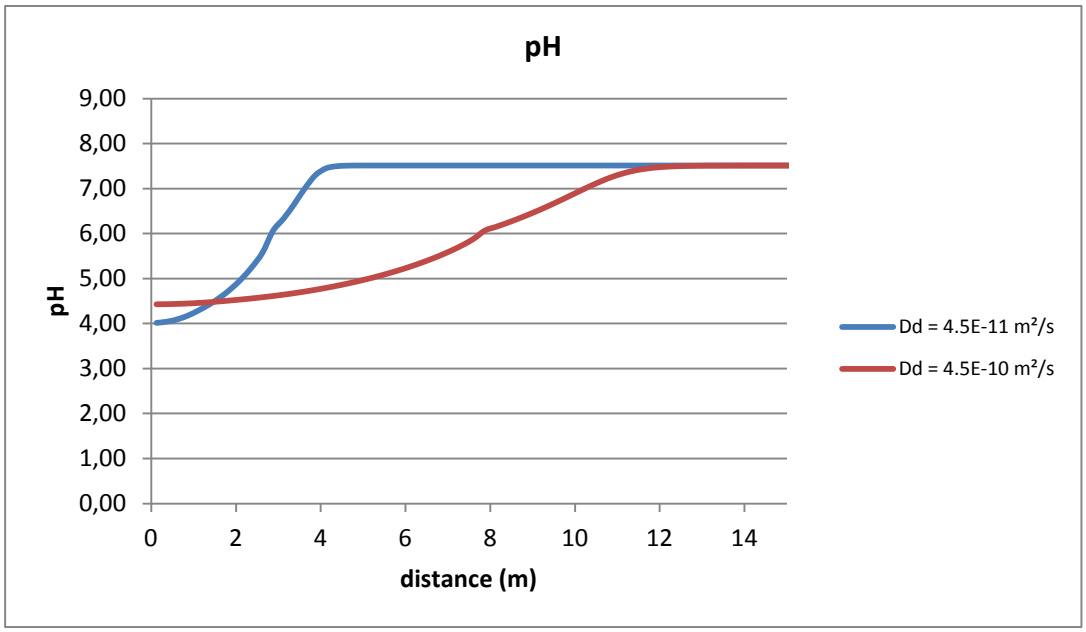

Figure 6.1: pH variations within the first 15 meters of the cap rock.

pH rises from initial pH of 4.04 to 7.51 at equilibrium. Since the CO_2 concentration decreases rapidly in the first four meters the pH will rise proportionally. No change in pH is seen after five meters of the cap rock for run 1, as indicated by Figure 6.1.

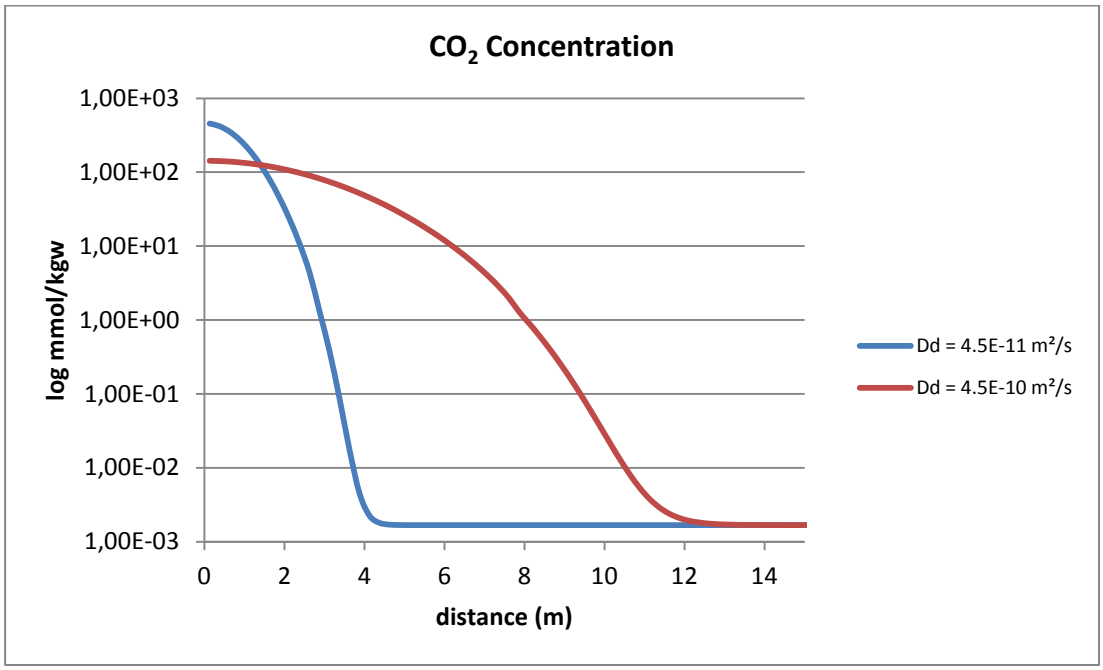

Figure 6.2: CO_2 concentration within the first 15 meters of the cap rock.

Figure 6.2 shows that elevated concentration of CO_2 only exists within the first four meters of the cap rock after 200 years with the original diffusion coefficient. It is evident that the CO_2 effects seen in the first five meters of the cap rock are significant. The trend is similar for the second run with a faster diffusion coefficient, where diffusive transport affects the lower 13 meters of the shale.

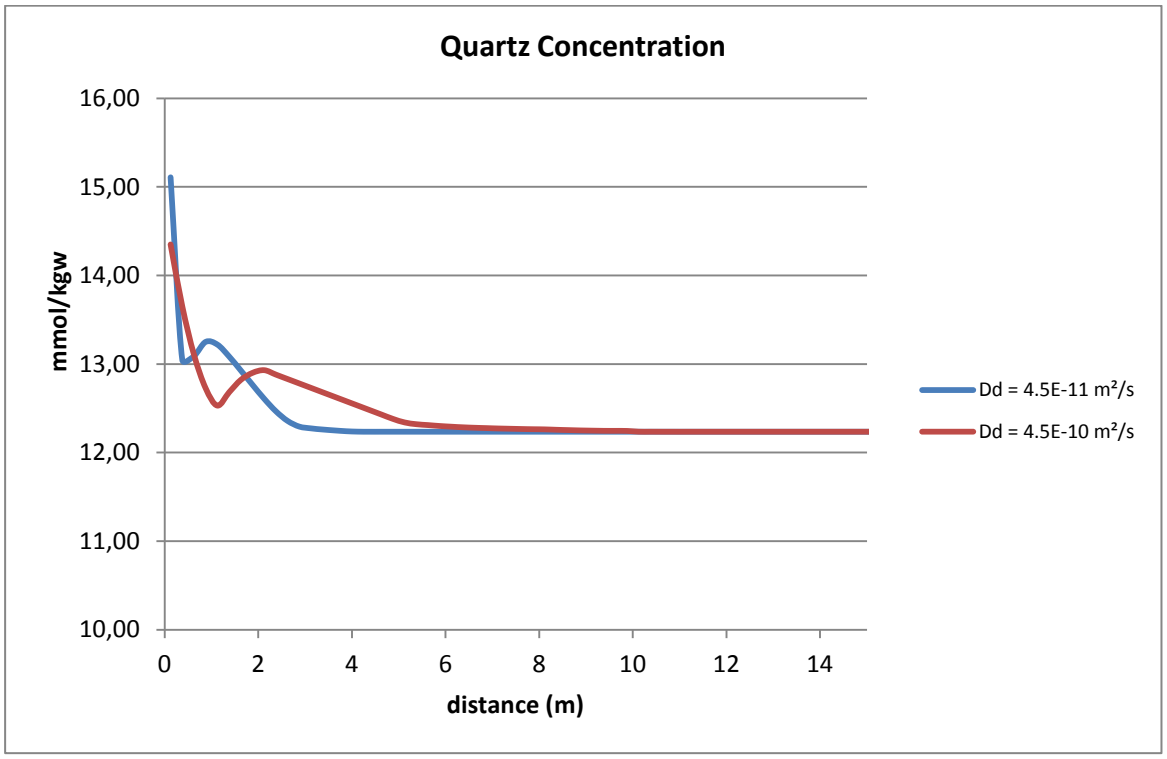

Figure 6.3: Quartz concentration within the first 15 meters of the cap rock.

Figure 6.3 shows those quartz first decreases rapidly within the first meter of the shale. This is because CO_2 concentration decreases, thereby implying that other silicate minerals are precipitating in the same section. This feature is seen for kaolinite (Figure 6.4), which precipitates as quartz dissolves and thus "steals" the dissolved $SiO_{2(aq)}$. For the next half meter or so, quartz precipitates shortly before it again dissolves steadily until approximately three meters into the cap rock. Some slight dissolution is seen within the next meter, but equilibrium is nevertheless achieved after approximately four meters. The second run is very similar, and obtains equilibrium after ten meters.

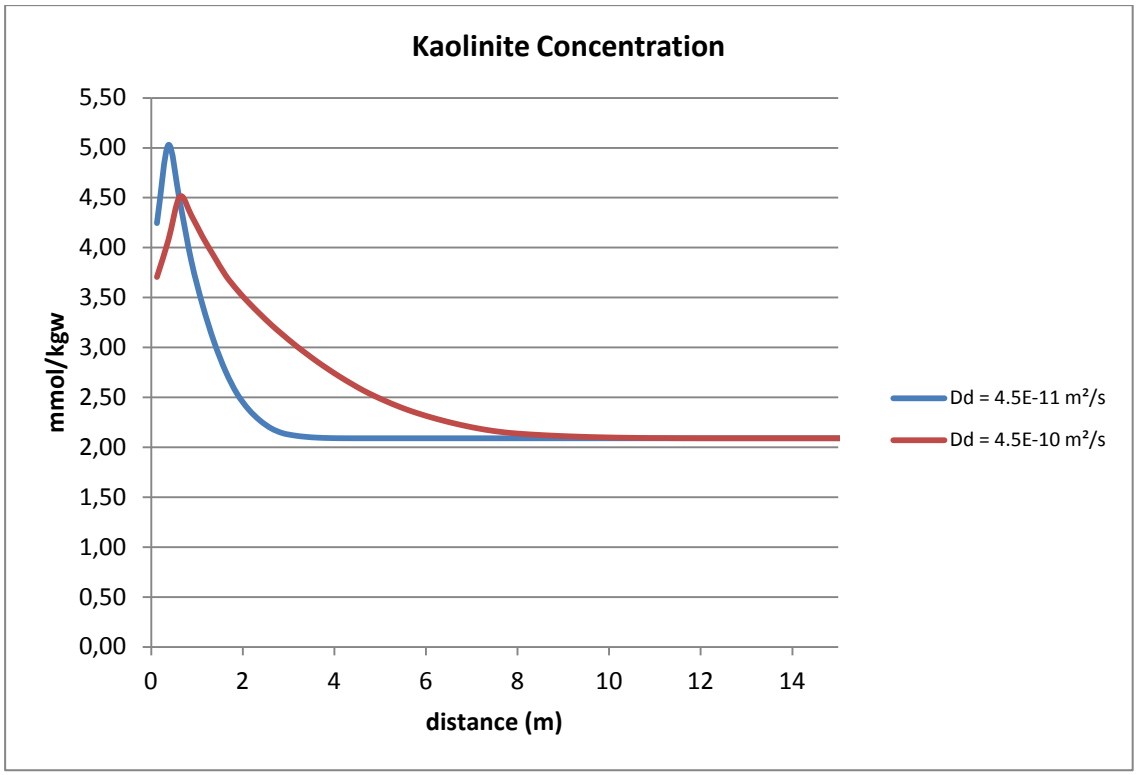

Figure 6.4: Concentration of kaolinite within the first 15 meters of the cap rock..

Figure 6.4 shows that kaolinite concentration increases within the first meter of the cap rock. This is possibly due to the fact that this area contains the highest CO_2 concentrations encountered within the cap rock. Dissolution of other silicates promotes precipitation of kaolinite. The amount of kaolinite present in the cap rock is stabilized after four meters, with a concentration of 2.1 mmol/kgw. The same trend is evident for run 2, where kaolinite reaches equilibrium concentration at eleven meters into the cap rock.

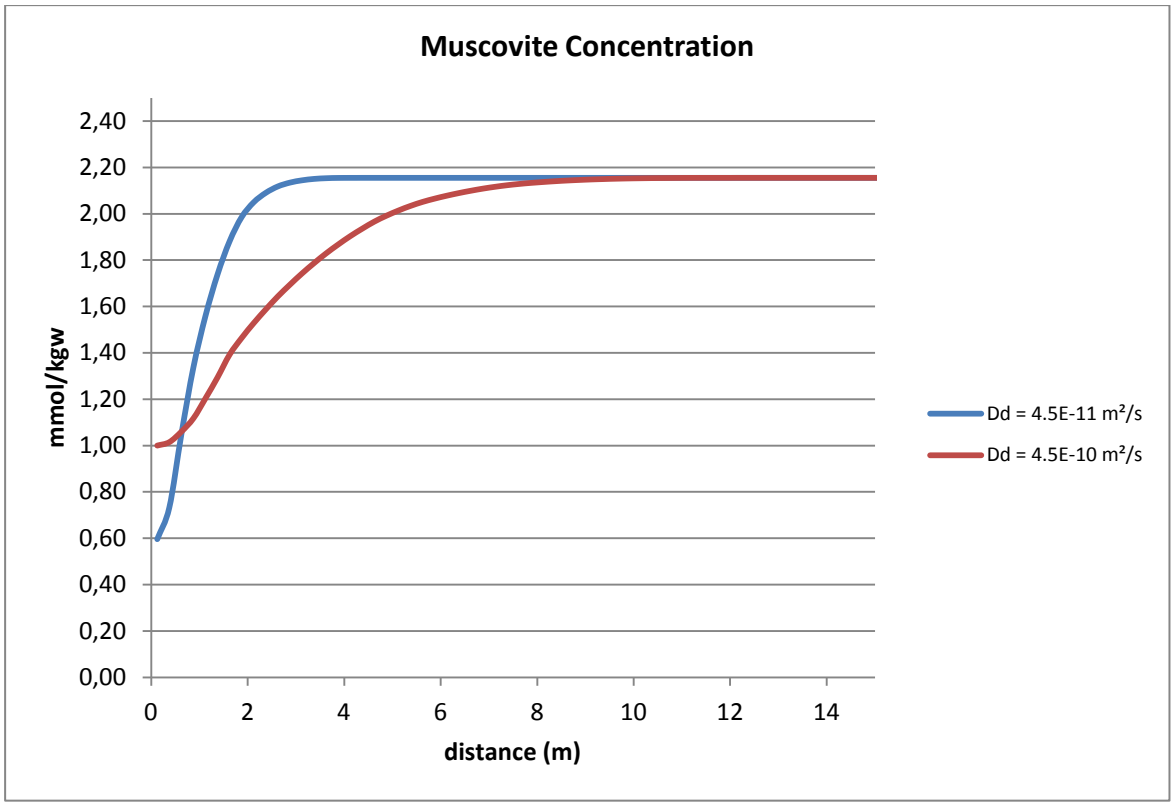

Figure 6.5: Muscovite concentration within the first 15 meters of the cap rock.

Muscovite concentration rises within the first four meters of the cap rock. Muscovite tends to dissolve where CO_2 concentration is high, so the muscovite concentration therefore rises as CO_2 vanishes from the cap rock. Equilibrium concentration is 2.15 mmol/kgw, as indicated by Figure 6.5. The trend is similar for run 2. Muscovite precipitates within the first eleven meters from an initial concentration of 1.00 mmol/kgw.

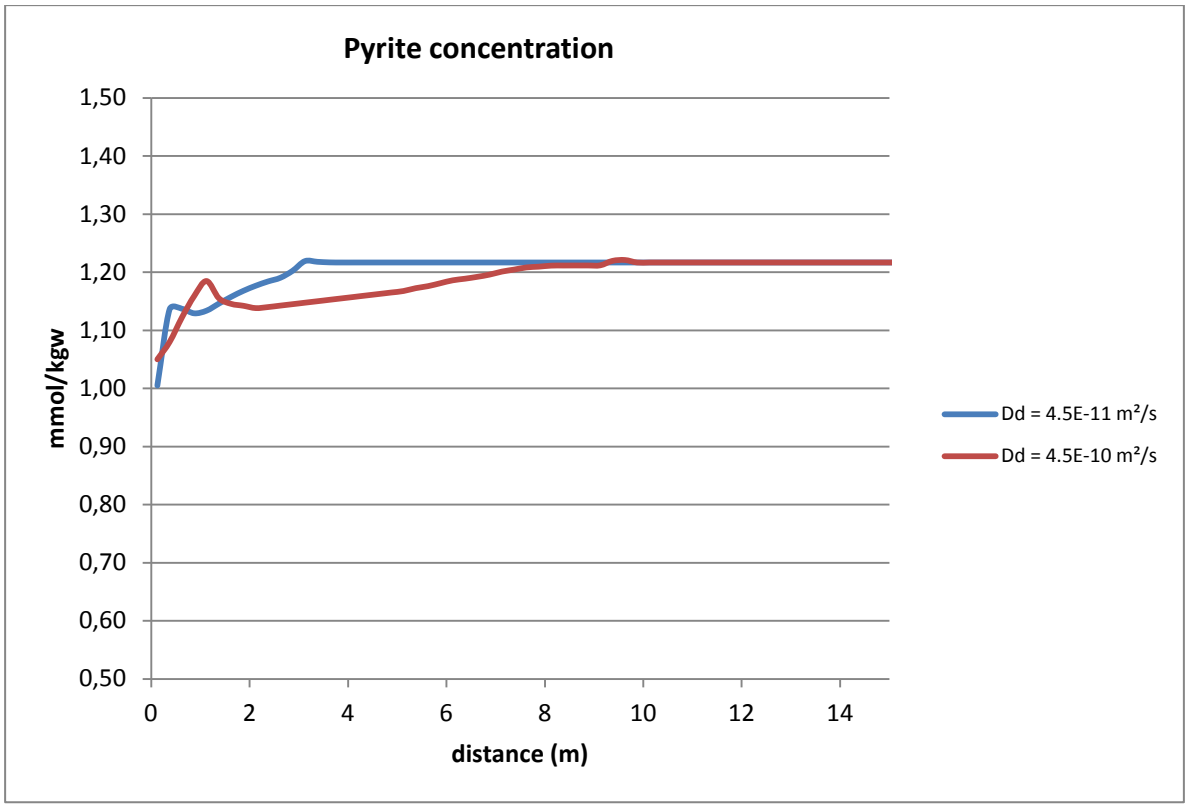

Figure 6.6: Pyrite concentration within the first 15 meters of the cap rock.

Pyrite precipitates initially from a concentration of 1 mmol/kgw to a concentration of 1.2 mmol/kgw in run 1, as shown by Figure 6.6. In this period, pyrite is supplied with Fe^{2+} and S^{-} from the formation water. A very short decrease in concentration is evident, before concentration increases slowly until equilibrium is reached after approximately four meters. The same trend is evident for run 2, with an initial concentration of 1.04 mmol/kgw. However, some distortions are seen. These may be insignificant or due to convergence problems for the iron element. Diffusive transport nevertheless affects the first ten meters of the cap rock in the second run.

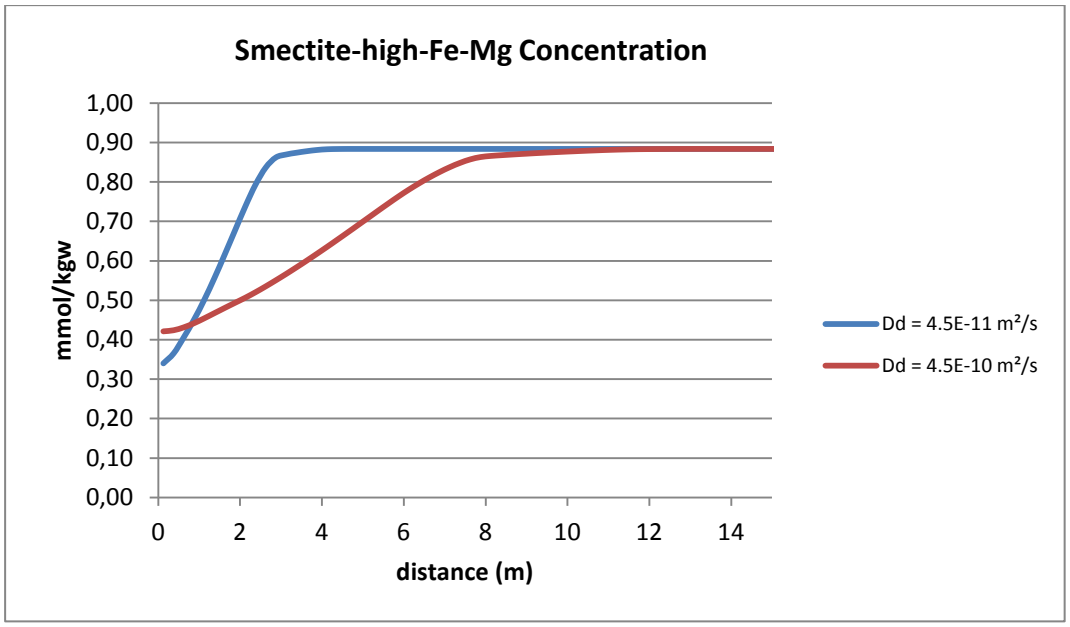

Figure 6.7: Smectite-high-Fe-Mg concentration within the first 15 meters of the cap rock.

Smectite-high-Fe-Mg precipitates at elevated CO_2 concentrations. Figure 6.7 shows that the concentration of the clay mineral increases until equilibrium is reached at four meters where no elevated CO_2 is longer present. Concentration near the lower-boundary is 0.33 mmol/kgw and equilibrium concentration is 0.88 mmol/kgw. In run 2, smectite increases gradually from initial 0.41 mmol/kgw to 0.88 mmol/kgw after twelve meters.

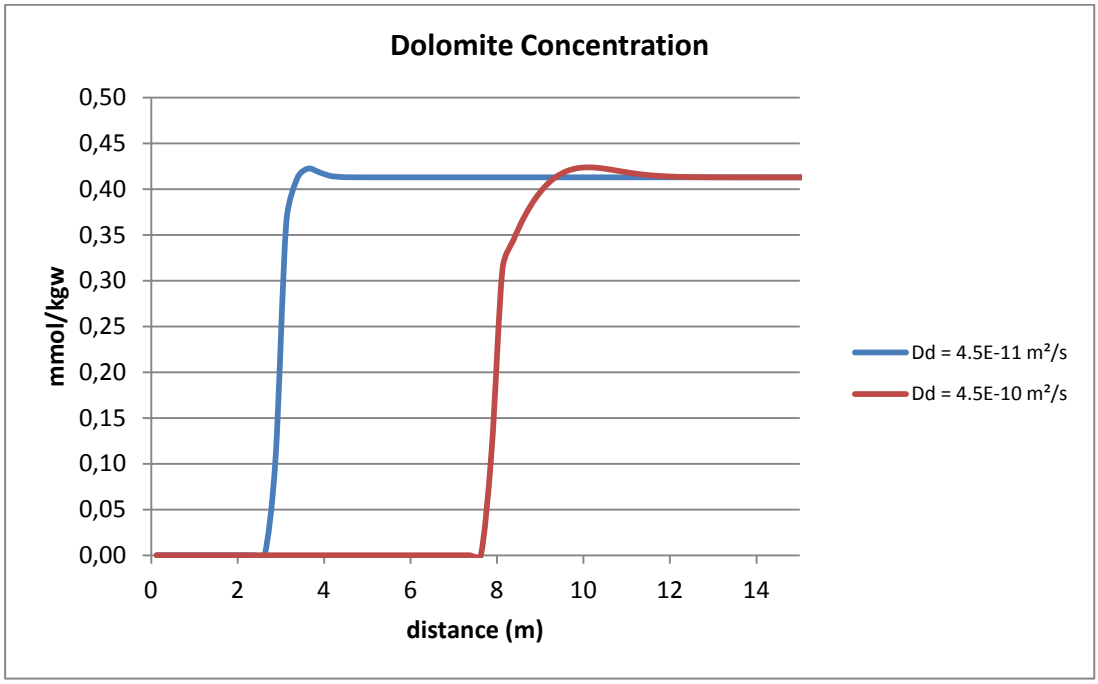

Figure 6.8: Dolomite concentration (secondary mineral) within the first 15 meters of the cap rock.

Figure 6.8 shows that dolomite is not present in the first three meters, but precipitates in the next meter to trap a fraction of the dissolved CO_2. Final dolomite concentration is 0.41 mmol/kgw. A short decrease of dolomite can be seen just before equilibrium is reached. No dolomite is present until 8 meters into the cap rock in the second run. A less steep curve is evident, and a break of the curve is also seen from concentration of 0.32 mmol/kgw to peak level of 0.42 mmol/kgw, which is not evident in the first run. This is possibly due to the chosen cell length of 0.25 meter doesn't show the true slope for run 1, or because the true slope break in the first run is extremely small.

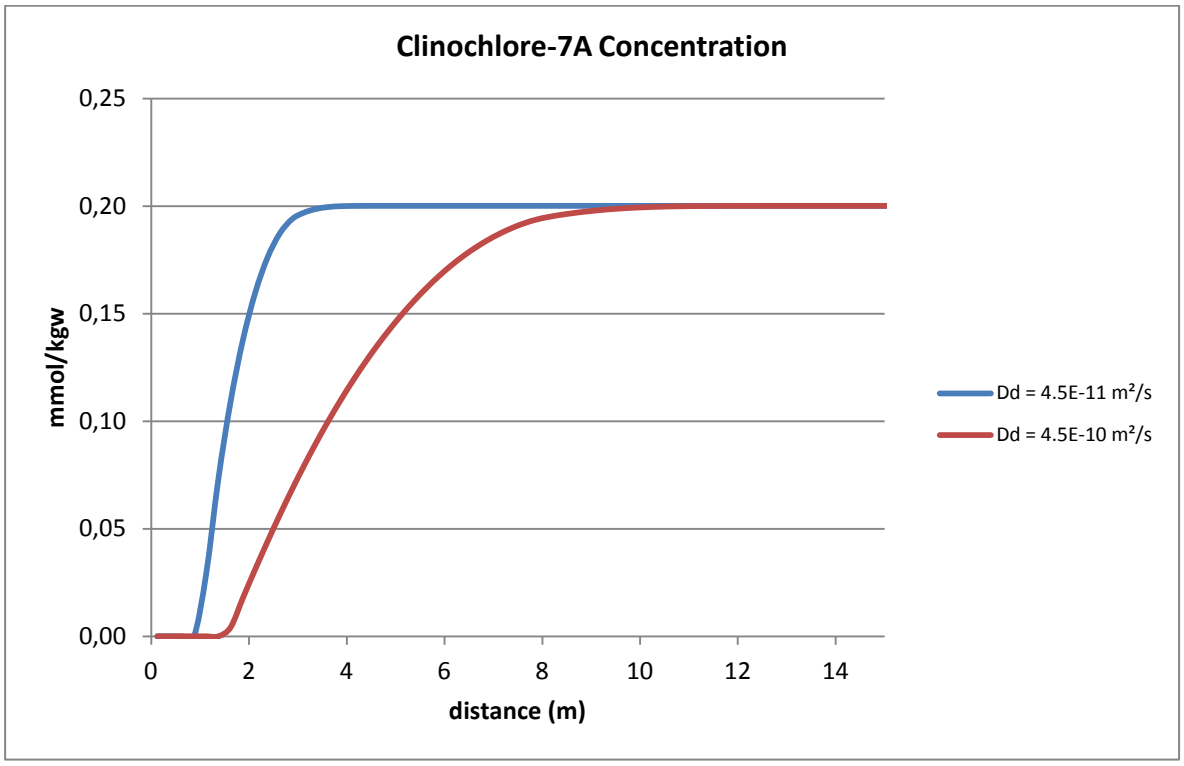

Figure 6.9: Clinochlore-7A concentration within the first 15 meters of the cap rock.

Figure 6.9 shows that clinochlore-7A is not present in the first meter, but concentration is steadily increasing until equilibrium is reached after four meters. Precipitation of clinochlore-7A is due to kaolinite and quartz dissolution, which provides it with Al^{3+} and $SiO_{2(aq)}$. Clinochlore-7A is first evident after 1.8 meters into the cap rock in the second run and increases steadily to equilibrium concentration of 0.2 mmol/kgw after approximately eleven meters.

6.3 Frio Shale Diffusive Transport

Diffusive transport is run for 200 years. Plagioclase is again represented as albite. Two different diffusion coefficients were used, with the slowest one taken from literature (Xu et al. 2005). Sensitivity was conducted on the grid cells, and the same number of cells and cell sizes are used for Frio Shale as for Nordland Shale with 200 cells à 0.25 meters.

The original diffusion coefficient at the Frio cap rock is $D_d = 1 \times 10^{-9}$ m^2/s (run 1). The second run has a diffusion coefficient of $D_d = 1 \times 10^{-8}$ m^2/s. Porosity of the cap rock at Frio is equal to 0.10. The moles allowed to react at Frio Shale is an order of magnitude higher than for Nordland, as there were little or no problems with convergence. Therefore, the number of moles for each mineral is not directly comparable to Nordland Shale. This will not change the length of the diffusive section of the cap rock.

6.3.1 Summary of Results

The first 15 meters of the cap rock are visibly affected by the diffusive transport at Frio Shale, however small changes can be seen within the first 25 meters by careful examination of the output file. With a faster diffusion coefficient the changes may be seen for the entire cap rock for some minerals. The changes in concentration are much smaller than for Nordland Shale, partly because diffusive transport takes place over a larger distance. Calcite has the largest molar concentration among the minerals and is evidently dominating the mineral trapping process. Quartz also dominates the cap rock composition by molar volume but concentration barely changes. The same is true for dawsonite, but dawsonite shows a fluctuating concentration over the diffusive section. Some alteration is also seen for K-feldspar and Na-montmorillonite. Siderite also precipitates to contribute to the mineral trapping of CO_2. Clinochlore-7A and kaolinite concentrations are very small and are excluded from the following. Their plots are given in Appendix E.

Table 6.4: pH during diffusive transport for Frio Shale

Run 1			**Run 2**		
	Initial	Final	Initial	Final	Figure No.
pH	6.20	6.45	6.36	6.45	Figure 6.10

Table 6.5: Diffusive transport results for Frio Shale.

	Run 1		**Run 2**		
Mineral/ CO_2	Initial concentration (mmol/kgw)	Final concentration (mmol/kgw)	Initial concentration (mmol/kgw)	Final concentration (mmol/kgw)	Figure no.
$CO_{2(g)}$	344.4	193.3	142.7	193.3	Figure 6.11
Calcite	93.9	98.0	93.9	98.0	Figure 6.12
Quartz	90.3	90.2	90.2	90.2	Figure 6.13
Dawsonite	51.0	50.5	50.9	50.5	Figure 6.14
K-feldspar	23.8	25.3	24.6	25.3	Figure 6.15
Na-montmor	18.2	17.4	17.7	17.4	Figure 6.16
Siderite	0.00	0.5	0.00	0.5	Figure 6.17
Clinochlore-7A	0.80	0.9	0.89	0.9	Figure E.1
Kaolinite	0.00	0.00	0.00	0.00	Figure E.2

Other minerals were not present after 200 years of diffusive transport.

6.3.2 Diffusive Transport Results with Albite Representing Plagioclase

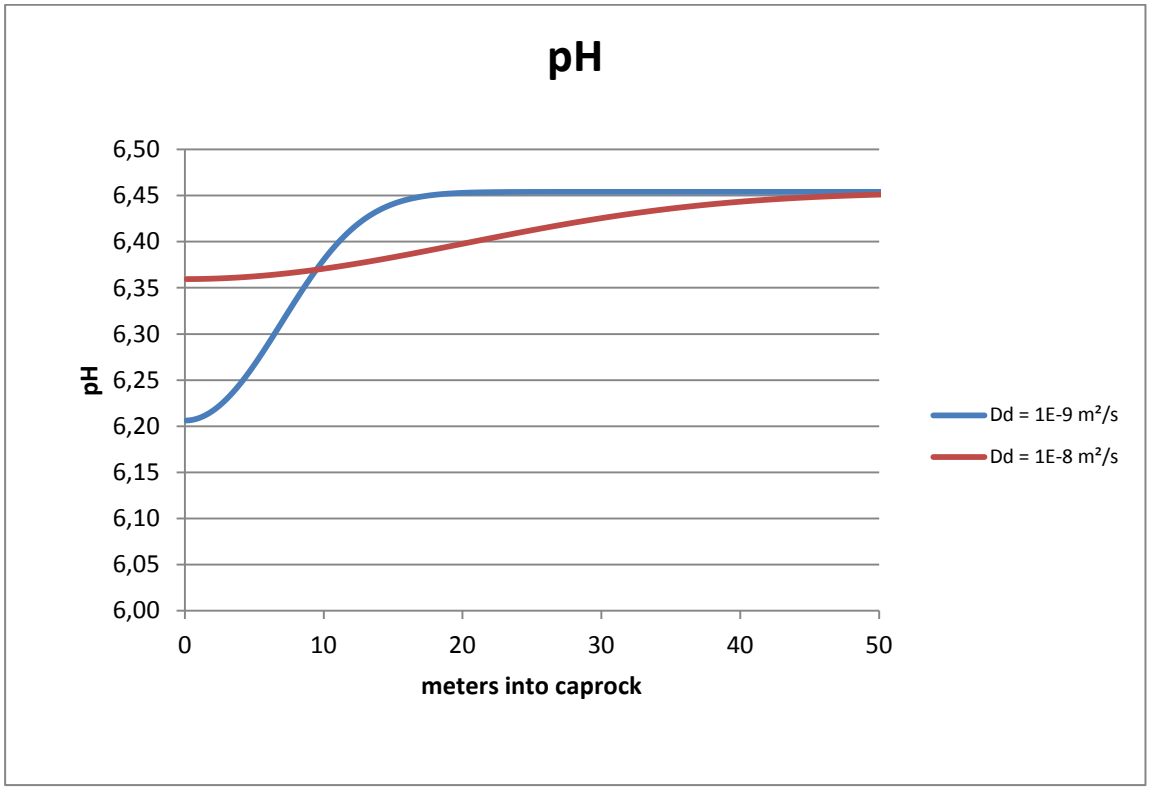

Figure 6.10: pH variations.

Figure 6.10 indicates that pH variations are much less for Frio Shale than for Nordland Shale, because the pH at Frio Shale is more stable. pH rises from 6.20 in the first cell to the original pH of 6.45 after 27 meters, which of course is the pH of the system after 200 years given no presence of injected CO_2. In run 2 the pH almost reaches original level after 50 meters.

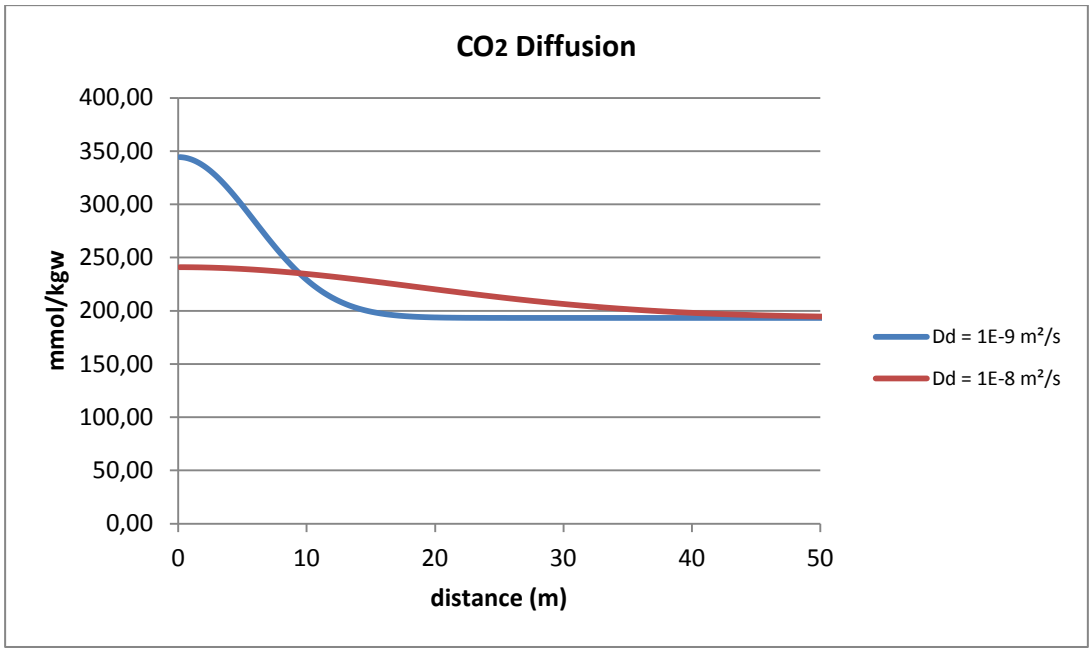

Figure 6.11: CO_2 concentration.

Figure 6.11 shows that for the original diffusion coefficient the concentration of CO_2 decreases from 344.4 mmol/kgw to the equilibrium concentration of 193.3 mmol/kgw after 27 meters into the shale. The level of CO_2 is much higher than for Nordland Shale, but the original level of natural occurring CO_2 is evidently much higher for Frio Shale than for Nordland Shale. Run 2 shows that with a diffusion coefficient that is ten times higher than the original the elevated CO_2 concentration is visible for the entire cap rock.

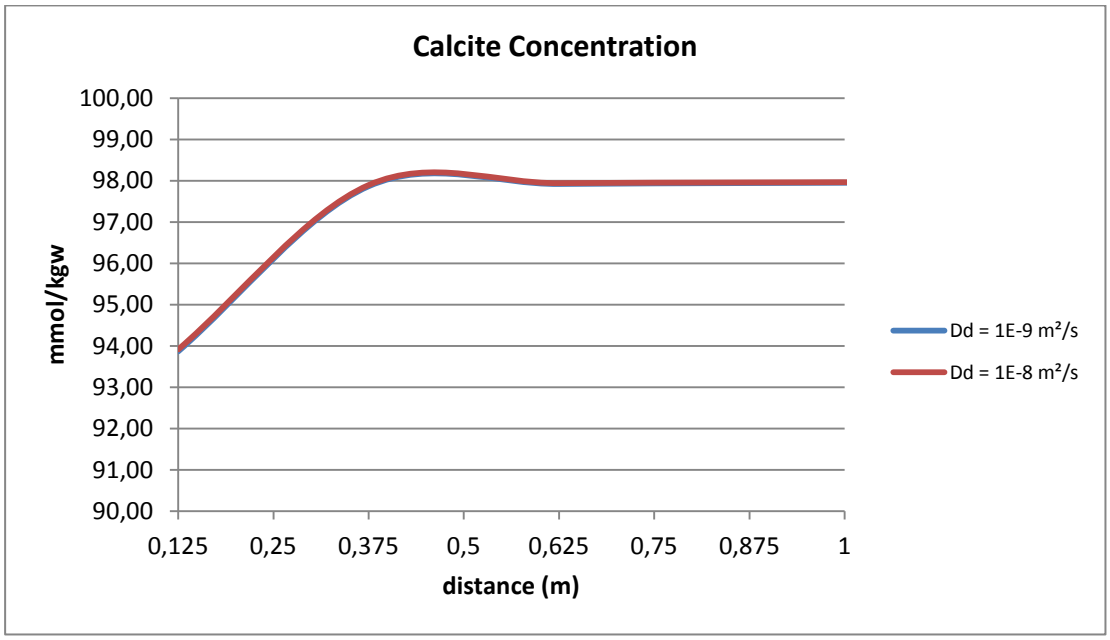

Figure 6.12: Concentration of calcite in the first meter of the cap rock.

Calcite precipitation happens very fast and is equal for both diffusion coefficients. Figure 6.12 shows that calcite concentration increases rapidly from 93.9 mmol/kgw to 98.0 mmol/kgw within the first 0.4 meters. This is partly because dawsonite dissolves in this section (Figure 6.14) and supplies calcite with carbonate ions, and partly due to the CO_2 dissolution. Note that the plot starts at 0.125 meters. This is because the concentration is measured in the middle of the first cell (0.125 meters).

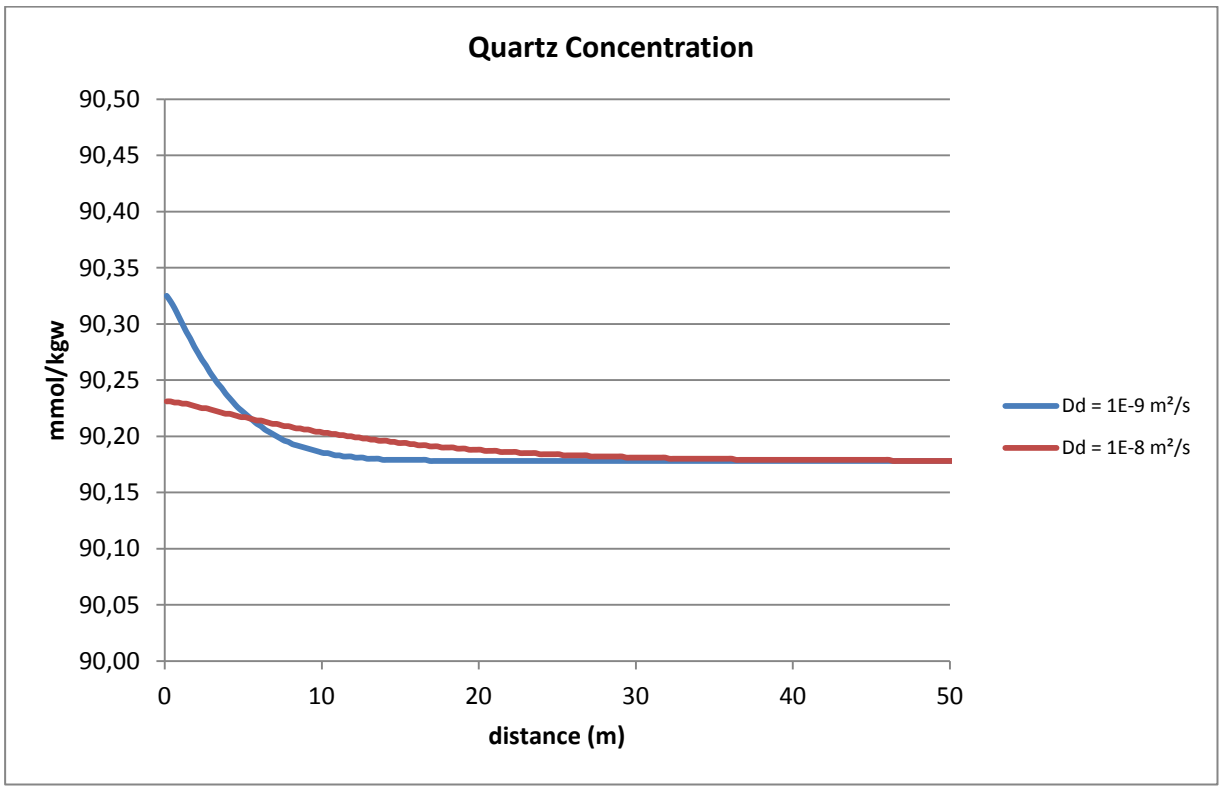

Figure 6.13: Concentration of quartz.

Quartz concentration decreases from 90.3 mmol/kgw to 90.2 mmol/kgw in run 1, as shown in Figure 6.13. Concentration of quartz is decreasing with decreasing CO_2 concentration, which is expected due to the relative increase of otherwise dissolving silicates. The slope of quartz in the second run has a similar slope as run 1 and affects the initial 40 meters of the cap rock compared to the first 20-25 meters for run 1.

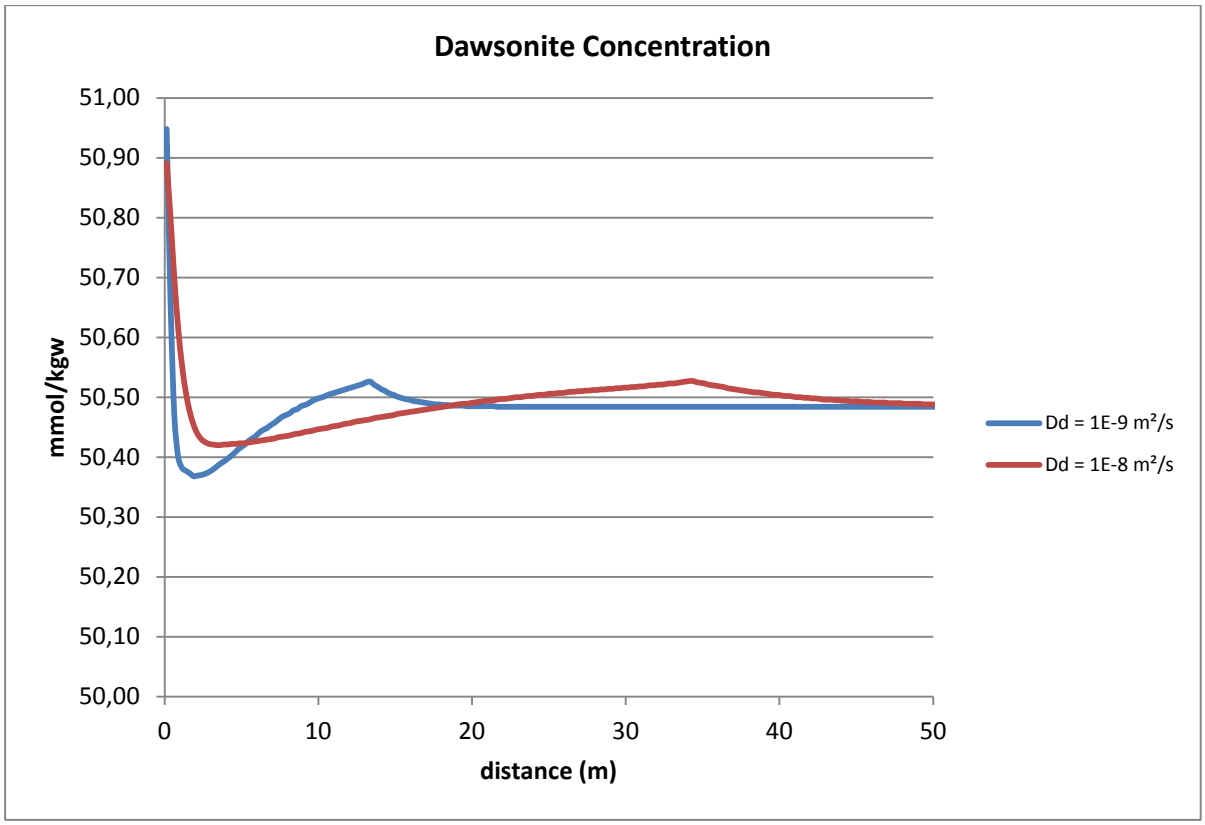

Figure 6.14: Concentration of dawsonite (secondary mineral).

Figure 6.14 indicates that dawsonite concentration is fluctuating. First, dawsonite decreases relatively sharply from a concentration of ca 51 mol/kgw to 50.4 mol/kgw within the first meter. In this period Na-montmorillonite (Figure 6.16) precipitates, so it is reasonable to believe that dawsonite dissolution which deliberates Na^+ ions fuels the initial precipitation phase of Na-montmorillonite. For the next 10 meters dawsonite precipitates to a concentration of 50.53 mmol/kgw, before a short dissolution phase is evident until the concentration reaches equilibrium.

The same trend is evident for run 2, where the initial dissolution phase occurs in the first two meters of the cap rock, and the subsequent precipitation seizes after approximately 35 meters. Subsequent dissolution acts for the remainder of the cap rock.

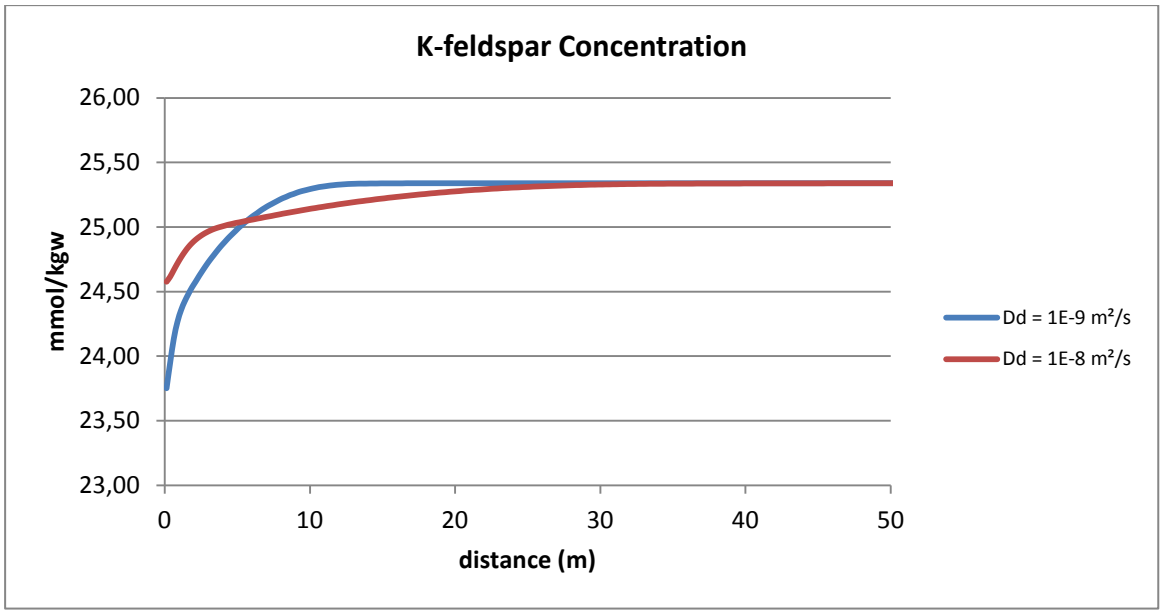

Figure 6.15: K-feldspar concentration.

Figure 6.15 shows that the concentration of potassium feldspar increases from 23.75 mmol/kgw to 25.3 kg mmol/kgw within the first 15 meters. K-feldspar precipitation is supplied with K^+ from diffusing element K, and $SiO_{2(aq)}$ and Al^{3+} from dissolving minerals. The trend is similar for run 2, with an initial concentration of 24.6 mmol/kgw. Diffusive transport for run 2 affects the first 30-35 meters of the cap rock.

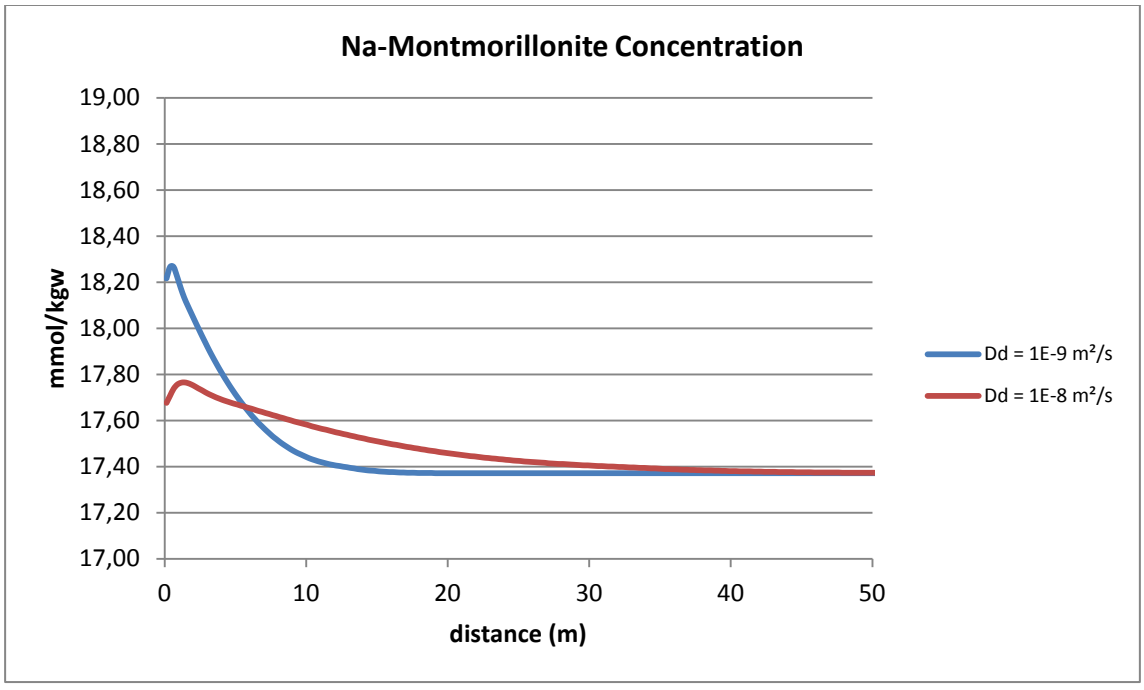

Figure 6.16: Concentration of Na-montmorillonite clay.

Figure 6.16 indicates that the concentration of Na-montmorillonite clay increases within the first 50 centimetres of the cap rock for run 1, before it dissolves for the next 17 meters. The initial feature is due to the dissolution of dawsonite, which contributes with Na^+ to the precipitating Na-montmorillonite (Figure 6.14). Equilibrium concentration is 17.4 mmol/kgw, and initial concentration is 18.2 mmol/kgw.

The initial precipitation is more evident for the second run, where precipitation can be seen within the first 1.5 meters. Initial concentration is 17.7 mmol/kgw and equilibrium concentration of 17.4 mmol/kgw is seen after 40 meters.

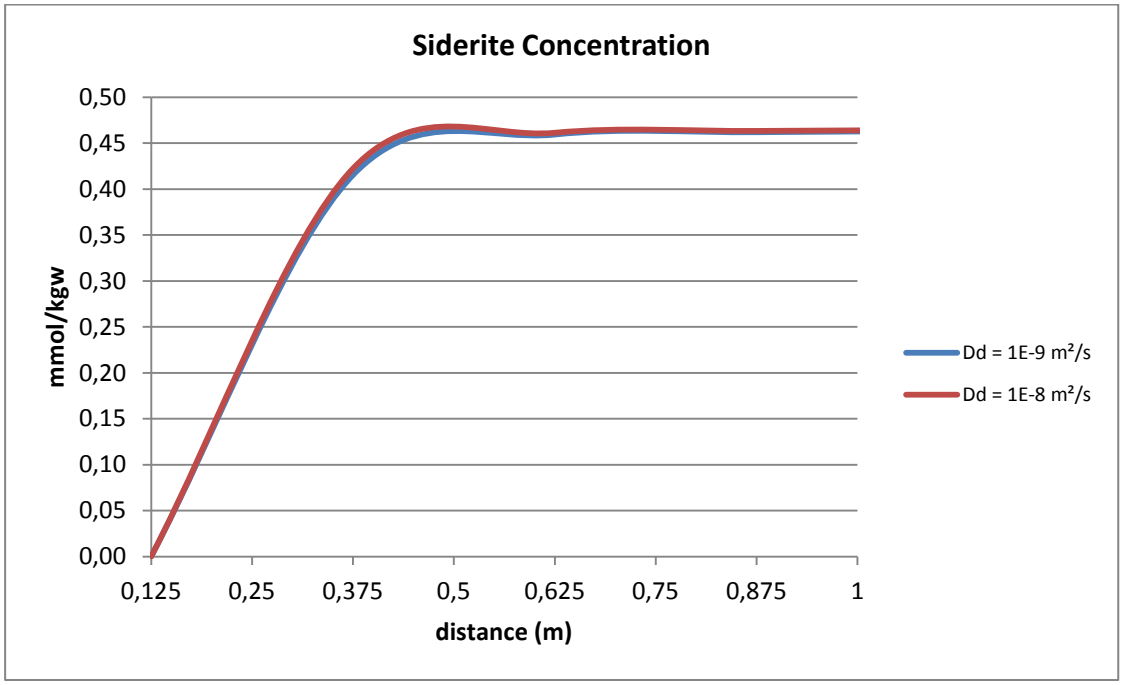

Figure 6.17: Siderite concentration.

Siderite concentration is practically identical for the two runs, as seen in Figure 6.17. Siderite concentration is very low compared to the minerals above, but it nevertheless works to trap a minor amount of CO_2. Equilibrium concentration of siderite is 0.46 mmol/kgw.

7. Discussion

Previous studies have been conducted on the sites investigated in this thesis (Gaus et al. 2005, Xu et al. 2005, Audigane et al. 2006). These studies showed that the diffusive transport after 1 000 to 10 000 years is likely to affect the lower 5-10 meters of the two investigated cap rocks, which is similar to this thesis for Nordland Shale in particular. These studies are not directly comparable with the thesis with respect to the mineralogical changes because of different time scales and setup. The trends can however be compared for kinetic batch simulation at the cap rock of Sleipner. Long-term kinetic reactions at Nordland Shale are similar to previous studies (Gaus et al. 2005). Albite dissolves and supplies ions to precipitating quartz, kaolinite, calcite and dawsonite. The rate of albite dissolution is much slower in their work compared to the thesis results, possibly due to the use of different reactive surface areas. This thesis used reactive surface areas from another study (Xu et al. 2005). The short-term reactions are very similar, with initial dissolution of calcite that stabilizes pH at 4.5. The initial calcite dissolution goes much slower in the thesis.

Geochemical simulations can play a major part in the screening process of potential storage sites. Input data must be collected from the storage formations to provide necessary input to the geochemical model. This data should include both the cap rock and the underlying storage reservoir if possible. The simulated results must then be compared to results gathered from laboratory studies. This may pose challenges, since laboratory studies can show conflicting results compared to actual reservoir situations. It is also impossible to test a core sample over a geological time scale. Such challenges may be dealt with by testing the core plugs at higher temperature and pressures than the actual reservoir conditions to accelerate the geochemical reactions induced by CO_2.

Computer models are never better than their capabilities and limitations. PHREEQC can perform a vast selection of geochemical reactions, but it also has several limitations. The limitations are however relatively easy to detect and can often be overcome by some adjustments to the code setup. A significant challenge experienced in the thesis study was that

illite could not be modelled longer than approximately 1 000 years and had to be changed to muscovite. Illite would also cause the transport simulations to stop completely. The two minerals are similar, but will most likely yield some measurable variations in the results. Another limitation is the time constraints on the diffusive transport, and in some cases on the kinetic simulation. In addition to the limitations above there are conflicting values for rate parameters presented in literature. Convergence problems may also affect the results for aluminium and iron in particular. Convergence may be dealt with by downscaling the number of moles for each mineral or by changing the original concentration of Al and Fe in solution. Finally, the description of the secondary mineral assembly along with the primary minerals introduced to PHREEQC is an uncertainty factor.

Future work could include:

- Advection transport of the Nordland Shale and Frio Shale.
- Coupled shale-sandstone modelling of the Nordland Shale and Frio Shale.
- Diffusive transport for at least 1 000 years of the Nordland Shale and Frio Shale.
- Sensitivity on rate parameters.
- Diffusive transport and advection transport on other potential storage formations.
- Coupled geochemical modelling and reservoir modelling by means of quantifying the exact changes in permeability and porosity during the storage process.
- Quantification of the mineralogical changes by mass percent or volume percent.
- Geochemical simulation studies with other simulation tools (e.g. TOUGHREACT or PHAST) for comparison with PHREEQC.

8. Conclusions

- Minerals reach equilibrium at very different periods over a geological time scale. It may take over 10 000 years for some minerals so reach true equilibrium at low temperatures and pressures for CO_2 storage projects. Reactions may therefore alter the cap rock properties for a significant time.
- Kinetic simulations for Nordland Shale and Frio Shale show similar concentration trends for carbonate minerals. They precipitate and permanently trap a fraction of the CO_2.
- The trend of the kinetic batch simulations indicate that silicate dissolution and precipitation are strongly linked to the behaviour of CO_2.
- The lower 5-10 meters of the Nordland cap rock is likely to be affected by diffusive transport during the next 200 years.
- The lower 15-25 meters are likely to be affected by diffusive transport during the next 200 years at the Frio Shale formation. With a ten times higher diffusion coefficient the section affected by diffusive transport may be higher.
- Mineralogical changes in the lower 5-10 meters of Nordland Shale are significant. The Sleipner West caprock is extremely thick and is very likely to prevent the CO_2 from migrating further given diffusion transport only. However, the permeability and porosity of the lower cap rock are probably altered to a certain degree given these large mineralogical changes.
- The mineralogical changes caused by CO_2 storage at Frio Shale are relatively small for all minerals that are initially present at the lower cap rock boundary. These changes occur over a larger distance than for Nordland Shale due to the higher diffusion coefficients.
- This thesis considers reaction kinetics and diffusive transport. A main assumption is that the lower cap rock boundary is uniform. However, future studies should model advection transport to check the effects that a flow rate would have on the cap rock mineralogy.

9. References

Appelo, C.A.J., Postma, D., 2005. Geochemistry, Groundwater and Pollution. 2nd edn. Balkema, Leiden. 649 pp. *ISBN 978-0415364287*.

Audigane, P., Gaus, I., Pruess, K., Xu, T., 2006. A Long Term 2D Modelling Study of CO_2 Storage at Sleipner (North Sea) Using Toughreact. Proceedings in TOUGH Symposium, San Francisco, USA, May 12-22.

Bachu, S. and Adams, J.J., 2003. Sequestration of CO_2 in geological media in response to climate change: Capacity of deep saline aquifers to sequester CO_2 in solution, *Energy Convers. Manage.*, 44(20), 3151 – 3175.

Bachu, S., Shaw, J.C. and Pearson, R.M., 2004. Estimation of Oil Recovery and CO_2 Storage Capacity in CO_2-EOR Incorporating the Effect of Underlying Aquifers. Paper SPE 89340 presented at the 2004 SPE/DOE 14th Symposium on Improved Oil Recovery, Tulsa, Oklahoma, USA, 17-21 Apr.

Berner, R.A., Lasaga, A.C., 1983. The carbonate-silicate geochemical cycle and its effect on atmospheric carbon dioxide over the past 100 million years. *American Journal of Science*., v. 283, p. 641-683.

Cantucci, B., Montegrossi, G., Vaselli, O., Tassi, F., Quattrocchi, F., Perkins, E.H., 2009. Geochemical modeling of CO_2 storage in deep reservoirs: The Weyburn Project (Canada). *Chemical Geology*, 265, 181-197.

Celia, M.A., Bachu, S., Nordbotten, S.E., Gasda, S.E., and Dahle, H.K., 2004. Quantitative Estimation of CO_2 Leakage from Geological Storage: Analytical Models, Numerical Models, and Data Needs. Paper 18-01, Proceedings, 9th International Conference on Greenhouse Gas Control Technologies, Vancouver, Canada, September 5-9.

Chadwick, R.A., Zweigel, P., Gregersen, U., Kirby, G.A., Johannessen, P.N. and Holloway, S., 2004a. Geological Reservoir Characterisation of a CO_2 storage site: The Utsira Sand, Sleipner, northern North Sea. *Energy*, 29, 1371-1381.

Domenico, P.A., Schwartz, F.W., 1990. Physical and Chemical Hydrogeology. Wiley, New York. 824 pages. *ISBN 978-0471507444*.

Gaus, 1., Azaroual, M., Czernichowski-Lauriol, I., 2005. Reactive transport modelling of the impact of CO_2 injection on the clayey cap rock at Sleipner (North Sea). *Chemical Geology* 217, 319-337.

Gorecki, C. D., Sorenson, J. A., and Bremer, J. M., 2009. Development of Storage Coefficients for Determining the Effective CO_2 Storage Resource in Deep Saline Formations. Paper 126444 presented at the SPE International Conference on CO_2 Capture, Storage, and Utilization, San Diego, California, 2-4 November.

Helgeson, H.C., Garrels, R.M. and Mackenzie, F.T., 1969. Evaluation of irreversible reactions in geochemical processes involving minerals and aqueous solutions - II. Applications: *Geochimica et Cosmochimica Acta*, v. 33, p. 455-481.

Intergovernmental Panel on Climate Change (IPCC)., 2005. Special report on carbon dioxide capture and storage. Prepared by Working Group III of the IPCC, Cambridge University Press, Cambridge, U.K.

Jasinge, D., Ranjith, P. G., 2011. Carbon dioxide sequestration in geologic formations with special reference to sequestration in deep coal seams. Paper ARMA 11-595 presented at the 45th US Rock Mechanics/Geomechanics Symposium, San Francisco, CA, USA, 26-29 June.

Johnson, J. W., Nitao, J.J., Morris J.P., 2004. Modelling the Long-Term Isolation Performance of Natural and Engineered Geologic CO_2 Storage Sites. Paper 405 presented at 7th International Conference on Greenhouse Gas Control Technologies, Vancouver, Canada, 5-9 September.

Kaszuba, J. P., Janecky, D. R., Snow, M. G., 2003. Carbon dioxide reaction processes in a model brine aquifer at 200 ºC and 200 bars: implications for geologic sequestration of carbon. *Appl. Geochem*. 18, 1065-1080.

Lasaga, A.C., 1984. Chemical kinetics of water–rock interaction. *J. Geophys*. *Res*. 89, 4009–4025.

Li, Z., Dong, M., Li, S. and Huang, S., 2006. CO_2 sequestration in depleted oil and gas reservoirs - caprock characterization and storage capacity. *Energy Conversion and Management*, 47, 1372-1382.

Marini, L. 2006. Geological Sequestration of Carbon Dioxide, Volume 11: Thermodynamics, Kinetics, and Reaction Path Modelling. 11 edn. Elsevier Science. 470 pages. *ISBN 978-044529503.*

Nguyen, D. N., 2003. Carbon Dioxide Geological Sequestration: Technical and Economic Reviews. Paper SPE 81199 presented at the SPE/EPA/DOE Exploration and

Production Environmental Conference, San Antonio, Texas, 10-12 March.

Parkhurst, D. L., Appelo, C. A. J., 1999. User's Guide to PHREEQC, version 2; *U.S. Geological Survey Water Resource Inv*. 99-4259.

Pauwels, H., Gaus, I., le Nindre, Y. M., Pearce, J., Czernichowski-Lauriol, I., 2007. Chemistry of fluids from a natural analogue for a geological CO_2 storage site (Montmiral, France): Lessons for CO_2-water-rock interaction assessment and monitoring, *Appl. Geochem*., 22, 2817.

Rickard, D. and Sjöberg, E. I., 1983. Mixed kinetic control of calcite dissolution rates. *American Journal of Science*., 283, p. 815-830.

Sahin, S., Kalfa, U., and Celebioglu, D., 2012. Unique CO_2-Injection Experience in the Bati Raman Field May Lead to a Proposal of EOR/Sequestration CO_2 Network in the Middle East. Paper SPE 139616 presented at the SPE International Conference on CO_2 Capture, Storage and Utilization, New Orleans, Louisiana, 10-12 November.

Shukla, P., Ranjith., P., ,Haque. and Choi, X., 2010. A Review of studies on CO_2 sequestration and caprock integrity. *Fuel*, 89, 2651-2664.

Soong, Y., Goodman, A. L., McCarthy-Jones, J.P., and Baltrus, J.P. 2004. Experimental and simulation studies on mineral trapping of CO_2 with brine. *Energy Conversion and Management 4*5, 1845-1859.

Statoil., 2012. Sleipner Vest factfile. http://www.statoil.com

Sweatman, R., Crookshank, S., Edman, S., 2011. Outlook and Technologies for Offshore CO_2 EOR/CCS Projects. Paper OTC 21984 presented at the Offshore Technology Conference, Houston, Texas, USA 2-5 May.

Wright, I., 2007. The In Salah Gas CO_2 Storage Project. Paper 11326 presented at International Petroleum Technology Conference, Dubai, U.A.E, 4-6 December.

Xie, X. and Economides, M .J., 2009. The Impact of Carbon Geological Sequestration. Paper SPE 120333 presented at SPE Americas E&P Environmental & Safety Conference, San Antonio, Texas, 23-25 March.

Xu, T., Apps, J. A. and K. Pruess., 2005. Mineral sequestration of a sandstone-shale system. *Chemical geology*, v. 217, (3-4), p. 295-318.

APPENDIX A - Dissociation Reactions

Table A.1: Relevant dissociation reactions for Nordland Shale and Frio Shale (Parkhurst and Appelo 1999).

Mineral introduced in PHREEQC	Dissociation reaction listed in llnl.dat
Muscovite	$KAl_3Si_3O_{10}(OH)_2 + 10\ H^+ = K^+ + 3\ Al^{3+} + 3\ SiO_2 + 6\ H_2O$
Quartz	$SiO_2 = SiO_2$
Kaolinite	$Al_2Si_2O_5(OH)_4 + 6\ H^+ = +2\ Al^{3+} + 2\ SiO_2 + 5\ H_2O$
Albite	$NaAlSi_3O_8 + 4\ H^+ = Al^{3+} + Na^+ + 2\ H_2O + 3\ SiO_2$
Anorthite	$CaAl_2(SiO_4)_2 + 8\ H_+ = Ca^{2+} + 2\ Al^{3+} + 2\ SiO_2 + 4\ H_2O$
Smectite-high-Fe-Mg	$Ca_{0.025}\ Na_{0.1}\ K_{0.2}\ Fe^{2+}{}_{0.5}Fe^{3+}{}_{0.2}\ Mg_{1.15}Al_{1.25}Si_{3.5}H_2O_{12} + 8\ H+ = 0.025\ Ca^{2+} + 0.1\ Na^+ + 0.2\ K^+ + 0.5\ Fe^{2+} + 0.2\ Fe^{3+} + 1.15\ Mg^{2+} + 1.25\ Al^{3+} + 3.5\ SiO_2 + 5\ H_2O$
Clinochlore-7A	$Mg_5Al_2Si_3O_{10}(OH)_8 + 16\ H+ = +2\ Al^{3+} + 3\ SiO_3 + 5\ Mg^{2+} + 12\ H_2O$
Pyrite	$FeS_2 + H_2O = 0.25\ H^+ + 0.25\ SO_4^{2-} + Fe^{2+} + 1.75\ HS^-$
K-feldspar	$KAlSi_3O_8 + 4\ H^+ = Al^{3+} + K^+ + 2\ H_2O + 3\ SiO_2$
Siderite	$FeCO_3 + H^+ = Fe^{2+} + HCO_3^-$
Na-Montmorillonite	$Na_{0.33}Mg_{0.33}Al_{1.67}Si_4O_{10}(OH)_2 + 6\ H^+ = 0.33\ Mg^+ + 0.33\ Na^+ + 1.67\ Al^{3+} + 4\ SiO_2 + 4\ H_2O$
Calcite	$CaCO_3 + H^+ = Ca^{2+} + HCO_3^-$
Dolomite	$CaMg(CO_3)_2 + 2\ H^+ = Ca^{2+} + Mg^{2+} + 2HCO_3^-$
Dawsonite	$NaAlCO_3(OH)_2 + 3\ H^+ = Al^{3+} + Na^+ + HCO_3^- + 2\ H_2O$
Magnesite	$MgCO_3 + H^+ = HCO_3^- + Mg^+$

APPENDIX B - Input to Rate Formulas

Table B.1 Input to the rate equations for Nordland Shale.

Mineral	**Reactive surface area (m^2/kgw) (calculated)**	**n (assumed)**	**log k at 37°C (Gaus et al 2005)**
Muscovite	199.9	0.5	-13.08
Quartz	10.4	0.5	-6.35
Kaolinite	135.8	0.5	-12.54
Albite/Anorthite	6.0	0.5	-8.44
Smectite-high-Mg-Fe	59.6	0.5	-13.25
Clinochlore-7A	2.0	0.5	-11.63
Pyrite	2.5	0.5	-3.72
K-feldspar	1.0	0.5	-8.79
Siderite	1.1	0.5	-7.38
Calcite	0.5	0.5	-6.35

Table B.2 Input to the rate equations for Frio Shale.

Mineral	**Reactive surface area (m^2/kgw) (calculated)**	**n (assumed)**	**log k at 75°C (Xu et al. 2005)**
Muscovite	106.4	0.5	-9.78
Na-montmorillonite	73.8	0.5	-9.78
Quartz	4.5	0.5	-11.70
Calcite	N/A	N/A	N/A
Albite/Anorthite	1.3	0.5	-8.15
K-feldspar	1.1	0.5	-8.15
Kaolinite	15.7	0.5	-10.06
Clinochlore-7A	0.56	0.5	-10.02

APPENDIX C - Additional Figures for Nordland Shale Kinetic Batch Modelling Results

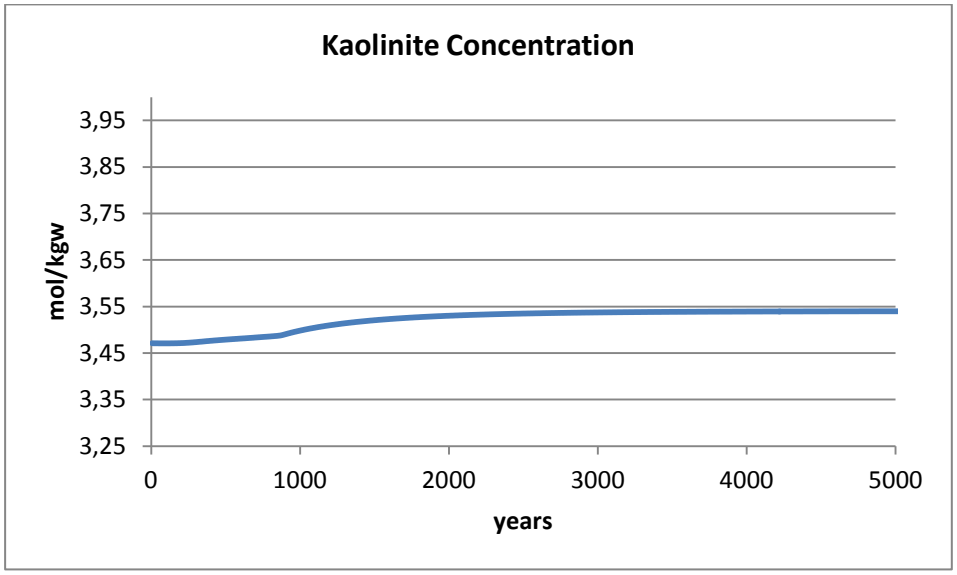

Figure C.1: Kaolinite concentration for the initial 5 000 years

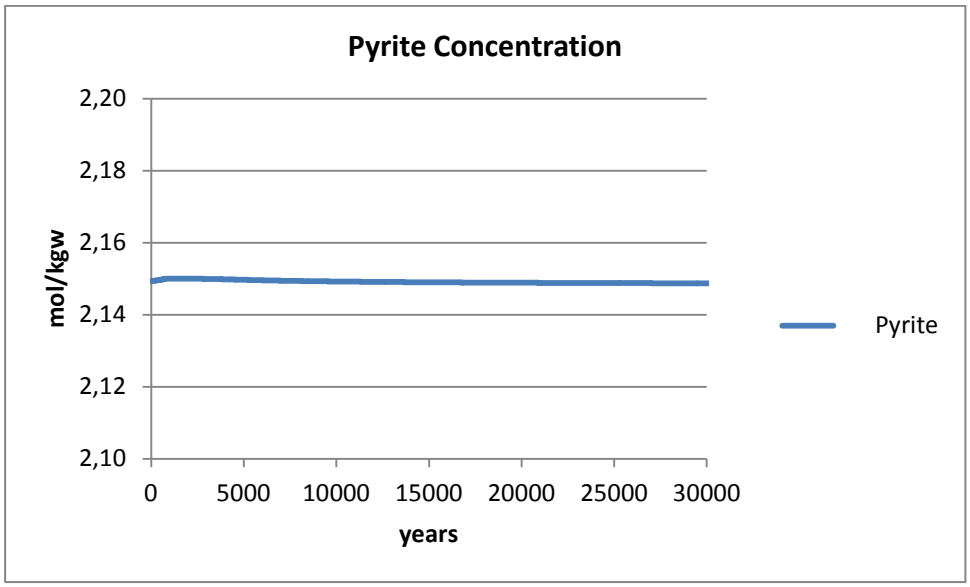

Figure C.2: Pyrite Concentratio

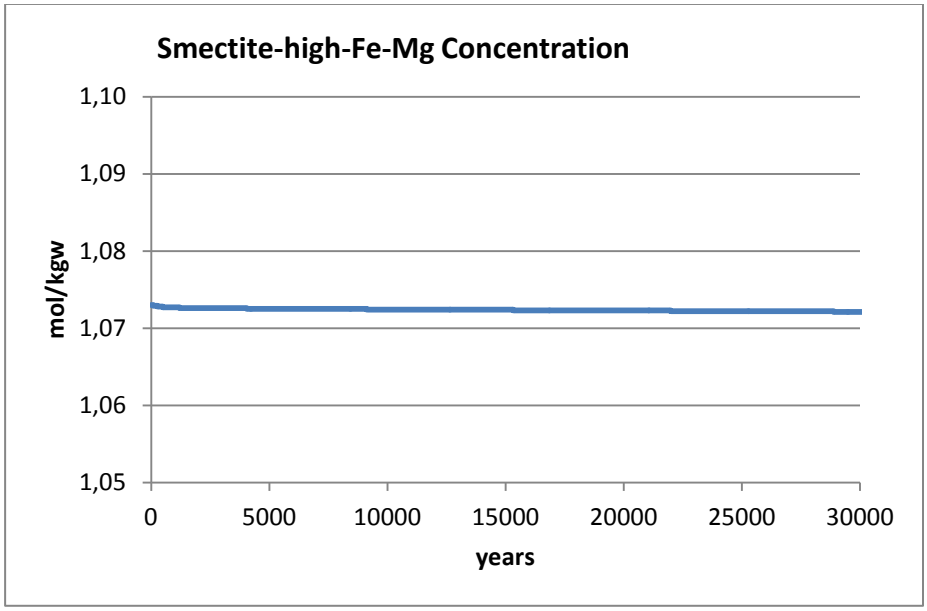

Figure C.3: Smectite-high-Fe-Mg concentration.

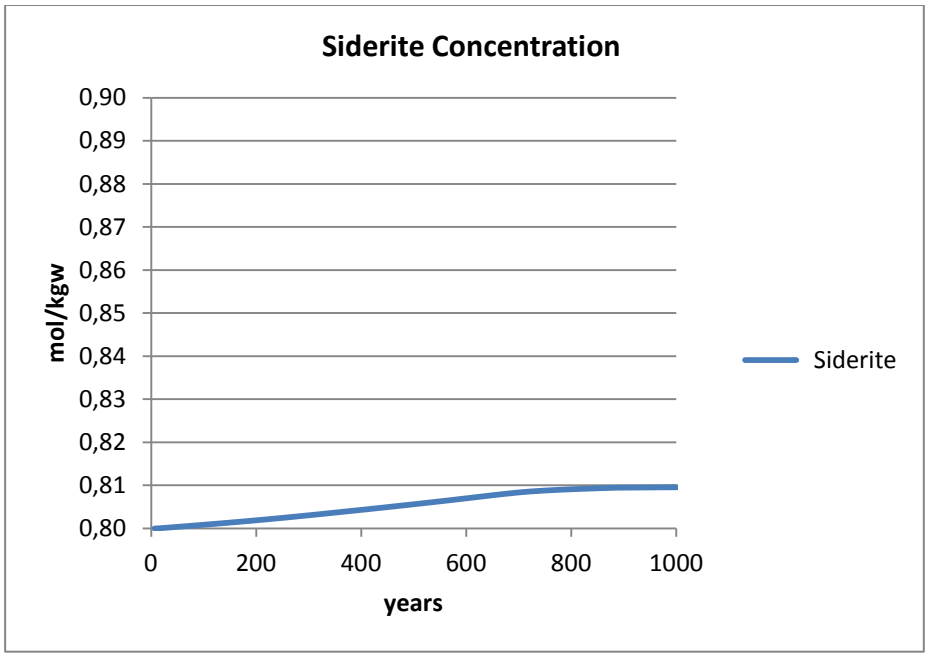

Figure C.4: Siderite concentration.

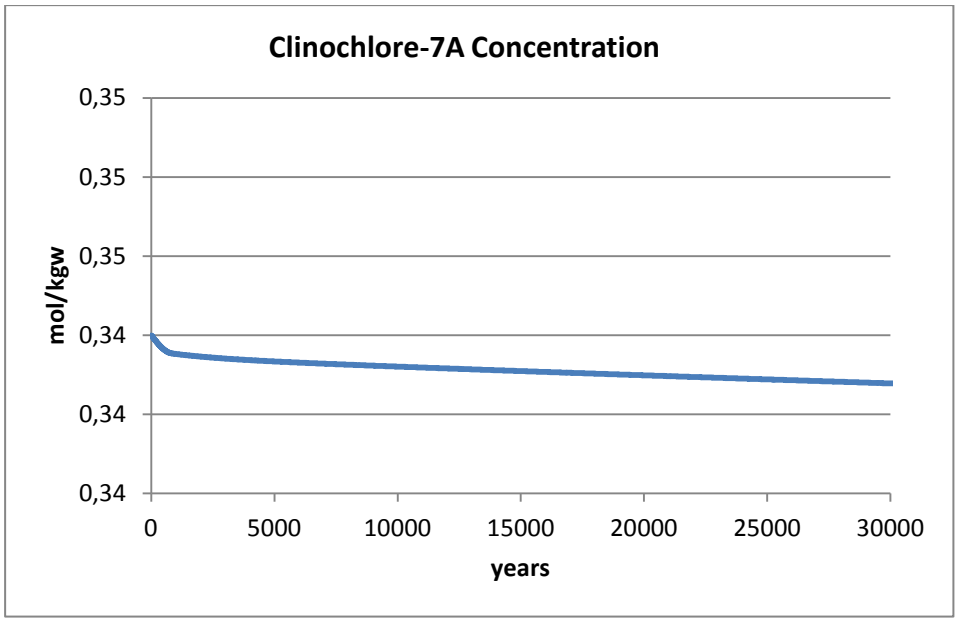

Figure C.5: Clinochlore-7A concentration.

APPENDIX D - Additional Figures for Frio Shale Kinetic Batch Modelling Results

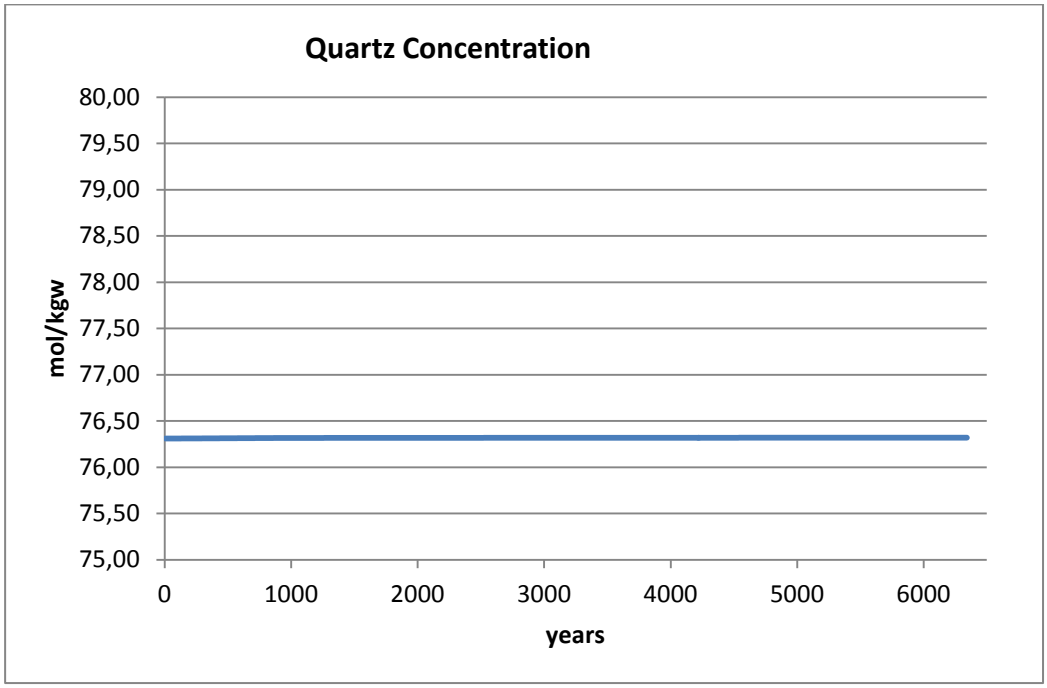

Figure D.1: Quartz concentration.

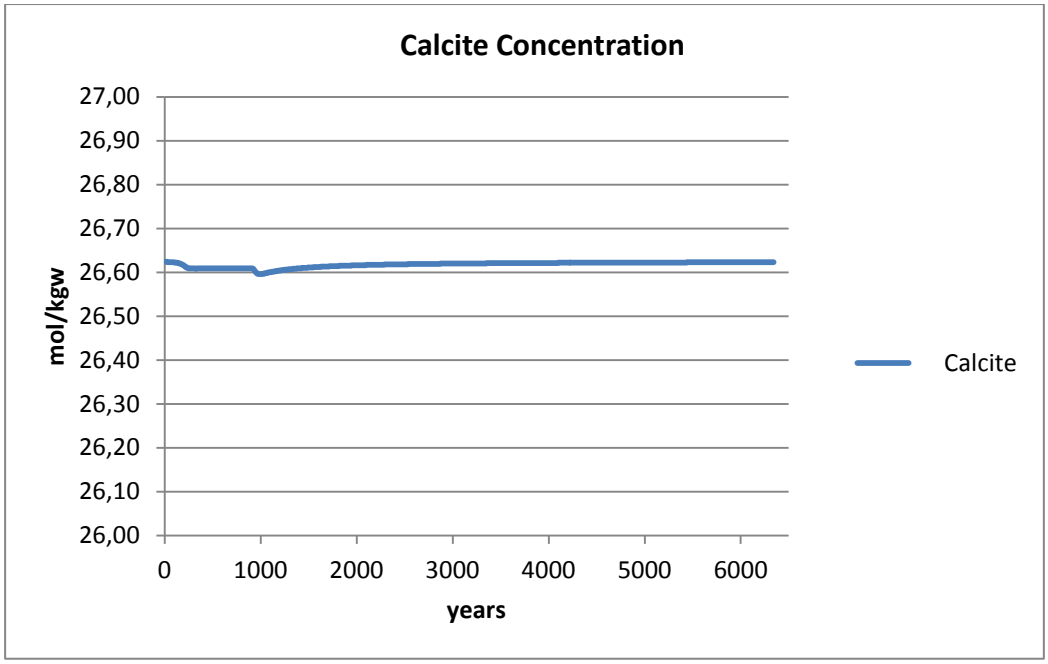

Figure D.2: Calcite concentration

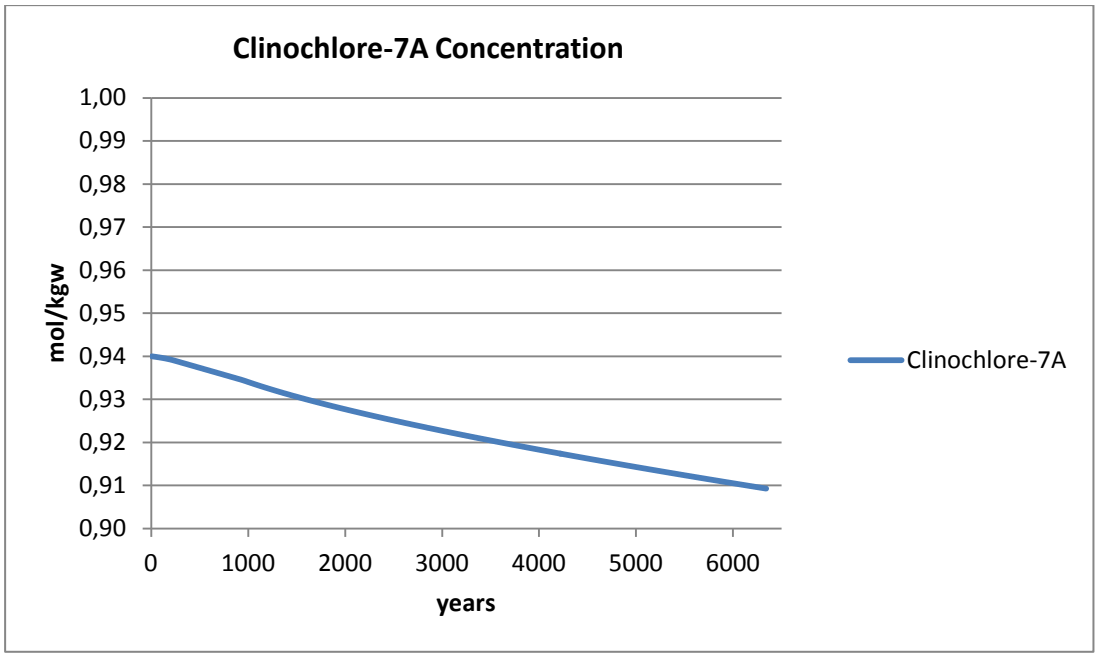

Figure D.3: Clinochlore concentration

APPENDIX E - Additional Figures for Frio Shale Diffusive Transport Results

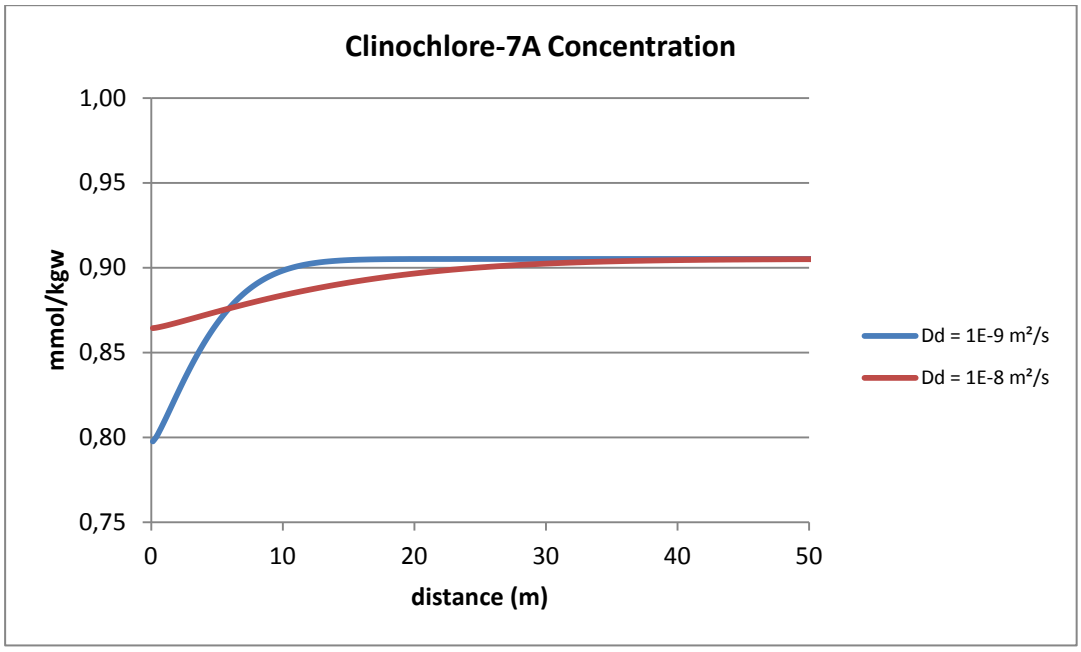

Figure E.1: Concentration of clinochlore-7A.

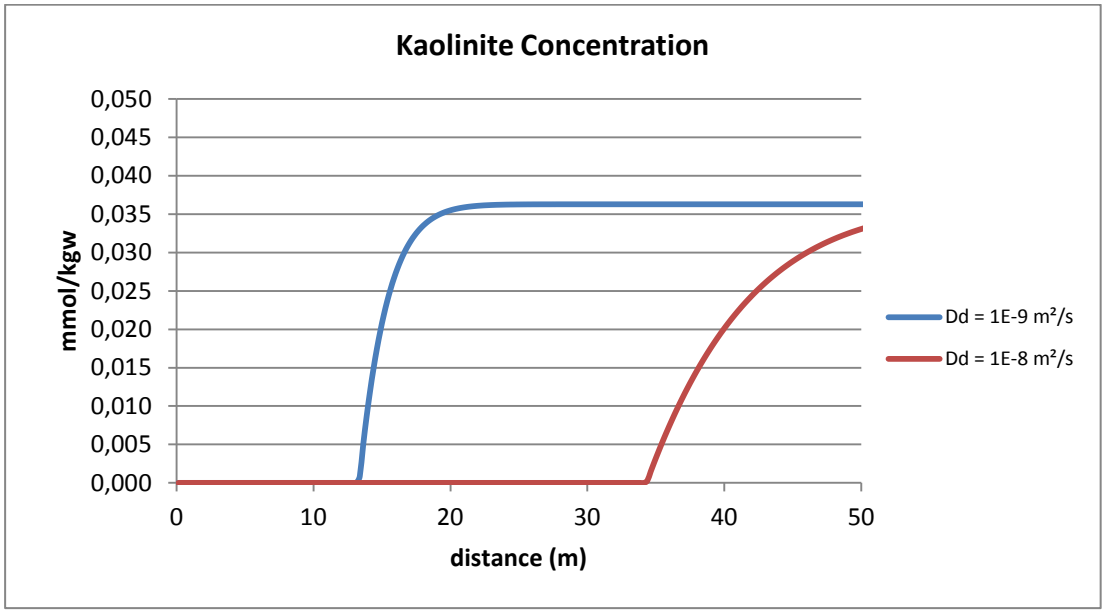

Figure E.2: Concentration of kaolinite.